Sediments in Angostura Hydropower Reservoir

Halvor Kjærås

Sediments in Angostura Hydropower Reservoir

Halvor Kjærås

June 8, 2012

Preface

This report is a master's thesis at the Department of Hydraulic and Environmental Engineering at the Norwegian University of Science and Technology. The main supervisor for the project is Nils Reidar Bøe Olsen, and assistant supervisor is Stefan Haun. The project is part of a research project on numerical modeling of sediment transport at the department, financed by the Norwegian Research Council. As part of the research project, the department is cooperating with ICE, the Costa Rican Institute of Electricity, using SSIIM to model sediment transport in the reservoirs for ICE's power plants. The main objective of the master's project was to use the SSIIM model to do three-dimensional numerical simulations of water and sediment flow in the Angostura reservoir in Costa Rica. The work consists of three parts: a testing of a simpler engineer tool named the RESCON model, a sediment concentration distribution simulation using SSIIM, and a sediment flushing using SSIIM. Some of the results from the work are used in an article written by Stefan Haun, Nils Reidar Bøe Olsen and me, and quite some time was spent revising the figures for the article. The work on the three parts has been done in series, effectually reducing the time available for the flushing part. The main focus has been on the concentration distribution simulation, so this is considered the most imporant part of the thesis.

The work on the thesis stared on January 12 2012 and was to be concluded on June 12. As this is the author's first time using the numerical model apart from the basics, some time was spent learning the program and understanding its workings. During the project work in the previous semester, an excursion to the reservoir in question was arranged in order to collect input data for the simulations.

I would like to thank my supervisors for help with my project, as well as operators and management at ICE for assistance during the measurements, and Sigurd Løvfall for assistance in the first part of the thesis.

<div align="center">

2012-06-08

Halvor Kjærås

</div>

Abstract

Reservoirs in areas with a high sediment yield will without mitigation sooner or later be filled up with sediments, reducing the volume available for regulation for electric generation. Flushing of sediments is a management strategy used in many reservoirs in the world, with varying degree of success. The Angostura reservoir is a shallow reservoir located on an inundated river, making it extra vulnerable to sedimentation. It is estimated a yearly inflow of 1.5 million tons of sediment. Other reservoirs are located upstream, and the flushing of these leads to large quantities of sediment inflow in a short period of time. In September every year, the water level in Angostura is partially drawn down to route this sediment through the reservoir. In November, the water level is drawn down completely, and a full sediment flushing is performed.

The RESCON model is a spreadsheet program designed to find a technically feasible sediment management strategy that maximizes the economical benefits of the project. Flushing is modeled with a simple algebraic model.

SSIIM is a three-dimensional computational fluid dynamics program designed for hydraulic engineering. Sediment erosion, transport and sedimentation can be modeled in a complex reservoir geometry using an adaptive grid with a moveable bed.

The main objective of this thesis is to test the performance of the RESCON and SSIIM models. The RESCON model was tested on the November flushing to see if it can reproduce the measured volume of flushed sediments. SSIIM was used for simulation of sediment concentration distribution in the reservoir, and to model the September flushing. The results are compared to measured values.

The reservoir geometry is based on bathymetry data from September 2011. Inflow series are from logged values at the hydropower plant.

Depth-averaged concentration values are used to present the longitudinal concentration distribution, and Hunter Rouse profiles to present the vertical distribution.

Using known reservoir values and the recommended coefficients, the RESCON model was not able to get close to the actual volume of flushed sediments. Although the model has given promising results in other cases, the complex reservoir geometry in Angostura sets heavy restrictions on the flushing processes in the reservoir, which an algebraic model of this type cannot reproduce.

The steady state simulation was successful in explaining previously unexplained variations in the concentration in the lateral and longitudinal direction of the reservoir. The simulation reproduces the longitudinal and vertical concentration distribution well.

A bug in the implementation of the second-order scheme in SSIIM was discovered, which has later been fixed, giving more similar results for the first-order and second-order schemes.

The time allocated for the flushing simulation was not enough to get satisfactory results. The erosion in the upstream end is modelled well, but the measured sedimentation in the downstream area is much larger than in the simulations. With more time for this simulation, it would have been possible to increase the quality of the results.

iii

Sammendrag

Reservoarer i områder med høy sedimentføring vil uten tiltak før eller siden fylles med sedimenter, noe som reduserer det tilgjengelige volumet til regulering for elektrisitetsproduksjon. Sedimentspyling er en strategi som er brukt i mange reservoarer i verden, med varierende grad av suksess. Angostura-reservoaret er et grunt reservoar, noe som gjør det ekstra sårbart for sedimentering. Det er estimert at årlig tilløp av sedimenter er 1,5 millioner tonn. Spyling av reservoarer oppstrøms fører til voldsom sedimentinnstrømning på kort tid. I september hvert år blir vannstanden i Angostura delvis senket for å route disse sedimentene gjennom reservoaret. I november senkes vannspeilet fullstendig, og det gjennomføres en fullverdig spyling.

RESCON-modellen er et regnearkprogram designet for å finne en teknisk gjennomførbar sedimentstrategi som samtidig maksimerer prosjektets økonomi. Spyling modelleres med en enkel algebraisk modell.

SSIIM er et tredimensjonalt CFD-program designet for hydraulikk. erosjon, sedimenttransport og sedimentering kan modelleres i en kompleks geometri ved bruk av et adaptivt grid med bevegelig bunn.

Hovedmålet med denne oppgaven er å teste prestasjonene til de to modellene. RESCON-modellen ble testet på november-spylingen for å se om den kan reprodusere de målte verdiene av spylte sedimenter. SSIIM ble brukt for å simulere fordelingen av sedimentkonsentrasjoner i reservoaret, og for å modellere september-spylingen. Resultatene ble sammenlignet med målte verdier.

Reservoargeometrien er basert på batymetridata fra september 2011. Tidsserier med vannstand og vannføringer kommer fra loggede verdier fra kraftverket.

Dybdegjennomsnittsverdier benyttes for å presentere konsentrasjonsvariasjoner i lengderetningen, og Hunter Rouse-profiler til den vertikale variasjonen.

Ved å bruke kjente reservoarverdier og anbefalte koeffisienter, var RESCON-modellen ikke i stand til å komme nær den målte verdien av spylte sedimenter. Selv om modellen har gitt lovende resultater i andre tilfeller, setter den kompliserte reservoargeometrien store begrensninger på spyleprosessene i Angostura, som en slik algebraisk modell ikke kan gjenskape.

Steady-state-simuleringen gjord det mulig å forklare tidligere uforklarte sedimentkonsentrasjonsvariasjoner i lengde- og bredderetningen i reservoaret. Simuleringen reproduserer konsentrasjonsfordelingen vertikalt og i lengderetningen godt.

En bug i implementeringen av andreordensskjemaet i SSIIM ble oppdaget, som senere ble fikset, slik at resultatene fra første- og andre-ordensskjemaene ble likere.

Den tildelte tiden til spylesimuleringen var ikke tilstrekkelig til å gi tilfredsstillende resultater. Eroderingen i oppstrøms ende er godt modellert, men den målte sedimenteringen i nedstrøms ende er mye større enn i simuleringen. Med mer tid satt av til denne simuleringen, ville det vært mulig å øke kvaliteten på resultatene.

Contents

11 Conclusion 98

12 Further Work 99

References 100

A Input Files 103

B Assignment Text 105

List of Figures

List of Tables

1 Introduction

1.1 Background

The focus on clean energy is increasing, and as a part of this, the Department of Hydraulic and Environmental Engineering at NTNU has started a project on numerical modeling of sediment transport in water reservoirs. The project is financed by the Norwegian Research Council, and aims to develop a three-dimensional numerical model to simulate sediment transport in water reservoirs, including flushing of sediments from reservoirs. The program is called SSIIM, which is an abbreviation for Sediment Simulation In Intakes with Multiblock option, and has been under development by professor Nils Reidar Bøe Olsen since 1990 Olsen (2011b). To test the performance of the program, it is applied to real cases. As Norwegian rivers in general carry very little sediment, Norwegian cases are not able to fully map the abilities and limitation of the program. NTNU has started a cooperation with ICE, the Costa Rican Institute of Electricity, using SSIIM to model sediment transport in the reservoirs for ICE's power plants.

ICE is a governmental Costa Rican company, established in 1949 to promote production and distribution of electrical energy in the country. ICE owns the majority of the hydropower plants in Costa Rica, and accounts at the moment for 78% of the installed capacity (ICE, 2011). The Angostura reservoir is a reservoir facing severe sedimentation problems. The resulting reduction in reservoir volume leads to less flexibility for daily peaking and hence loss of income. To reduce the unwanted effects of sedimentation, a biannual flushing regime was introduced in 2006 to maintain a sufficient live storage. Finding an optimized flushing management strategy may be assisted by numerical modeling.

During her M.Sc. thesis, Lisa Hoven modeled sedimentation and flushing of the Angostura reservoir. Later work has been done by PhD student Stefan Haun and M.Sc. student Sigurd Løvfall.

1.2 Master's Thesis Work

The work consists of three parts: a testing of a simpler engineering tool named the RESCON model, a sediment concentration distribution simulation using SSIIM, and a sediment flushing using SSIIM. Some of the results from the work are used in an article written by Stefan Haun, Nils Reidar Bøe Olsen and me, and quite some time was spent revising the figures for the article. The work on the three parts has been done in series, effactually reducing the time available for the flushing part.

The work on the thesis stared on January 12 2012 and was to be concluded on June 12. As this is the author's first time using the numerical model apart from the basics, quite some time was spent learning the program and understanding its workings.

Part I
Background and Theory

2   Sediment Theory

2.1   Introduction

Flowing water represents a great force that has the power to erode solid and weathered rock and transport the sediment particles over long distances, and finally deposite them when the water becomes stagnant. This chapter is a short introduction to sediment theory, and covers some of the basic physical mechanisms of sediment transport, methods for sediment studies and reservoir management.

2.2   Erosion

2.2.1   Initiation of motion

The forces acting on a particle on the river bed are shown in figure 2.1.
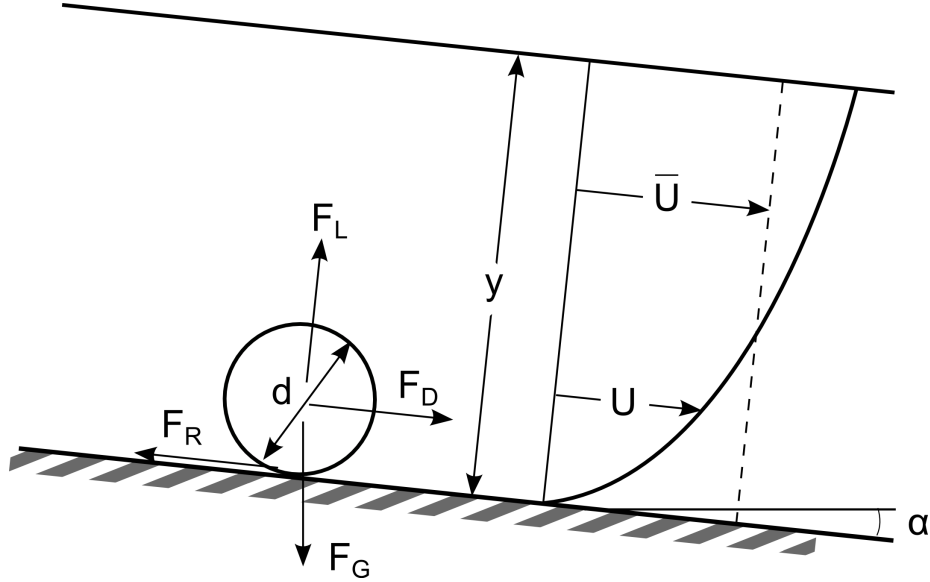
Figure 2.1: Forces acting on a particle

Gravity - buoyancy:

$$F_G = mg = \frac{\pi}{6} g \left(\rho_s - \rho_w \right) d^3 = k_1 g \left(\rho_s - \rho_w \right) d^3 \qquad (2.1a)$$

2

Drag force (Olsen, 2011a):

$$F_D = \frac{\pi}{8} C_D \rho_w \overline{U}^2 d^2 = \frac{\pi}{8} C_D \rho_w \left(I M^2 R^{4/3} \right) d^2 \approx k_2 \tau d^2 \qquad (2.1\mathrm{b})$$

Lift force:

$$F_L = \frac{\pi}{8} C_L \rho_w \overline{U}^2 d^2 \approx k_3 \tau d^2 \qquad (2.1\mathrm{c})$$

Friction force:

$$F_R = (F_G - F_L) \tan\alpha \qquad (2.1\mathrm{d})$$

For force equilibrium, $F_R = F_D$:

$$\left(k_1 g \left(\rho_s - \rho_w \right) d^3 - k_3 \tau_c d^2 \right) \tan\alpha = k_2 \tau_c d^2 \qquad (2.2)$$

The shear stress at equilibrium is the critical shear stress τ_c.
Solving equation 2.2 for the particle diameter:

$$d = \frac{\frac{k_2 \tau_c}{\tan\alpha} + k_3 \tau_c}{k_1 g \left(\rho_s - \rho_w \right)} = \frac{\tau_c}{g \left(\rho_s - \rho_w \right) \frac{k_1 \tan\alpha}{k_2 + k_3 \tan\alpha}} = \frac{\tau_c}{g \left(\rho_s - \rho_w \right) C} \qquad (2.3)$$

where C is the *Shields parameter*. Equation 2.3 is also valid for non-spherical particles because of this parameter. The Shields parameter has been determined experimentally as a function of the particle Reynolds number, and can be found in figure 2.2. For high particle Reynolds numbers, it has constant value of 0.06.
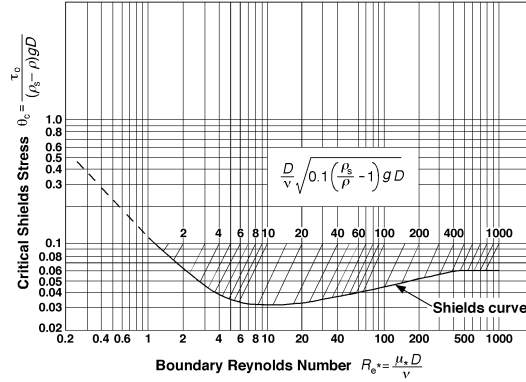
Figure 2.2: Shields curve
(USBR, 2006)

For sloping beds, this value is adjusted by Brooks' correction factor according to equation 2.4. (Olsen, 2011a)

$$K = -\frac{sin\phi sin\alpha}{tan\theta} + \sqrt{\left(\frac{sin\phi sin\alpha}{tan\theta}\right)^2 + cos^2\phi \left[1 - \left(\frac{tan\phi}{tan\theta}\right)^2\right]} \qquad (2.4)$$

In this equation, θ is the bed slope, ϕ is the side slope and α is the deviation angle between the flow and channel direction.

2.3 Sediment Transport

2.3.1 Suspended Sediments and Bed Load

It is common practice to make a distinction between bed load and suspended load. Bed load may be defined as the fraction of the sediment transport that happens on or close to the bed, by the processes of *sliding, rolling* and *saltation*. The origin of the distinction is partly caused by the difficulty to measure the material transported close to the bed. For this reason, some definitions use a reference level under which the material is assumed to be transported as bed load (Vanoni, 2008).

Suspended sediments are finer particles that are held in *suspension* due to turbulent diffusion. For non-turbulent flows, any particle heavier than water will eventually end up on the bed. The particle's terminal *settling velocity* can be found by equating the gravity and drag forces. For small Reynolds numbers, i.e. for particle sizes < 100 μm, this can be found from *Stokes' law*:

$$w = \frac{g\left(\rho_s - \rho_w\right)d^2}{18\nu} \qquad (2.5)$$

where ν is the kinematic viscosity.

In turbulent flows, turbulent diffusion induces an upwards motion because of the concentration gradient, helping to keep the particles in suspension. The most famous vertical distribution profile for suspended sediments was developed by Hunter Rouse. It assumes a parabolic turbulence distribution, and includes the *Hunter Rouse parameter,*

$$z = \frac{w}{\kappa u_*} \qquad (2.6)$$

where $\kappa = 0.41$ is the *von Kármán constant* and u_* is the *shear velocity*. The distribution is calculated relative to a reference level, a, usually 5% of the water depth, and a reference concentration c_a at this level, according to equation 2.7.

$$\frac{c}{c_a} = \left(\frac{(d-y)/y}{(d-a)/a}\right)^z \qquad (2.7)$$

where d is the water depth and y is an arbitrary vertical position.

For particles with low settling velocities, i.e. low z values, the *Rouse distribution* shows an increasingly uniform distribution across the depth, as shown in figure 2.3.

4
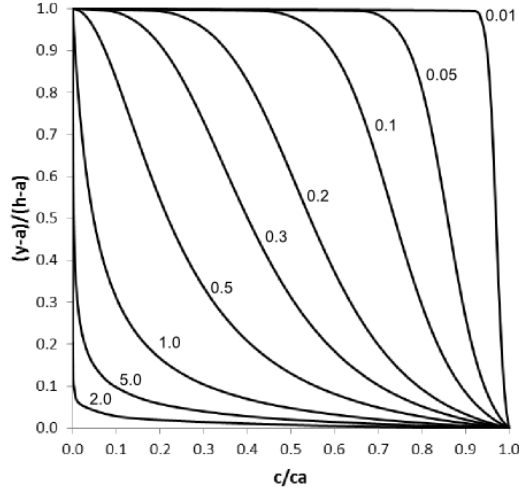
Figure 2.3: Rouse distribution

2.4 Reservoir Sedimentation

Worldwide, there is a storage capacity of over 6,000 km^3 in reservoirs, and between 0.5 and 1.0 percent of this capacity is lost annually due to reservoir sedimentation, although this number is debated by other studies ((White, 2001; Mahmood, 1987)). This reservoir sedimentation rate varies significantly from region to region, because of varying local sediment yield. In areas with high sediment yield, sedimentation is one of the most severe problems with hydropower reservoirs, and sets to a large extent the borders for what is possible with a reservoir. The *capacity-inflow ratio* (CIR) is the reservoir volume divided by the annual water inflow. In areas with sedimentation problems, construction of a reservoir with a CIR between 3 and 30% is often not economically feasible (White, 2001). For larger reservoirs, the reservoir volume will be filled slowly, and the reservoir will function throughout the economic life time of the project. Small reservoirs will have the possibility of sediment management options like flushing or dredging (see section 2.5). However, reservoirs in-between will face a problem: they are not large enough for the life time to pay back the investment costs, nor are they small enough for reservoir management options to be feasible or practicable.

2.4.1 Sediment Delivery to Reservoirs

Sediment yield is the amount of sediments transported by a river through a cross-section annually, divided by the catchment area. The most common unit for sediment yield is tonnes/km^2/year. The sediment yield is hard to estimate, mainly because of the high degree of temporal variation. The concentration of sediments will normally increase with increasing water discharge. The natu-

ral high variability of floods makes the variation in transported sediment even higher.

However, the *carrying capacity* of the river is often not the limiting factor for the sediment transport, but the supply of sediment to the river upstream in the catchment. Land slides into the river are not uncommon, and will lead to a sudden increase in sediment transport. Also, much of the annual inflow of sediments may stem from a single to a few large floods at the beginning of the wet season, when deposited sediments are flushed from the reaches upstream in the catchment. Studies from the United States found that 50% of the annual sediment load is discharged on 1% of the days (Vanoni, 2008). These facts make the variation in transported sediment larger, and more importantly, more unpredictable, as there is often no one-to-one relationship between the water discharge and the actual sediment discharge. As a result, successfully mapping of the sediment inflow into a reservoir requires extensive measurements of sediment inflow over many years to get a representative picture.

Two basic strategies exist for measuring sediment yield:

1. Volume of deposited sediment in reservoirs

2. Continuous monitoring of fluvial sediment discharge

Survey data from reservoirs are generally more accurate because reservoirs collect sediment from all events since their construction, while gauge stations will have under-reported events (Vanoni, 2008).

Bathymetric Surveys

Bathymetric Surveys aim to measure the bed-level across the area of the reservoir at different time-steps to establish the volume of deposited sediment during the time, usually a time-span of several years. Such a survey should also include borings to determine the grain size of the deposits and verify estimates of deposit bulk density. A problem with bathymetric surveys is that they do not reveal the details of spatial or temporal patterns of sediment delivery, which may be needed for some management alternatives (Vanoni, 2008). Bathymetric surveys are usually performed using GPS in combination with an echo sounder.

Surveys on Fluvial Data

Fluvial sediment data is required to determine variations in sediment yield over time. Sediment load is often computed from a long-term discharge record and a *sediment rating curve* that relates concentration to stream flow. The rating curve is constructed from simultaneous discharge and concentration measurements, but the resulting relationship typically exhibits considerable scatter, and the variation in sediment concentration for a given water discharge may vary with up to two log units (Vanoni, 2008).

2.4.2 Sediment Deposition in Reservoirs

A reservoir is usually constructed with a designed life time, often calculated as the storage capacity divided by the annual deposited sediment load. The annual

deposited sediment load is the amount of incoming sediment multiplied with the *trap efficiency* of the reservoir. Depending of the size of the particles, the water flow and geometry of the reservoir, the sediments will be deposited in different places. The finest sediments will still be in suspension when the water leaves the reservoir.

In general, the coarse fraction of the inflowing load creates a *delta deposit* in the entrance area of the reservoir. At the *foreslope* of the delta, the grain size decreases rapidly. Because of backwater effects, deltaic deposits may also be deposited further upstream (Vanoni (2008)). Normally, sediments first fill the deepest part of each cross section, and then spread out to form a flat bed. Nevertheless, depositional patterns may be more complex, as earlier deposits may be moved, large particles may be deposited far downstream during large floods, and there may exist several deltas.

To fully explain sediment deposition patterns, *turbidity currents* need to be addressed A turbidity current results from the higher density of the sediment-loaded inflowing water. The higher density makes the flow move close to the bed, and as the slope of the reservoir increases, gravity pulls the suspended sediment in the bottom water downslope, and the sediment then drags the water with it (Vanoni, 2008). Turbidity currents are the main reason that each cross section is filled from the bottom up. The travel distance for the current may be significant; the longest documented travel distance is 129 km (Vanoni, 2008). If the current reaches the reservoir dam, it will create a lake of muddy water, creating a horizontal deposit of fine sediments. A generalized sketch of reservoir sedimentation geometry is seen in figure 2.4.
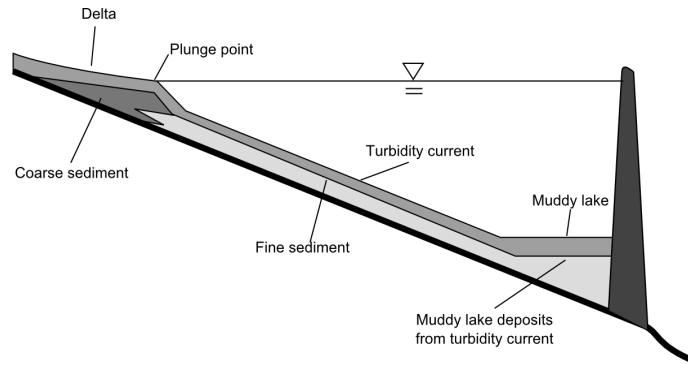
Figure 2.4: Reservoir depositional geometry
based on Vanoni (2008)

An important fact to consider is that as soon as sedimentation begins, it will also start reducing the *live storage* of the reservoir. The delta formation in the upper reach of the reservoir is between the lowest and highest regulated water level, and deposition here will reduce the regulated capacity of the reservoir. Without action, the reservoir will lose both live and dead storage, and eventually become unserviceable.

2.5 Reservoir Management

Although the partitioning and the significance of the terms varies in the literature, and the categories may overlap, sediment management strategies in reservoirs may be divided into seven strategies.

1. Sediment yield reduction: Erosion control to reduce sediment yield from the catchment

2. Sediment storage: Sufficient storage volume for the incoming sediments over time

3. Sediment focusing: Redistribution of sediments in the reservoir by drawdown or dredging

4. Sediment routing: Routing of sediments through or past the reservoir to minimize deposition

5. Sediment dredging: Removal of deposited sediment by traditional dredging

6. Hydrosuction: Dredging powered by gravity

7. Sediment flushing: Removal of deposited sediment by hydraulic flushing

2.5.1 Sediment Yield Reduction

Perhaps the most difficult of the management options, sediment yield reduction may be efficient in prolonging the life time of the reservoir when done successfully. Land-use effects erosion rate substantially, and many areas show increased sediment yield because of increasing farming activity (Vanoni, 2008). Erosion rate varies considerably within a watershed, and a small parcel of the total area will often be responsible for most of the sediment yield. As a result, identifying the major contributors to the sediment yield is essential in order to maximize the cost-efficiency of the measures.

2.5.2 Sediment Storage

Traditionally, sedimentation has been managed by providing a storage volume large enough to postpone problems for 50 to 100 years. As described in earlier sections, sediment problems are not always successfully delayed in this way, as sedimentation to a large degree happens in the live storage volume. The most-used method to increase the storage volume of an existing reservoir, is to raise the dam. The sediment storage may also be in a separate sedimentation dam upstream. (Vanoni, 2008)

2.5.3 Sediment Focusing

As shown in figure 2.4, the depositional pattern in a reservoir is not favorable. One way of prolonging the life time of the reservoir is to redistribute the sediments so that they do not occupy the live storage of the reservoir. This may be accomplished by adapting an operational regime that deposits the sediment further downstream in the reservoir, or by mechanically relocating the sediments by flushing or dredging.

2.5.4 Routing

Another way to handle sediment problems is to *bypass* sediments when the load is high. Run of the river hydropower plants or reservoirs for daily peaking can usually benefit from shutting down during high floods to avoid the high sediment loads. There are different ways to route the sediments past the reservoir.

One way to achieve sediment routing is to place the pool offstream and divert only relatively clear water from moderate flows into storage. To achieve additional sediment exclusion, the intake may be closed during floods with high sediment concentration (Vanoni, 2008).

The reason for sedimentation in reservoirs is that the water velocity, and hence the transport capacity, is reduced. To avoid major sedimentation events during high sediment-loaded floods, the reservoir level may be *drawn down*. By opening *high-capacity gates*, the water level will be reduced, and velocities will be kept sufficiently high to pass the sediments through the reservoir. This may be done when anticipating a large flood, either by *hydrograph prediction* or based on seasonality of sediment floods (Vanoni, 2008). This technique is also named *sluicing*.

Yet another way to achieve sediment routing is to exploit the sediment transport by turbidity currents. In the cases where these currents transport fine sediments all the way to the dam, it may be possible to open bottom gates to flush the sediments. At the Cachí hydropower reservoir in Costa Rica, studies have showed that 72% of the total inflowing load was either deposited along or transported through the original river channel at the bottom of the reservoir, making it easier to vent (Vanoni, 2008).

2.5.5 Dredging

Dredging is the process of removing sediment from underwater. We may distinguish between dredging and hydrosuction by naming dredging the traditional dredging powered by an external pump. Dredging may be used to sustain the volumetric capacity, or solely to remove sediments from around an intake to improve functionality (Vanoni, 2008). As dredging normally does not cover the whole reservoir, it is not necessarily a sustainable management technique, because sediments will build up over the years (Palmiere et al., 2003).

2.5.6 Hydrosuction

Sediment sluicing is dredging powered by the pressure difference from the reservoir level to downstream of the dam. As the external power required for traditional dredging can make the process expensive, sluicing may be a more economical way to achieve the same goal where it is applicable. To ensure proper sluicing, an externally powered water jet may still be needed to dissolve deposited sediments. (Palmiere et al., 2003)

A problem with both sediment flushing, dredging and sluicing is the highly increased sediment concentration in the reaches downstream during the process, which may reduce the livelihood for many aquatic organisms (Vanoni, 2008).

2.5.7 Flushing

Because of its relevance to this thesis, flushing is more extensively described than the other methods. Flushing is a technique than combines drawdown of the water level with an increase in the water flow to achieve a maximized erodible power, allowing for previously deposited sediments to be discharged from the reservoir. The lowering of the water surface is often done in two steps, where the first involves a slow decrease to the lowest regulated water level, while producing power, and the second involves opening of the low-level flushing gates to rapidly decrease the water level until the reservoir is empty. The water level is then maintained at this level for hours, days, or weeks, depending on the time needed to remove the determined amount of sediment. Usually the process is done annually, but in some cases the interval between flushing events may be several years (White, 2001).

The drawdown may be complete, restoring the flow to preimpounded conditions to reach river flow, or partial, depending on the pressure of the water as well as the velocities to erode the material. The latter method is a variation of sediment focusing, because it will not under normal circumstances be efficient enough to remove the sediment from the reservoir, but rather redistribute it within the water volume. A partial drawdown may also be performed as a sediment routing, when the incoming sediment concentrations are high, for example in association with an upstream reservoir flushing.

Reservoir flushing will be effective along the original river thalweg, or a central flushing channel in case of a natural lake, but the sides of the reservoir will normally remain unaffected. As a result, flushing will be much more efficient in narrow gauge reservoirs than in reservoirs over wide floodplains. Flushing is often performed in the wet season to provide a high flow and later a rapid refilling of the reservoir (Vanoni, 2008). Coarse sediment deposited in the delta area may still be difficult to flush, and a fully sustainable original reservoir volume is hard to obtain.

Successful flushing is dependent on many factors:

The hydrological size of the reservoir is perhaps the most important element. Reservoirs that are small compared to the annual inflow will have a greater chance of a successful flushing. In larger reservoirs, a complete draw-

down involves a great chance of not being able to refill the reservoir during the wet season. A ratio of storage capacity to mean annual inflow of 30% is often used as a boundary between hydrologically large and small reservoirs. For a ratio lower than 30%, there is a reasonable probability of achieving sufficient flow for annual flushing of the reservoir, and the lower the ratio is, the higher the probability. It is important to note that large reservoirs that are impracticable to flush, may be more practicable as sedimentation reduces the storage volume. (White, 2001)

The shape of the reservoir also has a large influence. Narrow reservoirs with steep side-slopes are by far the most favorable for flushing. This is aided additionally if the bed gradient is steep. Broader, shallow reservoirs are much more difficult to flush, as the flushing flow tends to follow a narrow flushing channel, usually in the old river reach in the reservoir. In a narrow reservoir, this channel will cover most of the reservoir width, effectively flushing most of the sediments, while in a broad reservoir, only a small portion of the sediment will be flushed. In addition, the drawdown during flushing, and sometimes other times of the year, will leave the dried out sediments to consolidate, making future flushing even more difficult. The geometry of the flushing channel, e.g the bottom slope, width and side slope, are generally a function of sediment characteristics, the gradient of the valley and the flushing discharge, but may also be limited by the reservoir geometry (White, 2001).

It is also essential to have control over the flushing discharge. When the reservoir has been emptied, there still needs to be a sufficient inflow of water to the reservoir to flush the sediments for the duration of the flushing.

A successful flushing is dependent on low-level outlets with enough capacity. The outlets should be on level with the original riverbed at the dam to keep control of the bed level. A higher outlet will both limit the drawdown during the flushing and the available head to achieve a certain discharge. The discharge should also be high enough to allow lowering of the water level to the desired level. A commonly used rule of thumb for hydrologically small reservoirs flushed off-season is that the low-level gates should be able to pass at least twice the mean annual inflow at a drawdown by at least 50% (White, 2001). This criterion is not valid for larger reservoirs, where the time needed for a drawdown is much longer and the process may be interrupted by periods of high flow.

For flushing to be a sustainable sediment management method, the amount of flushed sediment needs to be equal to the amount that has settled between each flushing event. For this reason, the amount of sediment that enters the reservoir, along with the reservoir trap efficiency, are important for the success of the flushing. When the sediment inflow is high, the time needed to flush all the sediment may be extensive. For reservoirs in catchments with lower sediment yield, the flushing time may be reduced, or the frequency of flushing events may be reduced. This, however, needs to take into account the risk of sediment consolidation if the time between flushings is very long, or if the water level is reduced sufficiently for the sediment to dry up. Finer sediments are less likely to consolidate (White, 2001).

11

3 The RESCON Model

3.1 Introduction

The RESCON research project was invited by the World Bank in 1999 to develop an approach to the assessment and promotion of sustainable management of reservoirs, with special emphasis on the economic evaluation of sediment management and the promotion of sustainable development (Palmiere et al., 2003). The name RESCON is a portmanteau of reservoir and conservation.

A full feasibility study on the effects of sediment management strategies on large dam and reservoir systems requires great time and resources and a comprehensive acquisition of data. The RESCON approach is a tool kit that can be used for decision making purposes at the policy level, using readily available data, such as reservoir geometry, hydrology, and economic parameters. The tool is best used on a portfolio of projects, to evaluate which options to pursue and which sediment management alternative is most suitable. The approach also includes a method of including an environmental safeguard.

Little information is published on the economics of reservoir sedimentation and its implication for sustainable development. The purpose of the RESCON research is to develop a framework to assess the feasibility of sediment management to prolong the lifetime of dams indefinitely.

3.2 The RESCON Model

The RESCON model is a computer model of the RESCON approach developed as a demonstration tool (Palmiere et al., 2003).

The model assesses the economic feasibility of flushing, hydrosuction, traditional dredging, and trucking, and compares them to the "do nothing" scenario. Watershed management, sediment bypass and operating rules are not assessed in the program.

The aim of the program is to select a technologically feasible sediment management strategy that also maximizes the net economic benefits. Written as a macro enabled Excel workbook, the program test flushing and hydrosuction for technical feasibility, and then proceeds to an economic optimization algorithm. The program assumes that trucking and traditional dredging as technically feasible, leaving this evaluation to the user.

In contrast to the design life approach, the RESCON approach uses the life cycle management approach, striving for sustainable management of the reservoir, or if this is not possible, decommission is planned at the optimal time, and a retirement fund is established.

The main program structure is outlined in figure 3.1.
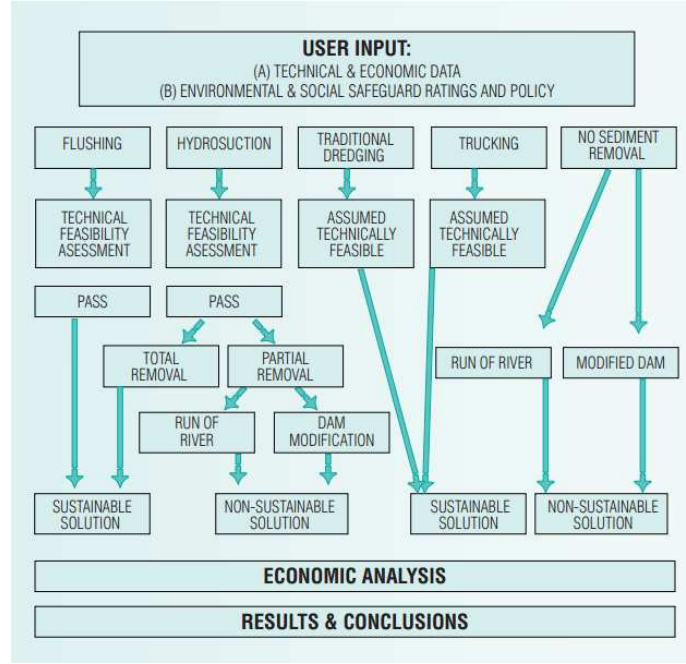
Figure 3.1: RESCON program structure
(Palmiere et al., 2003)

3.3 Flushing

For the purpose of this thesis, the whole RESCON is not of interest. The economic value is not to be assessed, and other sediment management strategies than flushing are out of the scope.

The flushing module in the model is based on (Atkinson, 1996). This article develops criteria which require readily available data to assess the feasibility of flushing sediment from a reservoir. The proposed criteria are:

- Sediment balance ratio, SBR:

$$SBR = \frac{\text{sediment mass flushed annually}}{\text{sediment mass deposited annually}} \quad (3.1)$$

- Long term capacity ratio, LTCR:

$$LTCR = \frac{\text{sustainable capacity}}{\text{original capacity}} \quad (3.2)$$

- Drawdown ratio, DDR:

$$DDR = \frac{\text{flow depth for the flushing water level}}{\text{flow depth for the normal impounding level}} \quad (3.3)$$

13

- Flushing width ratio, FDR:

$$FDR = \frac{\text{predicted flushing width}}{\text{representative bottom width of reservoir}} \tag{3.4}$$

- Top width ratio, TWR:

$$TWR = \frac{\text{top width of scoured valley}}{\text{actual top width}} \tag{3.5}$$

For details on each criterion, see the original article.

These criteria are used in the RESCON model to assess whether flushing of the reservoir is feasible or not, and the long term capacity and economic value of the management strategy.

To estimate the flushed sediment volume during a flushing event, Atkinson's model uses a transporting capacity from an empirical method developed at the Tsinghua University in China, as there are few other good methods in the literature (Atkinson, 1996). The sediment carrying capacity is calculated according to equation 3.6.

$$Q_{fs} = \psi \frac{Q_f^{1.6} S^{1.2}}{W^{0.6}} \tag{3.6}$$

where Q_s is the sediment transporting capacity in t/s, ψ is an empirical sediment parameter, Q_f is the flushing discharge in m^3/s, S is the energy slope, and W is the top width of the flushing channel in m.

As the method is to be applied to unflushed reservoirs, the flushing channel width may be unknown. Based on a curve fit from empirical data, equation 3.7 may be used. In case the width of the reservoir at the flushing water level is lower than this value, the width in equation 3.6 is set to the lower value of the calculated flushing channel width and the surface width of the reservoir.

$$W_f = 12.8 Q_f^{0.5} \tag{3.7}$$

where Q_f is the flushing discharge in m^3/s.

The slope is calculated as the difference between the highest regulated water level and the water level during flushing, divided by the reservoir length.

$$S = \frac{El_{max} - El_f}{L} \tag{3.8}$$

The removed sediment volume during the flushing event is then the flushing discharge multiplied with the flushing time, divided by the deposited sediment density.

$$V_f = \frac{Q_f \Delta t}{\rho_{dep}} \tag{3.9}$$

14

3.4   Limitations

Because the model does not have an adequate method of dealing with incoming sediment, the RESCON model is not suited for sediment pass-through.

The output from the flushing module is only the volume of flushed sediment. As there is only a limited input of reservoir geometry and the flushing algorithm used gives only a number, there is no way to get the distribution pattern of the eroded sediment.

4 Computational Fluid Dynamics

4.1 Introduction

The Navier-Stokes equations, which are the governing equations for Newtonian fluid dynamics, have been known for almost 200 years. The equations are a set of coupled nonlinear partial differential equations, and their complexity makes them almost impossible to solve for most real situations. In fact, it has net yet been proven mathematically that an analytical solution always exists or that if it does, it does not contain any singularities. However, the great number of practical applications for the equations has forced an ongoing research on development of new and better solution methods. Since analytical solution methods do not exist, the equations are solved numerically. The field of numerical solution of fluid equations is termed computational fluid dynamics. With the steady advancement of computer power, improving CFD software and an increasing base of trained users, this branch of fluid dynamics offers an increasingly attractive alternative or supplement to physical model studies. Although the aerospace industry has integrated CFD techniques in the design process since the 1960s, its application as an engineering tool in the hydraulic sciences has not had the same development (Versteeg and Malalasekera, 2007).

Fletcher (1996) lists five major advantages of CFD compared with physical model studies:

1. Reduction in design and development time

2. Possibility of simulating flow conditions that are not reproducible in physical model studies

3. More detail and comprehensive information

4. Increasingly more cost-effective

5. Lower energy consumption

CFD is based around the numerical algorithms that can solve the govering equations. However, the complexity of geometry and input data requires a method of treating the data before the calculations begin. In addition, the often immens amounts of results needs to be represented in a way that is meaningful to the user. For these reasons, a complete CFD program needs both a *pre-processor*, a *solver*, and a *post-processor*, although the different elements may be separate programs. The three program elements will be shortly described in the following.

4.1.1 Pre-Processor

A pre-processing consists of a practical user-interface that allows for input of the flow problem and a means of transforming the problem into a form that can be interpreted by the solver. The user will define the computational domain, select the equations that are to be modeled, generate a grid onto which the equations

are to be solved, and define the initial and boundary conditions. According to Versteeg and Malalasekera (2007), over 50% of the time spent in industry on a CFD project is used on domain geometry and grid generation. This illustrates the importance and challenge related to this phase of the process.

4.1.2 Solver

The solver approximates the flow variables with simple functions and converts the governing equations into ordinary differential equations by discretization, and solves the set of algebraic equations. There are three distinct classes of numerical solution techniques, finite difference, finite elements and finite volume, which are shortly described in section 4.4.2.

4.1.3 Post-Processor

The results of the calculations performed by the solver is only a whole lot of numbers. In order for this to give any meaning to the user, it needs to be represented in a graphical way, and this is the purpose of a post-processor. The leading commercial CFD packages have advanced visualization tools that give vector plots, line and shaded contour plots, surface plots in 2D or 3D, particle tracking and animations. (Versteeg and Malalasekera, 2007)

The following text will describe in more detail the principles and processes of CFD.

4.2 Governing Equations

The fundamental laws governing transport phenomena in moving fluids are:

1. Conservation of mass

2. Conservation of momentum (Newton's second law)

3. Conservation of energy (first law of thermodynamics)

There are two possible ways to apply these laws to the fluid:

1. The particle approach

2. The continuum approach

The particle approach looks at a group of particles, and the laws are applied to describe particle motion. The motion of the fluid is then described as the statistically averaged motion of the particles. Because of the high number of fluid particles in a volume of fluid, this method is often unmanageable.

In the continuum approach, the laws are applied to a control volume of the fluid that contains a large number of particles, assuming the statistical averaging is already performed, and the fluid acts as a continuum. In the engineering sciences, the movements of a single molecule are seldom of particular interest, and its influence on the behavior of the fluid as a whole is negligible. However,

some of the processes on micro level affect the properties and behavior of the fluid, and this information is lost if the laws are applied directly to the control volume. To recover this, experimentally determined fluid parameters like viscosity, mass diffusivity and thermal conductivity are applied. (Date, 2005)

In the following derivations, we consider an infinitesimally small element fixed in space, ordered according to the Cartesian coordinates.

4.2.1 Conservation of Mass

The law of conservation of mass states that accumulation rate of mass = mass rate in - mass rate out.

$$\dot{M}_{ac} = \dot{M}_{in} - \dot{M}_{out} \tag{4.1}$$

$$\dot{M}_{ac} = \frac{\partial}{\partial t} \left(\rho \Delta V \right) \tag{4.2a}$$

$$\dot{M}_{in} = \left(\rho u_1 \Delta x_2 \Delta x_3 \right)|_{x_1} + \left(\rho u_2 \Delta x_3 \Delta x_{31} \right)|_{x_2} + \left(\rho u_3 \Delta x_1 \Delta x_2 \right)|_{x_3} \tag{4.2b}$$

$$\dot{M}_{out} = \left(\rho u_1 \Delta x_2 \Delta x_3 \right)|_{x_1 + \Delta x_1} + \left(\rho u_2 \Delta x_3 \Delta x_1 \right)|_{x_2 + \Delta x_2} + \left(\rho u_3 \Delta x_1 \Delta x_2 \right)|_{x_3 + \Delta x_3} \tag{4.2c}$$

Dividing each term by the volume, $\Delta x_1 \Delta x_2 \Delta x_3$, we get:

$$\frac{\partial \rho}{\partial t} = \frac{\left(\rho u_1 \right)|_{x_1} - \left(\rho u_1 \right)|_{x_1 + \Delta x_1}}{\Delta x_1} + \frac{\left(\rho u_2 \right)|_{x_2} - \left(\rho u_2 \right)|_{x_2 + \Delta x_2}}{\Delta x_2}$$

$$+ \frac{\left(\rho u_3 \right)|_{x_3} - \left(\rho u_3 \right)|_{x_3 + \Delta x_3}}{\Delta x_3} \tag{4.3}$$

Letting Δx_1, Δx_2, $\Delta x_3 \to 0$, this can be written in conservative differential form:

$$\frac{\partial \rho}{\partial t} + \frac{\partial}{\partial x_1} \left(\rho u_1 \right) + \frac{\partial}{\partial x_2} \left(\rho u_2 \right) + \frac{\partial}{\delta \partial x_3} \left(\rho u_3 \right) = 0 \tag{4.4}$$

or short:

$$\frac{\partial \rho}{\partial t} + \frac{\partial}{\partial x_i} \left(\rho u_i \right) = 0 \tag{4.5}$$

Expanding the derivatives, this can be written in non-conservative form:

$$\frac{\partial \rho}{\partial t} + u_1 \frac{\partial \rho}{\partial x_1} + u_2 \frac{\partial \rho}{\partial x_2} + u_3 \frac{\partial \rho}{\partial x_3} = -\rho \left(\frac{\partial u_1}{\partial x_1} + \rho \frac{\partial u_2}{\partial x_2} + \rho \frac{\partial u_3}{\partial x_3} \right) \tag{4.6a}$$

or short:

$$\frac{D\rho}{Dt} = -\rho \frac{\partial u_i}{\partial x_i} \tag{4.6b}$$

18

4.2.2 Conservation of Momentum

Newton's second law in a given direction:

Accumulation rate of momentum = momentum rate in - momentum rate out + sum of forces acting on the CV

$$Mom_{ac} = Mom_{in} - Mom_{out} + F_{CV} \tag{4.7}$$

in x direction, this can be written as:

$$Mom_{ac} = \frac{\partial}{\partial t}\left(\rho \Delta V u_1\right) \tag{4.8a}$$

$$Mom_{in} = \left(\rho \Delta x_2 \Delta x_3 u_1\right)|_{x_1} + \left(\rho \Delta x_3 \Delta x_1 u_2\right)|_{x_2} + \left(\rho \Delta x_1 \Delta x_2 u_3\right)|_{x_3} \tag{4.8b}$$

$$Mom_{out} = \left(\rho \Delta x_2 \Delta x_3 u_1\right)|_{x_1 + \Delta x_1} + \left(\rho \Delta x_3 \Delta x_1 u_2\right)|_{x_2 + \Delta x_2}$$

$$+ \left(\rho \Delta x_1 \Delta x_2 u_3\right)|_{x_3 + \Delta x_3} \tag{4.8c}$$

$$F_{CV} = -\left(\sigma_1|_{x_1} - \sigma_1|_{x_1 + \Delta x_1}\right)\Delta x_2 \Delta x_3 + \left(\tau_{11}|_{x_1 + \Delta x_1} - \tau_{11}|_{x_1}\right)\Delta x_2 \Delta x_3$$

$$+\left(\tau_{21}|_{x_2 + \Delta x_2} - \tau_{21}|_{x_2}\right)\Delta x_3 \Delta x_1 + \left(\tau_{31}|_{x_3 + \Delta x_3} - \tau_{31}|_{x_3}\right)\Delta x_1 \Delta x_2 + \rho f \Delta x_1 \Delta x_2 \Delta x_3 \tag{4.8d}$$

where f_i is a *body force* (gravity or other) per unit mass acting on the body, σ_1 is the *tensile normal stress* and τ_{ij} are the *shear stresses* acting on the surfaces.

Dividing by the volume and letting Δx_1, Δx_2, $\Delta x_3 \to 0$, it can be shown that:

In x direction:

$$\frac{\partial}{\partial t}\left(\rho u_1\right) + \frac{\partial}{\partial x_1}\left(\rho u_1 u_1\right) + \frac{\partial}{\partial x_2}\left(\rho u_2 u_1\right) + \frac{\partial}{\partial x_3}\left(\rho u_3 u_1\right)$$

$$= \frac{\partial}{\partial x_1}\left(p_1\right) + \frac{\partial}{\partial x_2}\left(\tau_{11}\right) + \frac{\partial}{\partial x_2}\left(\tau_{21}\right) + \frac{\partial}{\partial x_3}\left(\tau_{31}\right) + \rho f_1 \tag{4.9a}$$

In y direction:

$$\frac{\partial}{\partial t}\left(\rho u_2\right) + \frac{\partial}{\partial x_1}\left(\rho u_1 u_2\right) + \frac{\partial}{\partial x_2}\left(\rho u_2 u_2\right) + \frac{\partial}{\partial x_3}\left(\rho u_3 u_2\right)$$

$$= \frac{\partial}{\partial x_1}\left(\tau_{12}\right) + \frac{\partial}{\partial x_2}\left(p_2\right) + \frac{\partial}{\partial x_2}\left(\tau_{22}\right) + \frac{\partial}{\partial x_3}\left(\tau_{32}\right) + \rho f_2 \tag{4.9b}$$

In z direction:

$$\frac{\partial}{\partial t}\left(\rho u_3\right) + \frac{\partial}{\partial x_1}\left(\rho u_1 u_3\right) + \frac{\partial}{\partial x_2}\left(\rho u_2 u_3\right) + \frac{\partial}{\partial x_3}\left(\rho u_3 u_3\right)$$

$$= \frac{\partial}{\partial x_1}\left(\tau_{13}\right) + \frac{\partial}{\partial x_2}\left(\tau_{23}\right) + \frac{\partial}{\partial x_3}\left(p_3\right) + \frac{\partial}{\partial x_3}\left(\tau_{33}\right) + \rho f_3 \qquad (4.9c)$$

Substituting equation 4.4 into the momentum equations, equation 4.9a can be written in reduced non-conservative form, and similarly for the other directions:

$$\rho\frac{Du_1}{Dt} = \frac{\partial}{\partial x_1}\left(p_1\right) + \frac{\partial}{\partial x_2}\left(\tau_{21}\right) + \frac{\partial}{\partial x_3}\left(\tau_{31}\right) + \rho f_1 \qquad (4.10)$$

Equation 4.4 and equations 4.9 a-c define particle motion completely, but have nine unknowns when *complementary stresses* are taken into account, which can not be solved by four equations. (Date, 2005)

Stokes' Stress Law   For *isotropic Newtonian fluids,* whose stress is linearly proportional to the strain rate and equal in all directions, *Stokes' stress law* applies, yielding a relationship between the stresses and the velocity gradients (Versteeg and Malalasekera, 2007).

$$\tau_{ij} = \lambda\left(\nabla\cdot\mathbf{u}\right) + 2\mu\frac{\partial u_i}{\partial x_i}, \; i = j \qquad (4.11)$$

$$\tau_{ij} = \mu\left(\frac{\partial u_j}{\partial x_i} + \frac{\partial u_i}{\partial x_j}\right) \; i \neq j \qquad (4.12)$$

This can be written in general using *Kronecker's delta*:

$$\tau_{ij} = \left(1 - \delta_{ij}\right)\lambda\left(\nabla\cdot\mathbf{u}\right) + \mu\left(\frac{\partial u_j}{\partial x_i} + \frac{\partial u_i}{\partial x_j}\right) \qquad (4.13)$$

- μ is the first coefficient of viscosity

- λ is the second coefficient of viscosity, associated with viscous effects from volume changes. The value of λ (and even its sign) are not known with certainty, and the most common approximation is $\lambda = -\frac{2}{3}\mu$. However, even for compressible flows, this term is negligible compared to the other terms, and is usually set to zero. (Anderson, 1995)

The three momentum equations in conservative form can be written compactly in tensor notation as:

$$\frac{\partial}{\partial t}\left(\rho u_i\right) + \frac{\partial}{\partial x_j}\left(\rho u_i u_j\right) = \frac{\partial}{\partial x_j}\left(-p\delta_{ij} + \left(1 - \delta_{ij}\right)\lambda\left(\nabla\cdot\mathbf{u}\right) + \mu\left(\frac{\partial u_j}{\partial x_i} + \frac{\partial u_i}{\partial x_j}\right)\right) + \rho f_i$$
$$(4.14)$$

or, ignoring the volumetric viscosity coefficient,

$$\frac{\partial}{\partial t}\left(\rho u_i\right) + \frac{\partial}{\partial x_j}\left(\rho u_i u_j\right) = \frac{\partial}{\delta \partial x_j}\left(-p\delta_{ij} + \mu\left(\frac{\partial u_j}{\partial x_i} + \frac{\partial u_i}{\partial x_j}\right)\right) + \rho f_i \qquad (4.15)$$

For incompressible flow, where ρ is a property of the fluid and not of the state, we have four unknowns: u_1, u_2, u_3 and p. Combined with the continuity equation, equation 4.4, we have a total of four equations with four unknowns, so the system can be solved.

4.2.3 Conservation of Scalar Quantities

Similarly to the derivations above, we may cast the conservation laws of any scalar quantity for the fluid continuum. These scalar quantities may be e.g. concentrations of species transported in the fluid or the fluid temperature.

$$\frac{\partial}{\partial t}\left(\rho\phi\right) + \frac{\partial}{\partial x_i}\left(\rho u_i\phi\right) = \frac{\partial}{\partial x_i}\left(\lambda\frac{\partial\phi}{\partial x_i}\right) + \rho S_\phi \qquad (4.16)$$

where λ is the diffusivity coefficient of quantity ϕ, and S_ϕ is a source term. Assigning temperature or internal energy to the quantity ϕ, we get the energy equation, which is a manifestation of the first law of thermodynamics, the principle of conservation of energy.

For compressible flow, this is needed, as ρ is changing with the flow, so there are more unknowns than equations. However, this introduces yet another unknown, and an *equation of state*, e.g. the ideal gas law, i.e. $p = \rho RT$, or the caloric equation of state, i.e. $e = c_v T$, must be introduced to establish the relationship between the unknowns and close the system mathematically (Anderson, 1995).

The source terms will vary strongly with the quantity modeled. Chemical quantities arise and decay by chemical reactions, while energy has source terms from external heat, mechanical work, contributions from chemical energy and others. Depending on the terms included and the quantity modeled (e.g. total energy, enthalpy of temperature) the equation are expressed differently.

4.2.4 Forms of the Equations

Depending on the literature, the Navier-Stokes equations may be the name of only the momentum equations, or the full set of continuity, momentum and energy equations.

All the equations may be written in different forms. When the derivation of the equations is done as above, with an infinitesimally small element, the directly obtained equations are on differential form. In contrast, deriving the equations from an arbitrarily shaped control volume yields equations on integral form. The differential form requires mathematical continuity of the flow because the variables need to be differentiable. The integral form, however, is not limited by this, which may be an advantage when modeling e.g. shock waves (Anderson, 1995).

Another distinction comes from the perspective of the derivation. When looking at an element fixed in space, and the fluxes through its walls, the equations are said to be on conservation form, or divergence form because of the div operator that appears. In contrast, a derivation following the fluid element with the flow gives a non-conservative form. The different forms of the continuity equation are displayed in table 4.1. All the four forms of the equations state the same, and may be transcribed to any of the other forms. (Anderson, 1995)

Table 4.1: Four forms of the continuity equation

	Conservative	Non-conservative
Differential	$\frac{\partial}{\partial t} + \nabla \cdot (\rho \mathbf{u}) = 0$	$\frac{D\rho}{Dt} + \rho \nabla \cdot \mathbf{u} = 0$
Integral	$\frac{\partial}{\partial t} \iiint_V \rho dV + \iint_S \rho \mathbf{u} \cdot \mathbf{dS} = 0$	$\iiint_V \frac{\delta \rho}{\delta t} dV + \iint_S \rho \mathbf{u} \cdot \mathbf{dS} = 0$

An advantage with the conservative form is that all the equations may be written in the same manner. As a result, the full set of equations may be written as a single vector equation::

$$\frac{\partial U}{\partial t} + \frac{\partial F_1}{\partial x_1} + \frac{\partial F_2}{\partial x_2} + \frac{\partial F_3}{\partial x_3} = G \qquad (4.17)$$

where U, F_1, F_2, F_3 and G are column vectors. F_1, F_2, F_3 are flux terms, and G is a source term. U is often named a solution term, because the variables here are the direct results of the numerical calculations.

4.3 Turbulence Modeling

4.3.1 Turbulence

Turbulence is an irregular motion that appears when fluids flow past solid surfaces or when neighboring streams of the same fluid flow past each other Turbulence develops as an instability of laminar flow, when the Reynolds number is large. Mathematically, these instabilities may be seen as interactions between the nonlinear inertial terms and viscous terms in the Navier-Stokes equations (Wilcox, 1995). For almost any engineering application, the Reynolds number is significantly large to make the flow turbulent, which displays the need for handling of turbulence.

Turbulence manifests itself as three-dimensional rotating eddies in the flow, where the characteristic velocity and length of the largest eddies are of the same order as for the mean flow, e.g. for a boundary layer (Rodi, 1984). These large eddies take energy from the mean flow by a process called *vortex stretching*. The rotation of the large eddies again creates motion at smaller transverse length scales, and gives energy to smaller eddies by means of more vortex stretching (Versteeg and Malalasekera, 2007). This gives rise to a cascade of energy from

the largest eddies continuously down to the smallest, at the *Kolmogorov micro scale*, where the energy is lost to heat through molecular viscosity (Wilcox, 1995). In addition to creating the smaller eddies, the larger eddies also strongly influence the mean flow.

Turbulent eddies are inherently three-dimensional, as there is no satisfactory two-dimensional approximation. Another interesting property of turbulent flow is its enhanced diffusivity. Transfer of mass, momentum and heat is greatly increased by the turbulent diffusion (Wilcox, 1995).

Because of the large range of length and time scales on which turbulent eddies exist, a physically meaningful simulation of turbulent flow will normally require hundreds or thousands of cells in the spatial directions, in addition to a temporal interval of less than a millisecond (Rodi, 1984; Versteeg and Malalasekera, 2007). For normal engineering problems, this is not affordable, and historically it has been impossible due to limited computational power. The practical interest in averaged values supposes the definition of a time-averaged version of the Navier-Stokes equations. *Reynolds decomposition* splits the instantaneous velocity into a time-averaged value and an oscillating value with a mean of zero, equation 4.18.

$$\mathbf{u} = \mathbf{U} + \mathbf{u}' \tag{4.18}$$

By algebraic manipulation of the former equations, it is possible to reduce the mass, momentum and energy equations into time-averaged versions. The *Reynolds-averaged Navier-Stokes equations* (RANS) are displayed in equations 4.19 to 4.21, where equation 4.21 is the transport equation for temperature or concentration.

$$\frac{D\rho}{Dt} = -\rho \frac{\partial u_i}{\partial x_i} \tag{4.19}$$

$$\frac{\partial}{\partial t}(\rho U_i) + \frac{\partial}{\partial x_j}(\rho U_i U_j) = \frac{\partial}{\delta \partial x_j}\left(-P\delta_{ij} + \mu\left(\frac{\partial I_j}{\partial x_i} + \frac{\partial U_i}{\partial x_j}\right) - \rho\overline{u_i' u_j'}\right) + \rho f_i \tag{4.20}$$

$$\frac{\partial}{\partial t}(\rho\phi) + \frac{\partial}{\partial x_i}(\rho U_i \phi) = \frac{\partial}{\partial x_i}\left(\lambda\frac{\partial\phi}{\partial x_i} - \rho\overline{u_i' \varphi'}\right) + \rho S_\phi \tag{4.21}$$

In the process of time-averaging, however, six additional unknowns are introduced in the momentum equations, and additional three in the transport equation for energy or other quantities. The former stresses are called *Reynolds stresses*, and the latter *Reynolds Fluxes*, and have the form of last terms in the parentheses in equation 4.20 and 4.21. The additional turbulent terms were introduced because of the nonlinearity in the Navier-Stokes equations. There is no way of eliminating these terms by simply taking higher-order moments, because we introduce new unknowns at each level (Wilcox, 1995). The process of expressing these unknowns by approximations in terms of the mean properties of the flow gives rise to the existence of turbulence models.

4.3.2 Turbulence Models

According to Wilcox (1995), an ideal turbulence model is one that "introduces the minimum amount of complexity while capturing the essence of the relevant physics". For a turbulence model to be useful in general purpose CFD, it must have a wide applicability, be accurate, simple and computationally economical (Versteeg and Malalasekera, 2007).

One of the oldest proposal for modeling the turbulent stresses is the *Boussinesq assumption*. This is called the *eddy-viscosity concept* and assumes that the turbulent stresses are proportional to the mean-velocity gradients, analogous to the viscous stresses in laminar flows (Rodi, 1984). This may be expressed as:

$$- \rho \overline{u'_i u'_j} = \rho \nu_t \left(\frac{\partial U_i}{\partial x_j} + \frac{\partial U_j}{\partial x_i} - \frac{2}{3} \frac{\partial U_k}{\partial x_k} \delta_{ij} \right) - \frac{2}{3} \rho k \delta_{ij} \tag{4.22}$$

which for incompressible flow reduces to

$$- \rho \overline{u'_i u'_j} = \rho \nu_t \left(\frac{\partial U_i}{\partial x_j} + \frac{\partial U_j}{\partial x_i} \right) - \frac{2}{3} \rho k \delta_{ij} \tag{4.23}$$

where $k = \frac{1}{2} \left(u_1^2 + u_2^2 + u_3^2 \right)$. In equation 4.23, ν_t is the turbulent or eddy viscosity, which in contrast to molecular viscosity ν is a property of the flow field, not the fluid. Therefore, ν_t varies strongly in space and time, and there is still a need to determine the value of this property. In contrast to the nature of turbulence, the eddy viscosity is a scalar quantity, which does not take into account the anisotropic properties of the turbulence. Some models, however, introduce different eddy viscosity in different directions (Rodi, 1984).

In the same manner, the turbulent eddy-diffusivity is assumed to be related to the gradient of the transported quantity:

$$- \rho \overline{u'_i \varphi'} = \rho \Gamma \frac{\partial \phi}{\partial x_i} \tag{4.24}$$

where Γ is the turbulent diffusivity of heat or mass. Γ is also a property of the flow field, and is related to the eddy viscosity by the ratio:

$$\Gamma = \frac{\nu_t}{Sc} \tag{4.25}$$

where Sc is the *Schmidt number*, whose variation is significantly smaller than that of the eddy viscosity and diffusivity themselves, and is assumed equal to unity in many models (Rodi, 1984).

Algebraic models are the simplest turbulence models, and assign either a constant value to the eddy viscosity, or a value through the evaluation of an algebraic expression of the properties of the mean flow. This procedure assumes implicitly that turbulent energy is dissipated where it is created, so that turbulence cannot be transported (Rodi, 1984). As a result, this type of model is unsuitable for flows where transportation of turbulence is important.

The historically first proper turbulence model is Prandtl's *mixing-length model*. It assumes that the eddy viscosity is proportional to the local mean-velocity gradient and a parameter called the mixing length, ℓ_m, as an analogy to the mean free path on molecular level of gases. Prandtl's assumption may be expressed as:

$$\nu_t = \ell_m^2 \left| \frac{\partial U}{\partial y} \right| \tag{4.26}$$

The mixing-length can be linked to the width of the free shear layers, but different proportionality coefficients occur for different flows (Rodi, 1984).

One equation models are more advanced forms of turbulence models. To improve the ability to predict properties of turbulent flows, it is possible to relate the eddy viscosity to the kinetic energy of the turbulent fluctuations, k. A proper modeling of k, however, requires an additional partial differential equation. This allows the model to take into account the transport of turbulence, but the length scale of the vortices is still unsolved, and as it varies strongly from one flow to another, must be assigned in advance. One of the most well-known one equation models is the *Spalart-Allmaras model*.

Two equation models add two partial differential equations to the mass, momentum and energy equations. The historically first two equation model is the k-ω model, where k is the turbulent kinetic energy and ω is the specific dissipation, which determines the scale of the turbulence. These models have shown great success for a wide variety of flows, but have come somewhat in the shadow of the more popular k-ϵ model.

The most well-known is the k-ϵ model. Similarly tot he k-ω models, k determines the energy of the turbulence, but the determinant for the scale is ϵ, the turbulent dissipation. Compared to the zero and one equation models, the two equation models are the simplest *complete* models, that can be used to predict properties of a given turbulent flow with no a priori knowledge of the turbulent structure. This is achieved because the models can predict both the turbulent kinetic energy, but also the turbulent length scale. (Wilcox, 1995)

The full standard k-ϵ model is represented below (Wilcox, 1995):

$$\mu_t = \rho C_\mu \frac{k^2}{\epsilon} \tag{4.27a}$$

$$\rho \frac{\partial k}{\partial t} + \rho U_j \frac{\partial k}{\partial x_j} = \tau_{ij} \frac{\partial U_i}{\partial x_j} - \rho \epsilon + \frac{\partial}{\partial x_j} \left[\left(\mu + \frac{\mu_t}{\sigma_k} \right) \frac{\partial k}{\partial x_j} \right] \tag{4.27b}$$

$$\rho \frac{\partial \epsilon}{\partial t} + \rho U_j \frac{\partial \epsilon}{\partial x_j} = C_{\epsilon 1} \frac{\epsilon}{k} \tau_{ij} \frac{\partial U_i}{\partial x_j} - C_{\epsilon 2} \rho \frac{\epsilon^2}{k} + \frac{\partial}{\partial x_j} \left[\left(\mu + \frac{\mu_t}{\sigma_\epsilon} \right) \frac{\partial \epsilon}{\partial x_j} \right] \tag{4.27c}$$

$$C_{\epsilon 1} = 1.44, \quad C_{\epsilon 2} = 1.92. \quad C_\mu = 0.09. \quad \sigma_k = 1.0, \quad \sigma_\epsilon = 1.3 \tag{4.27d}$$

25

$$\omega = \frac{\epsilon}{C_\mu k}, \quad \ell = C_\mu \frac{k^{\frac{2}{3}}}{\epsilon} \qquad (4.27e)$$

Other two equation models exist, but these two are by far the most used.

Reynolds stress models (RSM) are the most complex of the classical turbulence models. When modeling flows with significant body forces or complicated strain fields, the two equation models encounter problems (Versteeg and Malalasekera, 2007). The models predict the directional effects of the Reynolds stress field replicated. In these cases, a Reynolds stress model, also called *second-order closure model*, may be used to achieve better results. RSM model the exact Reynolds stress transport equation, and add six partial differential equations to the set, in addition to the equation for the dissipation rate ϵ. Of course, this adds a huge computational load to the model.

Algebraic stress models (ASM) are an economic way of accounting for the anisotropy of Reynolds stresses. The reason for the high computational cost of the RSM is that the gradient of the stresses appear in the convective and diffusive terms for the same quantities. For some cases, neglecting the convective and diffusive terms altogether may give good results, but a more general approach assumes the sum of the convective and diffusive terms to be proportional to the sum of the convective and diffusive terms of turbulent kinetic energy (Versteeg and Malalasekera, 2007). Both of these approaches reduce the partial differential equations to simple algebraic equations. With some further assumptions about the different terms, this AMS may be written (Versteeg and Malalasekera, 2007):

$$R_{ij} = \overline{u_i' u_j'} = \frac{2}{3} k \delta_{ij} + \left(\frac{C_D}{C_1 - 1 + \frac{P}{\varepsilon}} \right) \left(P_{ij} - \frac{2}{3} P \delta_{ij} \right) \frac{k}{\varepsilon} \qquad (4.28)$$

where C_D and C_1 are constants.

The equations are solved along with the standard k-ϵ model.

Direct numerical simulations (DNS) aim to solve the instantaneous Navier-Stokes equations. As explained, this requires an immense computational effort, because of the need to simulate the fluctuations at a wide range of scales in time and space. However, with relatively simple geometries and moderate Reynolds numbers, DNS acts as a valuable tool for the study of the fundamental properties of turbulence. Previously simulated cases with DNS give a possibility to validate other approximate models. (Wesseling, 2000)

Large eddy simulations (LES) resolve the large turbulent eddies numerically, but reduce the modeling of the smaller eddies to a heuristic model. The development of this type of models is still progressing, but had yet to take the step out of research (Wesseling, 2000).

4.4 Solution Method

For a computer program to solve the governing equations for a given geometry, they need to be in a form that the program can understand. They will need to be defined for a finite set of discrete points, and similarly, the geometry must be divided into a set of smaller elements, onto which the equations can be evaluated. The computer program can then use a *solver* to let the solution progress. This section describes the processes of grid generation and discretization.

4.4.1 Grid Generation

For the program to take into account of the geometry, the domain has to be divided into computer-manageable parts. In the *control volume method*, which is by far the most used method in fluid dynamics, the domain is divided into discrete, non-overlapping control volumes without voids in-between. These control volumes are called *cells*, and the full network of cells is called a *grid* or a *mesh*. The program is to solve the governing equations for each of the cells. The process of fitting the grid to the geometry is called *grid generation*. Before describing the methods of grid generation, the different types of grids are introduced.

Grid types

One of the most important distinctions between different grid types, is that of structured and unstructured grids. In a *structured grid*, each grid point is uniquely identified by its indexes i, j, k. By far, most 2D structured grids have quadrilateral cells, and cells in 3D structured grids are hexahedral, although triangular and tetrahedral cells are also possible. In an *unstructured grid*, the cells have no particular ordering, so neighboring cells have to be identified through a separate table. The cells in an unstructured grid may have any shape, and a mix of shapes in a single grid is possible, although quadrilateral and triangular are most used in 2D, hexahedral and tetrahedral in 3D. The main advantage of structured grids is the easy identification of neighbor cells, which allows for quick evaluation of gradients, fluxes and boundary conditions. In addition, implicit schemes are quicker to solve because of the simple Jacobian. However, the structured configuration limits the ability for the grid to adapt to complex geometries. One other possibility is to divide the domain into a number of topologically simpler parts, and generate a structured grid for each of these parts, or blocks. This method is called the *multiblock* approach Blazek (2001). It is also possible to *outblock* regions of the structured grid. This simplifies the process of fitting the grid to a complex geometry.

When it is preferable that an internal part of the geometry is more detailed than the rest of the domain, a *nested grid* may be used. This grid is an individual block with a finer grid, that overlaps the main grid block. This allows for detailed calculations of e.g. water quality parameters for a region of interest. Olsen (2011a)

A quadrilateral or hexahedral grid does not have to be *orthogonal*, as the

ability to fit a general geometry is greatly reduced by this. Most structured grids are *curvilinear* to fit the domain boundary better. To allow this, the governing equations must be cast along the curvilinear coordinates.

Adaptive grids allow for the grid to move during the calculations. When the physical boundaries are changing, this is essential Olsen (2011a). In addition, it is useful for reduction of memory and processor use, and to increase the accuracy of the solution close to the interesting boundaries. It may also be desirable to have a higher grid density in the regions of the grid where there are high gradients, and an adaptive grid may change accordingly Olsen (2011a).

Grid generation To generate a grid to fit a physical geometry, it is essential to have detailed information about the geometry that is to be modeled. Usually, the boundary vertices are generated first, and then the internal grid cells.

The two most used methods for generation of internal grid cells are transfinite and elliptic grid generation. In *transfinite grid generation*, the lines of two opposing edges are connected with straight lines, and the cells in the other directions are distributed evenly. Other than for trivial cases with a quadrilateral or hexagonal physical domain, it is not possible to generate a transfinite grid in more than one direction. For more complex geometries, the method may not be applicable at all. The simplest form of *elliptic grid generation* solves Laplace's equation for the vertex distances, i.e.

$$\nabla^2 \xi_i = 0 \tag{4.29}$$

This method results in a smoother grid than the transfinite generation.

4.4.2 Spatial Discretization

The purpose of the discretization process is to transform the partial differential equations into an equation where the variables are functions of the variables at discrete points, i.e. the variables in one cell is a function of the variables in the neighbor cells. There are several different discretization methodologies, of which the three most commonly used are described below.

Finite difference method

The method of finite differences is directly applied to the differential form of the governing equations. *Taylor series expansions* are employed to estimate the derivatives of the flow parameters. For example, in a 1-D simulation, the velocity at position $(x + \Delta x)$ can be developed as

$$U(x + \Delta x) = U(x) + \Delta x \frac{\partial U(x)}{\partial x} + \frac{(\Delta x)^2}{2} \frac{\partial^2 U(x)}{\partial x^2} + \cdots + \frac{(\Delta x)^n}{n!} \frac{\partial^n U(x)}{\partial x^n} \tag{4.30}$$

which, truncated to the first to terms, can yield an expression for the first-order derivative:

$$\frac{\partial U\left(x\right)}{\partial x} = \frac{U\left(x + \Delta x\right) - U\left(x\right)}{\Delta x} \qquad (4.31)$$

The approximation in equation 4.31 is of first order, since the truncation error from neglecting the terms goes to zero with the first power of Δx. By linear operations of the Taylor series expansions of different points around x, higher-order derivatives may be achieved easily.

A disadvantage of the method is that it requires a structured grid, and its application to curvilinear grids is also not straight-forward (Blazek, 2001). This restricts the use of the finite difference method to quite simple grids.

Finite volume method

The method of finite volumes applies directly to the integral form of the governing equations. The *surface integral* in the formulations is then approximated as the sum of the fluxes crossing the individual faces of a control volume. The control volume may either be defined as identical to the cells, i.e. the flow quantities are stored at the cell centroid; or the flow quantities may be stored at the grid points, with varying definitions of the control volume around it (Blazek, 2001).

A great advantage of the finite volume method is that the spatial discretizations are done in the *physical space*, so there is no need to transform between different coordinate systems. This also makes it flexible to be employed in both structured and unstructured grids. As the integral form of the equations are used, the numerical scheme conserves the conservative quantities of the flow.

The great flexibility and ease of the method makes it the most commonly used methodology.

Finite element method

The method of finite elements was originally employed for structural analysis only, and its wide introduction to fluid dynamics happened first in the 1990s (Blazek, 2001). The method divides the physical space into triangular or tetrahedral elements, requiring an unstructured grid. The method has a very rigorous mathematical foundation, and the numerical effort is much higher than for the finite volume method. However, the method is ideal for treatment of non-Newtonian fluids, has some advantages in complex geometries (Blazek, 2001).

Discretization schemes

Within each of the main discretization methods described above, there are various numerical schemes for performing the spatial discretization. The following text is an introduction to the main numerical schemes, explained by the finite volume method for a structured grid, although most principles are transferable to the other methodologies.

The convective fluxes are modeled as $F_c = UA\phi$, and the diffusive fluxes as $F_d = \Gamma A \frac{d\Phi}{dx}$, where Γ_x is a dissipation coefficient, e.g. the turbulent diffusion

coefficient for scalar quantities. Because of the physical nature of the diffusive fluxes, they are always modeled with central differences, which is trivial in structured grids. The convective flux however, is dependent on the variables on the cell faces, which are not directly available, leading to a variety of different numerical schemes to approximate them.

As the purpose of the discretization is to formulate the equations so that the variables in one cell is a function of the variables in the neighbor cells, we define the notation that the central cell is cell P, and the neighbor cells are named according to the cardinal directions, as shown in figure 4.1. In 3D, there are two additional directions *top* and *bottom*.
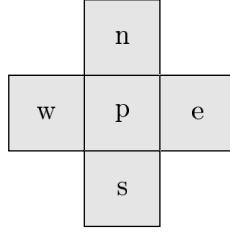
Figure 4.1: Calculation molecule for central scheme

The discretized equations may be explained as a weighted average of the variables in the cells plus a source term, i.e:

$$\phi_p = \frac{a_w \phi_w + a_n \phi_n + a_e \phi_e + a_s \phi_s}{a_p} + S = \frac{1}{a_p} \sum_{nb} a_{nb} \phi_{nb} + S_\phi \qquad (4.32)$$

where the index nb indicate the neighbor cells and S_ϕ is the source term for time-dependent calculations.

Central schemes (CS)

The central schemes are a class of schemes that average the conservative variables to the left and right for the evaluation of the flux at the face.

Assuming velocity directions from north-east, the fluxes through each of the cell faces are:

$$F_w = \frac{1}{2} U_w A_w (\phi_w + \phi_p) + \Gamma_w \frac{A_w}{\Delta x} (\phi_w - \phi_p) \qquad (4.33a)$$

$$F_n = \frac{1}{2} U_n A_n (\phi_n + \phi_p) + \Gamma_n \frac{A_n}{\Delta x} (\phi_n - \phi_p) \qquad (4.33b)$$

$$F_e = \frac{1}{2} U_e A_e (\phi_p + \phi_e) + \Gamma_e \frac{A_e}{\Delta x} (\phi_p - \phi_e) \qquad (4.33c)$$

$$F_s = \frac{1}{2} U_s A_s (\phi_p + \phi_{es}) + \Gamma_s \frac{A_s}{\Delta x} (\phi_p - \phi_s) \qquad (4.33d)$$

Applying the continuity equation (assuming no source terms), i.e $F_w + F_n = F_e + F_s$, and grouping each variable:

$$
\begin{aligned}
a_w &= \tfrac{1}{2} U_w A_w + \Gamma_w \frac{A_w}{\Delta x} \\
a_n &= \tfrac{1}{2} U_n A_n + \Gamma_n \frac{A_n}{\Delta y} \\
a_e &= -\tfrac{1}{2} U_e A_e + \Gamma_e \frac{A_e}{\Delta x} \\
a_s &= -\tfrac{1}{2} U_s A_s + \Gamma_s \frac{A_s}{\Delta y} \\
a_p &= \Gamma_w \frac{A_w}{\Delta x} + \Gamma_n \frac{A_n}{\Delta y} + \Gamma_e \frac{A_e}{\Delta x} + \Gamma_s \frac{A_s}{\Delta y}
\end{aligned}
\tag{4.34}
$$

Because of the similar formulation to the discretization of the diffusive fluxes, the solution gets unstable for low diffusion values, which requires addition of so-called *artificial diffusion* for stability. From these coefficients and equation 4.32, we see that low diffusion gives high weighting of the neighbor cells, with negative sign for the east and south direction. Another disadvantage of central schemes is their limited capability to capture discontinuities (Blazek, 2001).

Upwind schemes

In the upwind schemes, the convective fluxes are assumed to be a function of the values upstream.

The first-order upwind scheme (FOU) calculates the flux through the west face as:

$$
F_w = U_w A_w \phi_w + \Gamma_w \frac{A_w}{\Delta x} \left(\phi_w - \phi_p \right)
\tag{4.35}
$$

and similarly for the other faces. The weighting coefficients are:

$$
\begin{aligned}
a_w &= U_w A_w + \Gamma_w \frac{A_w}{\Delta x} \\
a_n &= U_n A_n + \Gamma_n \frac{A_n}{\Delta y} \\
a_e &= \Gamma_e \frac{A_e}{\Delta x} \\
a_s &= \Gamma_s \frac{A_s}{\Delta y} \\
a_p &= \Gamma_w \frac{A_w}{\Delta x} + \Gamma_n \frac{A_n}{\Delta y} + U_e A_e + \Gamma_e \frac{A_e}{\Delta x} + U_s A_s + \Gamma_s \frac{A_s}{\Delta y}
\end{aligned}
\tag{4.36}
$$

In areas with strong gradients, the truncation error in the approximation of the variables ϕ on the cell faces may lead to large inaccuracies. Because of the inabilities of the method to capture the steep gradients, it will give a smeared result compared to the analytical solution. The results may look as if there was a stronger diffusion, which gives the problem the name *false diffusion* or *numerical diffusion*. The problem can be reduced by:

- using a finer grid

- aligning the grid with the flow

- using a higher-order scheme

The second-order upwind scheme (SOU) calculates the flux through the west face for a uniform grid as:

$$F_w = \frac{3}{2}U_w A_w \phi_w - \frac{1}{2}U_w A_w \phi_{ww} + \Gamma_w \frac{A_w}{\Delta x}\left(\phi_w - \phi_p\right) \qquad (4.37)$$

and similarly for the other faces. In other words, a larger *calculation molecule* is needed, as shown in figure 4.2.
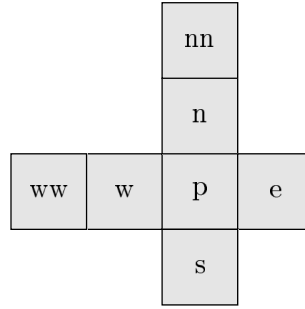
Figure 4.2: Calculation molecule for second-order upwind scheme

The weighting coefficients are:

$$
\begin{aligned}
a_w &= \tfrac{3}{2}U_w A_w + \Gamma_w \tfrac{A_w}{\Delta x} + \tfrac{1}{2}U_e A_e \\
a_n &= \tfrac{3}{2}U_n A_n + \Gamma_n \tfrac{A_n}{\Delta y} + \tfrac{1}{2}U_s A_s \\
a_e &= \Gamma_e \tfrac{A_e}{\Delta x} \\
a_s &= \Gamma_s \tfrac{A_s}{\Delta y} \\
a_{ww} &= -\tfrac{1}{2}U_w A_w \\
a_{nn} &= -\tfrac{1}{2}U_n A_n \\
a_p &= \tfrac{3}{2}U_w A_w + \Gamma_w \tfrac{A_w}{\Delta x} + \tfrac{3}{2}U_n A_n + \Gamma_n \tfrac{A_n}{\Delta y} + \tfrac{1}{2}U_e A_e + \tfrac{1}{2}U_s A_s \\
&\quad + \Gamma_e \tfrac{A_e}{\Delta x} + \Gamma_s \tfrac{A_s}{\Delta y} - \tfrac{1}{2}U_w A_w - \tfrac{1}{2}U_n A_n
\end{aligned}
\qquad (4.38)
$$

The second-order upwind scheme is second-order accurate, which means that it handles steep gradients better than lower-order schemes. However, because of the negative weighting factor for the *ww* and *nn* cells, it may give unphysical interpolations in some cases. A third-order accurate scheme has even lower dissipation errors, but the *dispersive errors* from the negative weighting might give oscillating solutions. Higher-order schemes also require more computational power.

The power-law scheme (POW) is a slight variation of the central scheme. The problem with the latter appeared at low diffusive fluxes, where the weighting factors for some cells turned out negative. An alternative is to reduce the diffusive term when the convective fluxes are dominating. In the power-law scheme, the diffusive term is scaled with the following reduction factor: (Olsen, 2011a)

$$f = (1 - 0.1\,|Pe|)^5 \qquad\qquad (4.39)$$

where *Pe* is the *Peclet* number, which is the ratio of convective to diffusive forces.

4.4.3   Temporal discretization

For most purposes, it is convenient to discretize time separately from the spatial discretization. This allows for *time-marching* methods, as the solution is only dependent on the situation in previous time steps. This can be done in two principally different ways, because we have the option of evaluating the spatial derivatives at time step *n* or *n+1*.

Explicit schemes   start from a known solution at time step *n* and employ a residual to obtain a new solution at time step *n+1*. The new solution depends on known values only, which makes it simple to implement. The most used explicit schemes use a modified *Runge-Kutta* method to arrive at a solution through iterations. These schemes advance the solution in a number of steps, by updating the solution to get a more accurate result.

   The main disadvantage of all explicit schemes is that there are strong restrictions on the time step for the methods to be stable. The *Courant-Friedrich-Lewy condition* states that the time step should be equal to or smaller than the time required to transport information across one unit in the discretization scheme, i.e.

$$\Delta t \sum_{i=1}^{n} \frac{U_i}{\Delta x_i} \leq C \qquad\qquad (4.40)$$

where *n* is the number of dimensions, and *C* is a dimensionless constant dependent on the equation to be solved. (Blazek, 2001)

Implicit schemes   evaluate the spatial differentials on the time step *n+1*, i.e. using unknown values. This results in a set of non-linear equations for the unknowns. This set can be linearized about the current time step, and solved with linear algebra. Implicit solutions do not suffer the same restrictions on the time step as explicit solutions, but the implementation is more cumbersome. There are also semi-implicit methods, interpreted as a weighting of the spatial derivatives in the current and previous time step.

4.4.4   Boundary and Initial Conditions

As any simulation models only a part of the physical domain, there will be *artificial boundaries* in the model. In addition, we have *Natural boundaries* such as walls and the fluid surface. At all these boundaries, we have to prescribe values of some of the variables.

The most used method for handling boundary conditions is to add one or more layers of *dummy cells* around the computational domain. The purpose of this is to simplify the calculation of the processes along the boundaries, as it allows for using the same discretization scheme at the boundaries as inside the domain, which makes code implementation much simpler, and solutions faster (Blazek, 2001).

Initial conditions
The main principle of time-marching methods is that the solution starts from a known situation and progresses in time. In order for this progress to happen, the known situation needs to be prescribed to the program. This is known as an initial condition, where every necessary variable needs to be prescribed to all the cells in the grid.

Inlet
At the inlet boundaries, the distribution of all flow variables needs to be specified in the dummy cells. This is called the *Dirichlet* boundary condition. The velocities may be prescribed from a logarithmic profile, and there exist methods for estimating k and ϵ at the boundary. Pressure is usually prescribed as a reference pressure, as the only the pressure gradients are of interest. (Versteeg and Malalasekera, 2007)

Outlet
If the outlet is far below of any disturbances, it may be appropriate to assume a fully developed state with zero gradients (except for the pressure) in the flow direction. This is called a *zero-gradient* boundary condition. For the velocity, this means setting the normal velocity in the dummy cells to the same value as the normal velocity at the inside of the boundary. To circumvent problems with the SIMPLE method, the value should be weighted by the mass flow ratio (Versteeg and Malalasekera, 2007).

Wall
For inviscid flow, the condition is that the velocity vector is tangential to the wall, i.e.

$$\mathbf{U} \cdot \mathbf{n} = 0 \tag{4.41}$$

where $\mathbf{n}$ is the unit normal vector at the surface.

For viscid flows, the friction reduces the velocity difference between the wall and the fluid to zero. This is called a *no-slip* boundary condition. For a stationary wall:

$$\mathbf{U} = \mathbf{0} \tag{4.42}$$

All scalar quantities need special source terms at the wall, which will depend on the turbulence level (Versteeg and Malalasekera, 2007). For laminar flow, it

is assumed that the velocity varies linearly with the distance from the wall, while the relationship is assumed to be logarithmic in turbulent flows. The exact form of the source terms depends on the variable under consideration and assumptions used, and will not be discussed here.

Symmetry

Along a symmetric boundary, there is no flow and no scalar flux across the boundary. To assure this, the normal velocity is set to zero, and the value of all scalar quantities in the dummy cells are set equal to their nearest value inside the domain.

Periodicity

If a problem involves a repeating pattern, either in the streamwise or spanwise direction, the *periodic* or *cyclic* boundary condition may be applicable. We set the flux of all flow variables leaving the outlet cyclic boundary equal to the flux entering the inlet cyclic boundary (Versteeg and Malalasekera, 2007).

4.4.5 Pressure Field

A complicating factor in the Navier-Stokes equation is the lack of an independent equation for the pressure. For compressible flows, the pressure may be found from the ideal gas law, but for incompressible flow, the density is constant, so this is not possible. The pressure gradient appears in the momentum equations, but acts more as a kinematic constraint to the velocity field than as a dynamic equation (Ferziger and Peric, 2001). As only the pressure gradient, and not the absolute value of the pressure, affects the incompressible flow, this problem may be solved by constructing a pressure field that guarantees satisfaction of the continuity equation. This is done by taking the divergence of the momentum equations and substituting it into the continuity equation to make a pressure equation (Ferziger and Peric, 2001), a method called *pressure-velocity coupling.*

The SIMPLE algorithm is the most used method pressure-velocity coupling algorithm. SIMPLE is an acronym for Semi-Implicit Method for Pressure-Linked Equations. The main principle is to make an initial guess (usually from the previous time step) for the pressure field, which will not satisfy continuity, and then use the deficiency in the continuity equation to make a formula for the pressure correction.

The initial, uncorrected pressure and velocity are denoted P^* and U^*. The pressure and velocity corrections are denoted $P^{'}$ and $U^{'}$. The correction equations are thus:

$$P = P^* + P^{'} \tag{4.43}$$

$$U_k = U_k^* + U_k^{'} \tag{4.44}$$

The discretized momentum equations for the uncorrected variables are:

$$a_p U_{k,p}^* = \sum_{nb} a_{nb} U_{k,nb}^* + B_{U_k} - \left(A_k \frac{\partial P^*}{\partial \xi} \right) \qquad (4.45)$$

where B_{U_k} are other terms than the gradient terms, A_k is the cell surface area on side k, and ξ is the grid distance.

Similarly, for the corrected variables:

$$a_p U_{k,p} = \sum_{nb} a_{nb} U_{k,nb} + B_{U_k} - A_k \frac{\partial P}{\partial \xi} \qquad (4.46)$$

Subtracting equation 4.46 from equation 4.45 and substituting equation 4.43 and 4.44, we get (Olsen, 2011a):

$$a_p U_k^{'} = \sum_{nb} a_{nb} U_{k,nb}^{'} + A_k \frac{\partial P^{'}}{\partial \xi} \qquad (4.47)$$

which can be solved for $U_k^{'}$ under differing approximations. In the standard SIMPLE method,

$$U_k^{'} = \frac{A_k}{a_p - \sum\limits_{nb} a_{nb}} \frac{\partial P^{'}}{\partial \xi} \qquad (4.48)$$

To find the pressure correction, the continuity equation is used:

$$\sum_{nb} A_k U_k = \sum_{nb} A_k U_k^* + \sum_{nb} A_k U_k^{'} \qquad (4.49)$$

where $\sum\limits_{nb} A_k U_k^*$ is the continuity deficiency from the previous time step, and $\sum\limits_{nb} A_k U_k^{'}$ is substituted from equation 4.48.

When summed up for each cell face, an equation where only the pressure correction is unknown can be derived (Olsen, 2011a):

$$a_p^o P_p^{'} = \sum_{nb} a_{nb}^o P_{nb}^{'} + b \qquad (4.50)$$

where b is the continuity deficit from the previous iteration, which is zero at convergence. The weighting coefficients are:

$$a_{nb}^o = \frac{A_{nb}^2}{a_{p,nb}} \qquad (4.51)$$

The full algorithm is:

Guess a pressure field P^*
DO
    Calculate velocity field U^* from equation 4.47
    Calculate pressure correction from equation 4.50
    Correct pressure with equation 4.43
    Correct velocities with equation 4.44
UNTIL convergence

There exist several improved versions of the SIMPLE algorithm, with different under-relaxation. However, all methods will converge to the correct solution, and which algorithm is the fastest depends on the flow in question.

4.4.6 Water Surface

For enclosed piped water flow, the flow field is calculated with the above methods. When a water surface is present, however, another essential step is needed, to calculate the new position of the water surface. This involves some way of keeping track of the surface position and how it changes, and there are various ways of doing this (Apsley and Hu, 2003). Depending on if the grid is adaptive or not, two fundamentally different groups of algorithms are used to calculate the free water surface.

Fixed grid methods

A fixed grid algorithm computes a two-phase flow with water and air, and the purpose is to determine where the boundary between the two phases is. One of the most used fixed grid algorithms is the *volume of fluid* (VOF) method. This method is based on the volume fraction of water in every cell:

$$F = \frac{V_w}{V_w + V_a} \tag{4.52}$$

where V_w and V_a are volume of water and air, respectively. This ratio can be solved by the convection-diffusion equation, i.e. (Olsen, 2011a)

$$\frac{\partial F}{\partial t} + U_i \frac{\partial F}{\partial x_i} = \frac{\partial}{\partial x_i} \left(\Gamma \frac{\partial F}{\partial x_i} \right) \tag{4.53}$$

When this is calculated for every cell, the location of the free water surface can be found, although this is not always trivial.

Another much used method is the *level set* method. Instead of using the volume fraction of water, it solves for the distance to the water surface, *L*. This is then solved with the convection equation (Olsen, 2011a):

$$\frac{\partial L}{\partial t} + U_i \frac{\partial L}{\partial x_i} = 0 \tag{4.54}$$

With the level set method, the process of finding the free water surface is simpler than with VOF. Of course, both volume of fluid and level set suffer from numerical diffusion, which may lead to inaccuracy (Muzaferija and Peric, 1997).

Yet another popular method is the *marker and cell* (MAC) method. Marker particles are initially placed in the fluid cells, and the local velocity moves them. Based on the particle movements in the cells adjacent to the previous surface, the new surface is calculated (Harlow and Welch, 1965).

Adaptive grid methods

In contrast to fixed grids, adaptive grids are able to adjust so that the top cells in the grid are aligned with the free water surface. This has the advantage that all cells are used to simulate the water flow. While the fixed grid methods may show inaccuracies where cells are partially filled with water, this is not a problem with adaptive grids. However, the adaptive grid methods tend to be more unstable than their fixed grid counterparts. (Olsen, 2011a)

One popular algorithm used for adaptive grids uses the water continuity equation in the top cells to calculate the changes in the water surface (Muzaferija and Peric, 1997). Then, the pressure in these cells is calculated by linear interpolation of the cell underneath and the surface (Olsen, 2011a). Because gravity is included as a source term in this method, the solution may be unstable, and a very short time step is needed. This method is therefore not preferred for simulations of long durations.

Another method is to use the energy equation to calculate the water surface changes. This method keeps the surface at a reference location at a known elevation, and uses the computed pressure field to estimate the location of the surface in other cells (Olsen, 2011a):

$$dh = \frac{dp}{\rho g} \tag{4.55}$$

where dh is the elevation difference between the surface in the current cell and the reference cell. The method is very stable even for long time steps, but assumes that the pressure field close to the surface is hydrostatic, so it is not applicable to very steep surface slopes (Olsen, 2011a).

4.5   Sediment Simulation

Since sediment transport traditionally is divided in bed-load and suspended load, this distinction is also often used in the numerical simulation programs. This distinction is useful since the means of transport is different, and different formulas exist for the two transport types.

4.5.1   Bed-Load

When bed-load is treated as a separate fraction of the total load, it is modeled with specific bed-load formulas. One of the most used is from van Rijn (1987):

$$\frac{q_b}{d_{50}^{1,5}\sqrt{g\frac{\rho_s - \rho_w}{\rho_w}}} = 0.053\frac{\left[\frac{\tau - \tau_c}{\tau_c}\right]^{2.1}}{d_{50}^{0.3}\left[\frac{g(\rho_s - \rho_w)}{\rho_w \nu^2}\right]^{0.1}} \tag{4.56}$$

38

4.5.2 Suspended Sediment

Suspended sediment concentrations are modeled with the convection-diffusion equation, like other scalar quantities. In addition to the water convection, sediment particles have a vertical settling velocity w, which is handled in the last term on the left hand side in equation 4.57.

$$\frac{\partial c}{\partial t} + U_j \frac{\partial c}{\partial x_j} + w \frac{\partial c}{\partial x_3} = \frac{\partial}{\partial x_j}\left(\Gamma \frac{\partial c}{\partial x_j}\right) + S_c \tag{4.57}$$

The diffusion coefficient Γ is often set proportional to or equal to the turbulent viscosity, but other relationships exist.

S_c in this equation is a sediment source term, which may be used to assign a pick-up flux from the bed, using one of several erosion formulas available. Another way to model the deposition and re-suspension of sediment, it to use van Rijn's 1987 formula for the equilibrium concentration close to the bed (Olsen, 2011b).

$$c_{bed} = 0.015 \frac{d^{0.3}}{a} \frac{\left[\frac{\tau - \tau_c}{\tau_c}\right]^{1.5}}{\left[\frac{g(\rho_s - \rho_w)}{\rho_w \nu^2}\right]^{0.1}} \tag{4.58}$$

where a is a reference level set equal to the roughness height (Olsen, 2011a). By prescribing a concentration to the bed cells in this way, there will be a continuity defect, which may be used to calculate the bed changes in time-dependent calculations.

4.5.3 Bedforms

For small-scale simulations, it is possible to simulate bedforms directly by having the bed change accordingly, but for most practice purposes, the size of the cells compared to the bedform length prevents this approach. Instead, empirical formulas may be used to calculate the bedform height, Δ. The most used formula for this purpose is equation 4.59 (Van Rijn, 1984).

$$\frac{\Delta}{d} = 0.11 \left(\frac{D_{50}}{d}\right)^{0.3} \left(1 - e^{\left[\frac{\tau - \tau_c}{\tau_c}\right]}\right) \left(25 - \left[\frac{\tau - \tau_c}{\tau_c}\right]\right) \tag{4.59}$$

Together with the bed sediment grain size distribution, the calculated bedform height may be used to compute an effective hydraulic roughness (Van Rijn, 1984):

$$k_s = 3d_{90} + 1.1\Delta\left(1 - exp\left[-25\frac{\Delta}{\lambda}\right]\right) \tag{4.60}$$

where λ is the bedform length, estimated as $\lambda = 7.3d$.

4.6 Errors in CFD

Computational fluid dynamics involves approximating the governing equations with discrete representations and numerically solve them with a computer program. As a result, all results from numerical simulations are approximate. In addition, because of the high complexity of the fluid flow processes and sometimes only partly explained by the governing equations, which in some cases may give results that are not a true representation of the physical processes. Furthermore, the CFD program user introduces errors and uncertainty to the problem.

The ERCOFTAC BPG adopts the following classification of CFD error sources:

1. Model errors and uncertainties

2. Discretization or numerical errors

3. Iteration or convergence errors

4. Round-off errors

5. Application uncertainties

6. User errors

7. Code errors

4.6.1 Model Errors and Uncertainties

Model errors are discrepancies between the exact solution to the model equations and the real flow. In other words, we are solving equations that are not a true representation of the actual physical processes. Any simplification in the representation of the governing equations may introduce errors that in some cases cause considerable deviations in the results. One example is the error introduced by replacing the instantaneous Navier-Stokes equations with RANS and a turbulence model. MARNET (2000)

4.6.2 Discretization or Numerical Errors

Discretization errors occur when there is a deviation between the numerical solution on a finite number of grid points and the exact solution to the equation. A larger number of grid points and a optimally distributed grid will decrease these errors. This type of error is present in all numerical methods, and arises when a continually varying parameter is approximated with a polynomial. MARNET (2000)

4.6.3 Iteration or Convergence Errors

Convergence errors arise when the solution deviates from a fully converged solution in the grid. The reason for this is that the numerical solution algorithms normally are iterative, gradually approaching the converged solution, but the process may be stopped before convergence is met. This may be because the convergence criteria are not strict enough, because the simulation time is too low compared to what is needed, or because the numerical methods do not converge. MARNET (2000)

4.6.4 Round-Off Errors

Round-off errors occur when the difference between two values of a parameter in an iterative scheme is below the accuracy of the computer. Although regarded as an insignificant problem compared to the other error sources today, with very fine spatial or temporal resolution, it may still cause problems. MARNET (2000)

4.6.5 Application Uncertainties

Application uncertainties arise when the application is complex and the data needed to get a correct solution is not available. Examples of this are uncertainties in the model geometry, and boundary and initial condition uncertainties. MARNET (2000)

4.6.6 User Errors

User errors are defined as errors that arise due to mistakes and carelessness of the user. Although this error source is reduced with increasing experience, there is always a possibility of human errors. MARNET (2000)

4.6.7 Code Errors

Code errors are caused by bugs in the computer program, and may arise from unintended programming errors in the model implementation or errors in the compilers used to generate the program. Code errors are difficult to find because of the high complexity and the often insignificant appearance of the error in the code. MARNET (2000)

5 SSIIM

5.1 Introduction

SSIIM is an abbreviation for Sediment Simulation In Intakes with Multiblock option. The program has been under development by professor Nils Reidar Bøe Olsen at the Norwegian University of Science and Technology since 1990. It is made for teaching and research purposes, and is not yet recommended for commercial use. The program was initially intended for simulation of sediment movements in general river geometries, as a physical model study is unlikely to yield accurate results for these cases, especially for fine sediments . The purpose of the program has later been extended to include other hydraulic engineering topics, e.g. head loss in tunnels, spillway modeling, stage-discharge relationships, turbidity currents, water quality simulations and habitat studies in rivers. The program and its user manual can be downloaded for free from http://folk.ntnu.no/nilsol/ssiim. (Olsen, 2011b)

Compared to other CFD programs, SSIIM has the advantage of being able to model sediment transport with moveable bed for complex geometries. This allows for modeling of several sediment sizes, bedload and suspended load, bedforms and effects of sloping beds. (Olsen, 2011b)

SSIIM solves the incompressible Navier-Stokes equations with the k-ϵ model on an almost general three-dimensional non-orthogonal grid, although all grid lines in the vertical direction are exactly vertical. The control volume method is used for the discretization, with choice of power-law or second order upwind scheme. This process neglects non-orthogonal diffusive terms. The SIMPLE method is used for the pressure coupling. The program uses an implicit solver to solve the velocity field, which is then used when solving the convection-diffusion equations for different sediment or water quality parameters.(Olsen, 2011b)

5.2 Versions

The program exists in two main versions: SSIIM 1 and SSIIM 2. There are versions for different platforms, i.e. Windows, OS/2 and Unix, and the Windows version exists both with and without the graphical user interface, as well as 32 and 64 bit versions. The main difference between the two main versions is that SSIIM 1 uses a structured grid, while SSIIM 2 uses an unstructured grid. The unstructured grid has the advantage of each cell being easily identified by the the indexes in i, j and k direction. This allows for simple editing of outblocking, wall locations and inflow and outflow surfaces, which may be assigned in the data sets. This is not possible with an unstructured grid, as each cell has only one index, making it difficult to manually locate. Inflow and outflow areas then have to be specified in the graphical discharge editor, which only exists for the unstructured grid versions. The grid editor for SSIIM 2 also allows for generating and connecting multiple grid blocks, making it possible to generate more advanced grids that fit complex geometries. The unstructured grid versions also allows for adaptive grids, which may change when the water

surface rises or falls, or when bed geometry is changed. When the water surface falls below the bed in a cell, A wetting and drying algorithm lets the program treat the cell as inert until the water again rises. These methods allow for a complex grid that can change over time to adapt to the altering boundaries. SSIIM 2 also has some additional sediment and water quality algorithms that are not implemented in SSIIM 1. Because of the easy connections between cells, surfaces and geometry points in a structured grid, the solvers for these grids are faster, and occupy less memory during the computations. For computations where an unstructured grid is not necessary, and there is no wetting and drying, a result would be achieved faster with SSIIM 1. (Olsen, 2011b)

The work with this thesis has used SSIIM 2 exclusively, so most of this text refers to SSIIM 2 as simply *SSIIM*. When contrasts to SSIIM 1 are made, this is shown explicitly.

5.3 Grid Editor

SSIIM includes a grid editor to fit a grid to the geometry. The constraint that all grid lines in the vertical direction need to be perfectly vertical, simplifies the grid generation, as all grid point manipulation may be done in the map view.

The grid is based on one or several grid blocks. These start out quadrilateral, but may be transformed in the grid generation process. However, the computational domain of each block is still rectangular, in that for each stream line, there is the same number of cells in the lateral direction. Up to 19 blocks may be glued together to create a complex geometry (Olsen, 2011b). However, the manual suggests that with the newest *wetting and drying* algorithm, it may be easiest to use a single block for the whole geometry. This process is explained further below.

The boundary of the block is originally defined by the four corner points, but additional no-move points may be defined and positioned before the boundary is generated in order to have a non-rectangular block. To generate the internal 2D grid, the user has the options of a transfinite grid in the x or y direction, or an elliptic grid. For the elliptic grid generator, the user can define *attraction points* or lines and their attraction or repulsion force.

In the beginning, the vertical elevation of the bed is defined only by the elevation of the border cells. To change this, geodata points may be added inside the grid. When the geodata points are set, the user may invoke the bed level algorithm, which interpolates z values for the bed surface of the grid from the nearest geodata points in the *geodata* file. The output is logged in the file *boogie.bed*.

To set the water surface, the user may add surface points. When three points are added, they define a plane covering the area between them.

To complete the grid generation, the 3D grid must be generated. This distributes cells in the vertical direction between the bed and the water surface. Since the grid is unstructured, the number of grid cells in each vertical may vary. The grid may then be saved to the *unstruc* file.

When simulating a natural water body, the geometry is most likely too complicated to build by setting border and bed points manually. It is then necessary to start with a *geodata* file. This file contains xyz coordinates of bed points, either as contour lines from a map, or from measurements, e.g. from echo sounding.

When using the wetting and drying algorithm to generate the grid, it is often best to start with a single rectangular block covering the whole geometry. The water level is set at a so high level that it is above the bed at all places. In areas where there are too few geodata points, additional points may be added manually. The *unstruc* file is then written for the wetted geometry, and this file will be used for all future computations. If a simulation is to be started at a lower water level, a *koordina.t* file is generated with the initial water level, edited in a spreadsheet to the wanted water level, and saved as *koordina*. When the *F 112 1* data set is used in the *control* file, the program loads the original *unstruc* file, then the *koordina* file with the water level is read, and the grid is regenerated to the lowered water level. The original *unstruc* file is not to be overwritten. If it is overwritten with the lower water level, the dry areas will be removed from the grid, causing problems when the water level rises again. (Olsen, 2011b)

5.4   Input and Output Files

A range of input and output files can be read and written by SSIIM, but most of them are for special purposes only and not needed otherwise In SSIIM 1, the main input files are *control* and *coordina*. The *koordina* file contains the geometry, while the *control* file contains many of the other parameters. The files need to be present when the program starts; otherwise the program generates default files based on some simple user input. In SSIIM 2, the grid and water discharges are stored in the *unstruc* file. The *control* file is also used for SSIIM 2, but default will be used if it is not present when the program starts. (Olsen, 2011b)

Boogie File

The *boogie* file shows a print-out of intermediate results from the computations, as well as average velocity, shear stress and water depth during the initialization, and the trap efficiency and sediment grain size distribution. In addition the file lists explanations if an error occurs. It is possible to write more detailed information to the file by including the option *D* on the *F 1* data set in the *control* file.

Control File

F data set:

- F1: Debugging option. Reads a character. If it is D, the print-out to the *boogie* file will be more detailed. If it is C, the coefficients in the discretized equations are written to *boogie*.

- F2: Automatic execution. Defines which parts of the program will start automatically after the initialization. The modules are started in the order they appear. R: Read *result* file. I: Initiate sediment concentration computation. S: Calculate sediment concentration. W: Start water flow computation. U: Read *unstruc* file. M: Write *result* file. H: Write *unstruc* file. Y: Regenerate grid.

- F 16: Roughness coefficient used on side walls and bed.

- F 33: Transient flow parameters: time step, number of inner iterations

- F 36: Free water surface algorithm. Different choices for the algorithm to calculate the change in the water surface

- F 37: Transient sediment computation.

- F 48: Parameter for print-out of special files at a given interval. If the number is 0, the *result* file is written. If it is higher than 0, the program will interpolate the values to the profile given in the *interpol* file and write a file with the values in these verticals. If the number is 2, the velocities, pressure, k and ε values are written to the *interres* file. If it is 16, the concentrations of the different sediment fractions are written.

- F 64: Algorithm for grid generation

- F 65: Assigned number of cells, surfaces, corners, surfaces in block connections, and connection points

- F 81: Number of time steps in *timei*

- F 91: Wetting and drying parameters. The first number read is the minimum height of a cell for it to be generated. The second number is the minimum height for it to be modeled as 3D.

- F 102: Enabling of wetting and drying

- F 105: Number of iterations between updates of water surface

- F 106: Thickness of upper active sediment layer

- F 112: Invoking the process described to start simulation at a lower water level than in *unstruc*

- F 113: Stabilizing of shallow regions close to side walls

- F 159: Stabilization algorithms.

- F 168: Multi-grid solver for the pressure-correction equation

- F 200: Residual norms for k and ε

- F 206: Maximum number of processors used for parallel versions

- F 235: Stabilization of triangular cells

- F 237: Overriding discharge values in *unstruc*

- F 291: Stabilization of edge cells

- F 292: Time step per inner iteration in Navier-Stokes equations

- F 293: Write residuals file

G data set:

- G 1: Number of cells in x, y and z direction, and number of sediment sizes

- G 6: Calculation of free water surface with adaptive grid. Reference to cell that will have the same water level, and relaxation factor and convergence criteria for the calculation

P data set:

- P 10: Number of iterations between each time the program writes the file in the *F 48* data set

W data set:

- W 1: Manning-Strickler value, discharge and water level

K data set:

- K 1: Number of outer iterations for flow procedure and minimum number of iterations between surface updates

- K 3: Relaxation factors for velocities, pressure correction, and k and ϵ equation

- K 5: Block-correction for the six water flow equations. If the value is 10, the multi-grid algorithm will be invoked

S data set: Sediment group number, size and fall velocity
  N data set: Bed sediment distribution
  B data set: Distribution of bed sediments

Unstruc File

The *unstruc* file stores the geometry data. It contains all grid line intersections and cell and surface connections, as well as information about inflow and outflow of water and water quality parameters.

Geodata File

The *geodata* file contains geometrical data in the form of xyz coordinates. The purpose of the file is to use geometrical data from field measurements or digital maps as input for the grid editor.

Bedrough File

The *bedrough* file allows for assigning a roughness height to individual cells, overruling the value calculated from the Manning-Strickler value in *W 1* and the *F 16* data set.

Result File

The *result* file contains the results from the water flow calculations. SSIIM writes the file when the solution has converged, or when the prescribed number of iterations have been calculated. The file can also be written periodically. The data stored in the file is the velocities in three directions, k, ϵ and pressure, and then the fluxes on all the cell walls. The program then uses this file for the solution of the convection-diffusion equations for the sediments and water quality parameters. It is also possible for the program to read the file after initialization to start the water flow calculations from the state in the stored file.

Interpol File

In the *interpol* file, the user can give the xy coordinates of vertical profiles where the results are wanted. By using the *F 48* data set in the *control* file as described above, the program will interpolate the chosen parameter to the cells in the verticals in the *interpol* file and write a file with the results at the interval specified in the *P 10* data set.

Timei File

The *timei* file is an input file for time series of water level, discharges, sediment concentrations, and control for output to the *timeo* file. Only the input is described here. Under default settings, the program reads five float for each line starting with *I*. The first is the time when the data is to be used. The program uses linear interpolation between two given times. The following floats are the upstream and downstream discharge and water level. The water levels are in the cells defined in the *G 6* data set. If the values are set to a negative number, the program will calculate the value. If the transient sediment computation method is used, SSIIM also reads the concentration of every sediment fraction for each inflow group. It is also possible to vary the discharge of each discharge group individually over time with a *D* data set. The sum of the inflow discharges always need to equal the sum of the outflows.

5.5 Graphics

SSIIM includes a module to display the grid or the calculated variables. In SSIIM 1, it is possible to show the graphics in longitudinal or cross-sectional profiles as well as the map view, but because of the unstructured grid, SSIIM 2 only displays the variables in map view at any level. It is however not possible in any version to view a profile in an arbitrary direction from within the program. (Olsen, 2011b).

When displaying the graphics, the user may choose which variables to show. The list of variables to display is long, including horizontal and vertical velocities, pressure, Froude and Reynolds number and water quality parameters. The menu has a separate option for sediment variables, with choices of e.g. sediment concentration, bed levels and bed changes. The concentration may be displayed for each of the sediment fractions, for the sum, or for different sieve fractions of the sizes.

The values are shown as colored or black *isobar* lines, and the user may toggle an adjustable legend. Velocities may in contrast be displayed as velocity vectors to get a better overview of the directions of the flow. For more colorful graphics, or for profiles in arbitrary directions or curved profiles, the data will need to be post-processed and viewed in another designated program. The graphics may be displayed after the simulation has finished, or during the calculations. SSIIM allows for periodical writing of the results files, in order to give time dependent graphics.

It is also possible to predefine a profile by giving xy coordinates in the *interpol* file. The program can then interpolate the chosen variables to the vertical lines at the given coordinates and write a *.vtk* file at a specified iteration interval, which may be viewed in a designated program.

5.6 Limitations

Any computer program has some limitations that may be solved more correctly with another program. For SSIIM, we can list a few:

Non-Orthogonal Diffusive Terms
Like many CFD-programs, SSIIM ignores non-orthogonal diffusive terms. Grid cells with angles deviating strongly from 90 degrees might therefore give erroneous diffusion.

Vertical Lines
All the vertical grid lines have to be exactly vertical. This prevents a perfect alignment of the grid with the flow field, which may cause false diffusion. In addition, close to steep but non-vertical side walls, there might be problems with triangular cells.

Time-Dependent Simulations
Time-dependent simulations are only quasi-time-dependent, as the inflow and outflow have to be the same. Although this restriction is removed by the *F 287* data set, which calculates the outflow from the water continuity based on the inflow and the prescribed water levels, the situation is still treated as a steady-state, so the seiches usually accompaying a water level change is not modelled.

Viscosity

The kinematic viscosity of the fluid is hard-coded in the program to be equivalent to water at 20 degrees Celcius.

Bugs

Any computer program is bound to have bugs, as described in section 4.6. For a non-commercial program like SSIIM, there will be many modules that are less tested than others, which may not work as expected. When evaluating the results from a simulation, it is important to keep this in mind.

Used Friendliness

Compared to commercial CFD programs, the user friendliness in SSIIM is limited. The simulation choices are mostly made by changing data set based text files, which may alienate new users.

Support

As SSIIM is non-commercial program with only one developer, there is no capacity for online support. Being based at the institute is hence a great advantage, because there are several experienced users who can give support. When a specific problem is encountered or a bug is found, direct contact with the program developer gives a unique possibility for implementation and modification of algorithms.

6 LISST-SL

6.1 Introduction

LISST-SL is an instrument for measuring concentration and particle size distribution of suspended sediment based on indirect measurements. LISST-SL (Laser In Situ Scattering and Transmissometry - StreamLine) is a product of *Sequoia Scientific*, in a series of similar instruments using the principle of laser diffraction. The instrument measures the concentration of sediments every two seconds in 32 particle size classes from 2 to 350 μm.

In contrast to the other instruments in the product series, the LISST-SL is a sensor only, without batteries and storage capacity. It is connected via a long cable to a surface-based control box, and is streamlined to minimize the disturbance on the flow field. The other LISST products have internal battery packages and storage capacity, and can operate in different conditions. The LISST-STX instrument has an added settling tube for performing submerged settling experiments. The LISST-Portable is a light battery-powered portable version of the instrument. Separate instruments are also available for constant monitoring of e.g. river concentrations.

6.2 Instrument

The system consists of three parts: The *LISST-SL sensor*, the *B-reel*, and the *top control box* (TCB). The different parts are displayed in figure 6.1. The sensor cannot function without the TCB, but the B-reel may be switched for a shorter cable for laboratory tests.

Figure 6.1: LISST-SL
(Sequoia, 2011d)

6.2.1 LISST-SL Sensor

The LISST-SL sensor is the submersible part of the system and works only as a sensor, i.e. has no data storage capacity. The sensor has no internal battery power and needs constant connection with the TCB to work. The sensor

consists of an internal pump powered tube for suction of sediment-loaded water, optics for measuring of laser scattering, a pitot meter for depth and velocity measurements, and a thermometer. The sensor is streamlined in order to always stay in the direction of the main component of the water flow. The pitot meter measures the water velocity, and the *isokinetic pump* adjusts to pump the water through the internal tube at the same speed as the ambient velocity. This is important in order to get accurate concentration and particle size distributions, as higher inflow velocities will suck more water and fine sediments in, keeping the fraction of high-inertia particles lower than the ambient concentrations.

6.2.2 B-Reel

The B-reel is a strong cable connecting the LISST-SL to the TCB. It is wrapped on a barrel on the user side, with a handle for manual operation as a winch. The cable serves both as a means of lowering and rising of the sensor, it provides power to the instrument, and it serves as information channel between the two objects.

6.2.3 Top Control Box

The TCB contains the battery package for the instrument. It has a touch-screen panel for easy control of the measurements, and real-time display of the sensor activity. The internal computer controls the touch-screen display and the scheduling and controlling programs for the measurements. The battery is rechargeable, and there is a cable for data transfer to a computer.

6.3 Laser Diffraction

The basis behind the LISST-SL is the physical principle of *laser diffraction.* Diffraction is the apparent bending of waves around small obstacles. This implies that the concentrated, straight light beam from a laser will be scattered in the meeting with particles, and the scattered light pattern can be measured. The technique used in the LISST system takes advantage of the fact that spherical particles with known properties will scatter light in a completely understood way. The exact scattering pattern of a spherical particle with known size, color and composition can be calculated with the *Airy function*, equation 6.1 (Sequoia, 2011c). For a given diffraction angle, the light scattering from particles with radius r is given as:

$$I\left(\theta\right) = r^4 \frac{J_0\left(ka\theta\right)^2}{\left(ka\theta\right)^2} \tag{6.1}$$

in which k is the wave number ($k = \frac{2\pi}{\lambda}$), and $J_0\left(x\right)$ is the *zero-order Bessel function*:

$$J_0\left(x\right) = \sum_{m=0}^{\infty} \frac{\left(-1\right)^m}{\left(m!\right)^2} \left(\frac{1}{2}x\right)^{2m} \tag{6.2}$$

51

Equation 6.2 is the $y(x)$ solution to the zero-order Bessel differential equation:

$$x^2 \frac{d^2 y}{dx^2} + x \frac{dy}{dx} + x^2 y = 0 \qquad (6.3)$$

The form of equation 6.1 is convenient, as it allows for calculation of the scattering for different particle sizes and angles. In addition, a small deviation in particle size will make a large deviation in scattering pattern, making identification of particle size a trivial process with only one particle size present. (Sequoia, 2011b)

As the laser diffraction is linear, the light scattering is proportional to the concentration of particles. This allows for superposition, and for a mix of different particle sizes, we get a total diffraction according to equation 6.4:

$$I(\theta_i) = \sum_{j=1}^{n} C_j I_j(\theta_i) \qquad (6.4)$$

Like most laser particle size analyzers, the LISST uses ring detectors, i.e. a circular detectors with a certain width placed around an origin, corresponding to certain deviation angles from the original laser beam direction. The LISST has 32 ring detectors, each measuring the scattered light in a short range of deviation angles (Sequoia, 2011b). When multiple particle sizes are present, the scattering pattern measured by the LISST is the sum of the individual scattering patterns from all the particles present. This corresponds to equation 6.4 above, with $n = 32$.

For all the relevant diffraction angles, equation 6.4 may be used to calculate the scattering, and the resulting vector is the total scattering pattern. This may be written in matrix form, according to equation 6.5.

$$E_v = \boldsymbol{K_v} C_v \qquad (6.5)$$

Put differently, the scattering pattern for a range of particles is a simple matrix multiplication between the *Kernel matrix* and the vector of concentrations of different particle sizes.

The Kernel matrix is a quadratic matrix containing the scattering for a range of particle sizes at a range of different angles, as displayed in equation 6.6.

$$K_{i,j} = I_j(\theta_i) = a_i^4 \frac{J_0(ka_j\theta_i)^2}{(ka_j\theta_i)^2} \qquad (6.6)$$

Equation 6.5 gives the scattering pattern as a vector containing the power of the scattered light for a number of angles. When the scattering vector is known, inversion of the same matrix may be used to calculate the concentration of the different particle size classes. This is, however, not always straight-forward.

Firstly, the 32 particle size ranges have to be chosen, and a representative scattering pattern calculated. This pattern may not be exactly identical to the scattering pattern measured with a random distribution of particles within this

range. This calls for some deviations from the actual particle size distribution and is responsible for some of the flattening of the curves that may be observed. However, this would normally not be a big problem if specific particle sizes are not of utmost interest.

Secondly, the inversion process with normal linear algebra may give unphysical results, e.g. negative values and unreasonably large spikes. To solve this, *inverse theory* has been used, with methods searching for non-negative values through least square algorithms etc. The very first LISST products used such an algorithm called the *Philips-Twomey algorithm* (Sequoia, 2011c). This method had the disadvantage of flattening the curve too much, and the resolution of the results was low. From 1999 and forwards, Sequoia has used a self-developed non-linear iterative algorithm, the *NLIA algorithm*, which preserves high resolution and non-negative values (Sequoia, 2011c).

Thirdly, the fundamental theory is based on spherical particles. However, almost no natural particles are spherical, and this will influence their laser diffraction and hence give erroneous results from the matrix inversion. Results from (Sequoia, 2008) show that it is possible to make a new Kernel matrix for naturally shaped particles. Their results show that irregular particles with a size < 16 µm scattered more light at larger angles than spherical particles, and this effect increases for smaller particles. The result of this is that using the Kernel matrix from the Airy function gives a concentration matrix with a higher concentration of finer particles. This problem is solved by using the Kernel matrix for naturally shaped particles. (Sequoia, 2008)

6.4   Limitations

Some limitations are mentioned in the previous section, based on the accuracy of the approach. The ring detectors used in the sensor give further limitations to the use.

The ring arrangement gives the set of diffraction angles that are measured, and hence limits the scope of detectable particle sizes. The LISST-SL has a range of detectable particle sizes from 1.9 µm to 381 µm (Sequoia, 2011e). When particles outside this scope are present, their scattering pattern will influence the measurements. For particles that are larger, the cut-off is quite sharp, so the influence will decrease rapidly as the size deviation increases. However, for small particles, this is not the case. This means that particles even 5 times smaller than the lower threshold have a significant influence on the measurements, as shown in figure 6.2. The practical consequence of this is that the inversion will yield a higher concentration of the finest particle size classes. (Sequoia, 2011a)
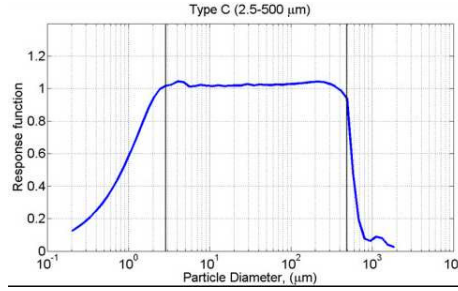
Figure 6.2: Results of particles outside range
(Sequoia, 2011a)

The concentration measurements also have some limitations. The LISST manual states that the approximate concentration limits are from about 10 to 2000 mg/L These values are guiding values, as the limits will depend highly on the size of the particles. Outside the viable region, the sensor may still work, but the accuracy will be reduced. (Sequoia, 2011e)

The instrument is calibrated for isokinetic use from 0.5 to 3.0 m/s, but is listed to operate from 0 to 3 m/s (Sequoia, 2011e). This means that at water velocities lower than 0.5 m/s, the internal pump may not suck the water into the instrument at the same speed. In river use, this will not affect the operation as the velocities are normally higher than 0.5 m/s, but in a reservoir, it might inflict some difficulties. At times, the pump gets automatically switched off during operation, making a sudden jump in the measured concentrations. This problem was already encountered in the lab, where we initially failed to get the velocities high enough.

7 Angostura

7.1 Introduction

The simulated case in this thesis is the Angostura hydropower reservoir in Costa Rica. For a better understanding of the site-specific conditions, this chapter includes some background information about the water shed in which the reservoir is situated.

7.2 Reventazón River Basin

The Reventazón river basin, which is situated in the Cartago and Limón provinces in the central Costa Rica. It is part of a larger primary river basin the Reventazón-Parismina basin, which drains out in the Caribbean Sea on the east coast. By area, it is the third largest river basin in Costa Rica, with its approximate 3,000 km^2. The length of the main river in the network is 145 km, and the mean slope is 2.1% (UDGN, 2008).
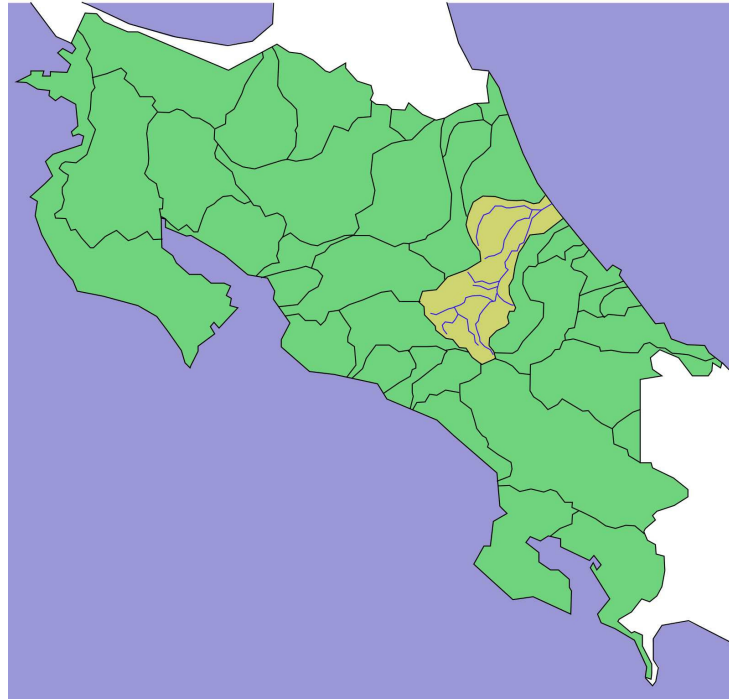

Figure 7.1: The Reventazón-Parismina river basin
Based on (UDGN, 2008)

7.2.1 Importance to Costa Rica

Over 400,000 people live within the boundaries of the watershed, and depend on the river for drinking water, irrigation, and electricity. 38% of the country's hydroelectricity is produced in the river, and it provides 25% of the drinking water used in the capital San José (Catano et al., 2009). About 40% of the area is forested, much of which is protected. In addition, a large portion of the land is agricultural areas, where the main products are coffee, sugar canes, bananas, flowers, vegetables and macadamia nuts (UDGN, 2008). The river is also used extensively for whitewater rafting, attracting many tourists. The river contains some of the most difficult rafting sections in the country, in addition to milder rapids for inexperienced rafters. While the upstream hydropower development cuts off the highest peaks in the hydrograph, it also keeps the discharge high in the drier seasons. However, the dams make up impassable barriers for the rafters, effectively dividing the reaches into shorter segments. New development downstream will further shorten the available reaches for rafting activities, but this is a trade-off for the country's focusing on renewable energy.

7.2.2 Topography

Because of its large size and its location in Costa Rica, the topographic variation within the catchment is large. The highest point is the Cerro de la Muerte in the southeast, with its altitude of 3,451 m, and about 20% of the catchment area lies above 2,000 m.a.s.l. In contrast, the lower plains stretch far into the catchment in the east, so an estimated 20% lies lower than 100 m.a.s.l, as seen in figure 7.2.
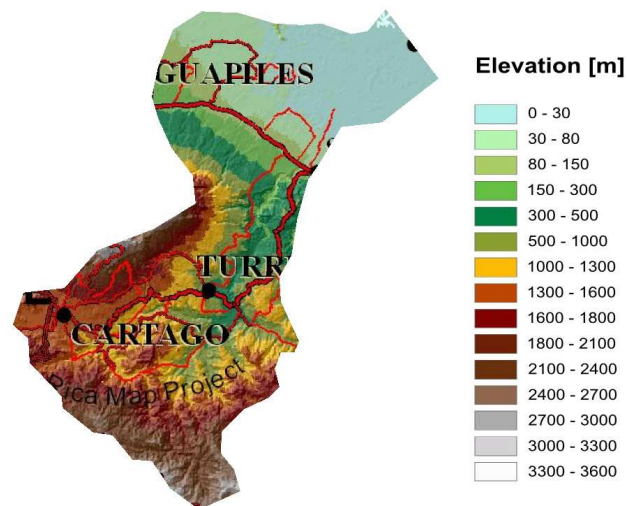
Figure 7.2: Topography
Based on CRMP (2007)

7.2.3   Climate

The annual average temperature in the catchment varies with the climatic zones. The coastal areas have a tropical climate with a mean temperature of about 25 degrees Centigrade, while the upper regions are cooler with an average of 10 degrees. as seen in figure 7.3. Being located in the tropics, the seasonal variations in the temperature are not drastic, but there is a slight change in temperature from season to season, which is more predominant in some areas.
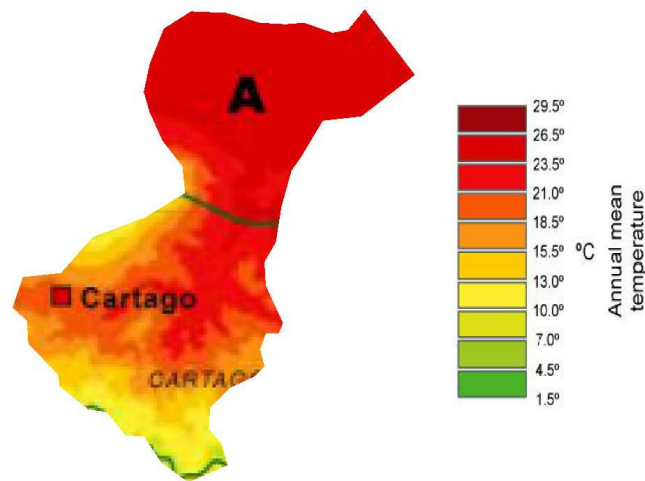
Figure 7.3: Temperature
Based on (bcr, 2012)

The average annual precipitation in the river basin as a whole is 3,500 mm, but because of the high altitude difference between the different parts of the catchment, the precipitation variation is also large. The driest areas in south west have as little as 1,400 mm per year, whilst the wettest areas around the Cerro de la Muerte in the south have as much as 8,500 mm per year, as seen in figure 7.4 (UDGN, 2008).
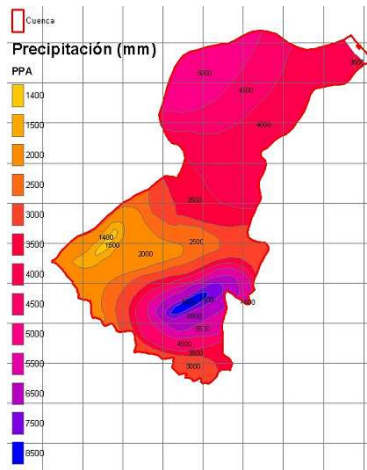
Figure 7.4: Annual precipitation
(UDGN, 2008)

The temporal variation of the precipitation is also large, because of the different climatic zones in the catchment. Two distinct areas in the catchment have a defined dry period in February to March, with very little rain. These are the wet area in the south east and most of the flood plains in the lower region. However, the region in the center of the catchment, as well as the coastal area most downstream, do not have a distinct dry season, and show a more uniform distribution.

7.2.4 Hydropower Plants

The development of hydropower in the Reventazón started in the early '60s with the construction of the Río Macho powerplant in 1963. This powerplant is located in the highest reaches of the catchment, using the water from the Macho, Blanco and Pejibaye rivers. Today, after several upgrades, it also gets water from Grande de Tapantí, Porras, Humo and río Villegas. (Tecun, 2010)

This was shortly followed by the Cachí powerplant in 1966. It is using water from Río Macho and Río Reventazón. The characteristic arch dam in the Cachí reservoir is unique in Costa Rica. Just downstream of Cachí, another power company, Union Fenosa, finished a powerplant called La Joya in 2006. Some distance downstream is Angostura, described in the next section. Today, the water released from Angostura runs without further interventions to the Caribbean coast, but a new hydropower project, the Reventazón hydropower plant, is under construction 38 km downstream. It will start operation in the beginning of the dry season in 2012. The new power plant will use water between 265 and 110 m.a.s.l., and have a capacity of 304.5 MW. (ICE, 2012a,b). A summary of the existing and planned power plants in the Reventazón river basin is shown in table 7.1.

Table 7.1: Hydropower plants in the Reventazón river basin

Power plant	Instal-lation year	Instal-lation MW	Production GWh	Active storage mill. m^3	Operator
			(ICE, 2012b)		
Río Macho	1963	134	522	0.4	ICE
Cachí	1966	103	593	36	ICE
Angostura	2000	180	902	11	ICE
La Joya	2006	50	252		Union Fenosa
Reventazón	2016	300	1430	120	ICE

7.3 Angostura

7.3.1 Specifications

The construction of the Angostura power plant was started in 1993 to increase power production in order to fulfill Costa Rica's goal to become a carbon-neutral nation. The project was finished in October 2000 as the largest powerplant in the country (Vega, 2004).

Most of the water to the powerplant comes from the Reventazón river, with supply from the tributaries Pejibaye/Gato and Atirro. In addition, water is supplied to the reservoir from the small tributaries Tuis and Turrialba via deviation canals. This major confluence allows the power plant to retrieve much water, and with a drainage area of 1,463 km^2, the mean annual inflow is 120 m^3/s. The supplying rivers are shown in figure 7.5.
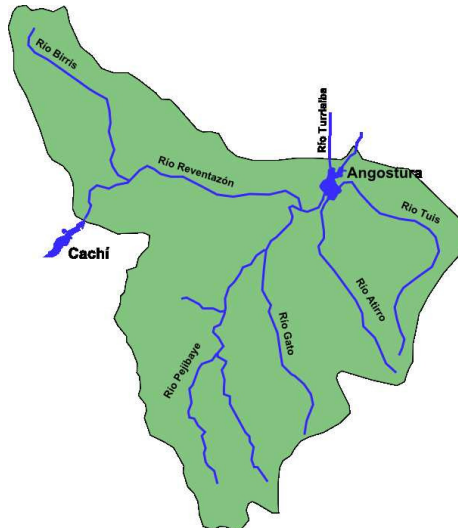

Figure 7.5: Angostura's watershed
Based on (Calderón, 2002)

The design discharge is 160 m^3/s, and the net fall is 124 m. The power plant has an installation of three 60 MW Francis turbines, which gives a yearly production of 902 GWh (UDGN, 2008). The Angostura reservoir, as seen in figure 7.6, is an inundated river, embanked by a 38 m tall rockfill dam with a total crest length of 235 m. The reservoir has an area of about 250 ha, and is regulated between 570 and 577 m.a.s.l., with the lowest bottom level at 552 m.a.s.l (Vega, 2004).

Figure 7.6: Angostura reservoir

The reservoir is designed for daily peaking, with enough storage capacity to fill the reservoir daily during the hours of low consumption, for use in the high-cunsumption hours. To achieve this, in addition to maintaining production in the dry season, an active volume of 2.5 mill m^3 is needed. However, to account for siltation, the total volume of the reservoir at the time of installation was 17 mill m^3, 11 of which was active storage. (Ramirez et al., 2003)

7.3.2   Operation

Compared to Cachí, whose reservoir is located in a natural gorge, Angostura is vulnerable to sedimentation. The upper part of the reservoir is very wide and shallow, with low water velocities. Incoming sediments settle in this area quickly, and is hard to remove. During a flushing event, this area quickly dries up, and the only erosion happens along a narrow flushing channel in the middle.

The upstream powerplants dictate some aspects of how Angostura is operated. When sediments exit Cachí, they inevitably have to go through Angostura. Since 1973, the Cachí reservoir has been flushed annually to maintain the original volume, and this procedure has shown to be effective, in that only 10% of the original volume has been lost over the years (Ramirez et al., 2003). A

flushing event lasts for a short period, where the concentration of sediments in the water is extremely high. Peak measurements have shown as high values as 300,000 ppm (Ramirez et al., 2003). Without mitigation, the water has no means of transporting these quantities through the Angostura reservoir, and they will quickly fill the active storage volume. To prevent this, the reservoirs are flushed in cascade, to pass the sediments through Angostura. This is only efficient for a period of time, and after some years, it is necessary to have an additional full flushing of Angostura. To manage the flushing of large quantities of sediment-laden water, Angostura is designed with two 4 m wide and 5.5 high flushing gates with threshold at 552 m.a.s.l (Ramirez et al., 2003).

Sediment Routing

Cachí is flushed every September. The water level is completely drawn down, and river flow is maintained for 33 hours to erode all sediments. Angostura, however, is not completely emptied. The water level is lowered to 565 m.a.s.l, which is the level of the water intake threshold. This allows most of the incoming sediments to be passed through the reservoir, or at least redistributed to the dead storage volume, but does not remove much of the already settled sediment. As a result, this management strategy alone will leave the reservoir to be filled gradually.

Sediment Flushing

During the first six years of operation, 30% of the storage capacity was lost, and to stop further losses of volume, the full flushings of Angostura started in 2006. In these flushing events, which are performed in November each year, Cachí's sole role is to contribute a sufficient water discharge. Angostura is first slowly drawn down to 570 m.a.s.l., and then the water level is rapidly reduced to 556 m.a.s.l. The purpose of this flushing is to remove the sediments that have settled in the reservoir, including in the dead storage. In this way, it has been possible to maintain the storage volume from 2006.

7.4 Previous Simulations

Before the construction of the dam, the reservoir was modelled numerically using different methods. In 1993, the HEC-6 Corps of Engineers Method, which is a one-dimensional model, was used. In 1994, SSIIM was tested for the first time, using a 5000 cells grid and very large time steps. Two simpler models were tested in 1995, the semi-empirical Brune-USBR method and a vertically bi-dimensional method called RESP (Jimenez et al., 2004). The purpose of the simulations were to assess long-term sedimentation of the reservoir.

Because of the advancement in computational capacity since 1994, the reservoir has been modelled with increased accuracy after the completion of the dam. Further development of SSIIM, including algorithms for sediment erosion and wetting and drying, also make recent simulations superior, allowing for modelling of a more diverse range of water and sediment related phenomena.

In 2010, M.Sc. student Lisa Hoven used a 27,000 cell model to simulate sedimentation and flushing of the reservoir (Hoven, 2010). M.Sc. student Sigurd Løvfall modelled the sedimentation and concentration distribution in 2011 (Løvfall, 2011). Since 2010, PhD student Stefan Haun has done much work on the case, simulating sediment transport, deposition and the November flushing.

Part II
Methods and Results

8   Methods

8.1   RESCON

The water level and flushing discharge for the November 2010 flushing are shown in figure 8.1b. After the full drawdown, the water level and discharge are quite stable, and we can find representative values. There are no measurements of the in situ sediment density, but from experience they are likely to be in the range 1.2-1.4 t/m^3.

(a) 2009   (b) 2010
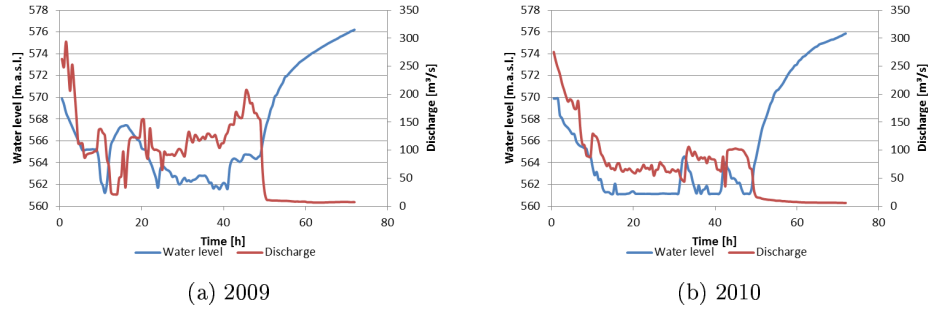
Figure 8.1: Water level and discharge during flushing

The sediment flushing parameter ψ derives from the Tsinghua method, and is set to:

1600	for loess sediments
650	for other sediments with median size finer than 0.1 mm
300	for sediments with median size larger than 0.1 mm
180	for low flushing discharge (< 50 m^3/s in the RESCON model)

According to (Atkinson, 1996), the ratio of an individual observation and the Tsinghua prediction is between 0.5 and 2 for 87% of the observations used to derive the method.

Still, Atkinson observes that these values may not be representative for reservoirs out of China, and suggests dividing by a factor 3 to get accordance with his data. The RESCON model includes this as an extra parameter, *Ans,* which is the value to divide with. The accompanying text with the model suggests setting *Ans* to 3 if the reservoir sediments are significantly larger than the median grain size ($d_{50} = 0.1$ mm), or if the reservoir has been impounded for more than 10 years without sediment removal. Otherwise, it is to be set to 1.

For the flushing in Angostura, the discharge is higher than 50 m^3/s, and we do not have loess sediment. The mean size is somewhat lower than 0.1 mm, so the flushing coefficient could be expected to be between 300 and 650. There is no evidence in the data to suggest dividing by 3, as the reservoir is flushed annually and the deposited sediment are in the order of 0.1 mm. A first guess would be $\psi = 300$.

Input parameters to the model for the November 2010 flushing are shown in table 8.1.

Table 8.1: Input November 2010 flushing

ψ	300	-
Q_f	100	m^3/s
El_{max}	577	m
El_f	562	m
L	3,500	m
T_f	1.54	days
ρ_{dep}	1.3	t/m^3

Using the 2010 flushing as calibration data, the model was tested with the 2009 flushing discharge and water level. These series are shown in figure 8.1a, and are not as stable as the 2010 data. As a result, it was difficult to find a representative discharge, water level and flushing time for the event.

To resolve this problem, the Excel program was rewritten to use the full time series of water level and discharge as input. This was first done for the 2010 flushing, giving a slightly different value than with the constant input. Accordingly, the flushing parameter was calibrated to 16.08, to give a flushed volume of 229,400 m^3.

This value was then used in the model with the flushing time series from November 2009.

To investigate the influence of the input parameters, an analytical parameter sensitivity analysis was performed. This was used to see how much relative or absolute change in one input parameter was needed to get a 10% change in the flushed volume.

8.2   Sediment Concentrations

During the field trip in September 2011, a lot of concentration measurements were made with the LISST in the reservoir. The measurements include vertical profiles along the main reservoir channel, vertical profiles along nine predefined cross sections in the downstream area of the reservoir, and horizontal measurements at constant depth along the same cross sections. The first objective was to analyze the measured data and describe the sediment concentration distribution in the reservoir, in all three directions. The second was to explain physical processes that create the variations in the profiles. The last part was to simulate

64

the case using the numerical model, and assess the model's ability to reproduce
the results.

8.2.1   Measured Concentrations

The LISST measurement data files contain the measured concentration values
in mg/L of the 32 size fractions, along with time of measurement, depth, water
temperature, state of the isokinetic pump and some other variables. The LISST
makes a measurement every two seconds, and each measurement is represented
as a row of values in the worksheet. As explained in section 6.4, the isokinetic
pump caused some problems for some of the measurements. Where the water
velocity was too low, the pump stopped, and the measured concentration val-
ues increased by some 60%. To eliminate this problem from the data set, the
worksheet rows where the isokinetic pump was off, were removed.

Previous assessments of the data have attempted to analyze the results using
color plots. This was continued for some time during the work on this thesis,
but it was seen that parts of the measured information was not fully explained
by this method. In order to get a better grasp on the data, the variation in
each direction in the reservoir was analyzed separately. This makes it easier to
notice and explain the different physical processes affecting the variations in the
concentrations.

The analyze of the variation in the longitudinal direction was based on depth-
averaging the 25 measured vertical profiles along the main reservoir channel.
The concentration variations in the different size fractions was then explained
by physical processes in the reservoir. The results from the numerical model
helped in the understanding of the measured variations.

To analyze the vertical sediment concentration distribution, the vertical mea-
surement profiles were represented in Rouse form, according to equation 2.7.
This representation form allows for a single graph to present the variation in
multiple sediment sizes with different absolute concentrations, without render-
ing small values illegible. The vertical axis in the diagram shows the point
depth divided by a reference depth, usually set as a constant fraction of the
total depth. In the measurements, the exact water depths are not known. This
makes it more natural to choose the lowest level in the measured profile as the
reference depth, which gives a scale from 0 to 1 where 1 is the lowest measure-
ment and 1 is the surface. The horizontal axis shows the concentration divided
by a reference concentration, usually the concentration at the reference depth.
However, some of the measured profiles contain higher concentrations closer to
the surface, which makes it more practical to choose the highest measured con-
centration as the reference value. This limits the values on the x-axis to values
between 0 and 1.

To facilitate the generation of a large number of figures with the same frame-
work, an Excel macro was written in Visual Basic. The macro calculates the
relative depths and concentration values, plots profile's size fractions, and ap-
plies a chosen layout to the figures.

The lateral variation was also assessed separately from the other directions.

The data consists of vertical and horizontal measurements along the nine cross sections, most of which where measured several times in several days. Both the depth-averaged concentrations and concentrations at constant depths were plotted and analyzed. However, the variation in the data was large, with contradicting trends from day to day, as well as inconsistent variations along a single cross section measured within half an hour. In general, the data seemed to give little consistent information, and no general trends were observed. Until better measurements are acquired, the analysis of the concentration variation in lateral direction will have to wait.

8.2.2 Size Fractions

Sediment particles of different sizes behave differently, and as a result, the variations in the distribution in the reservoir will be different for fine and coarse sediments. The LISST measures concentrations in 32 separate size fractions, but it is not necessary to use all these fractions to explain the variations. In the measured data from Angostura, a typical LISST measurement particle size distribution looks like figure 8.2. The high concentration values for small particles stem from particles outside the range of measurable particle sizes, as explained in section 6.4. Some measurements show high values for the coarse particles as well, even far downstream in the reservoir. As these high concentrations are measured close to the surface, it is very likely that this is not sediment, but rather floating organic matter.
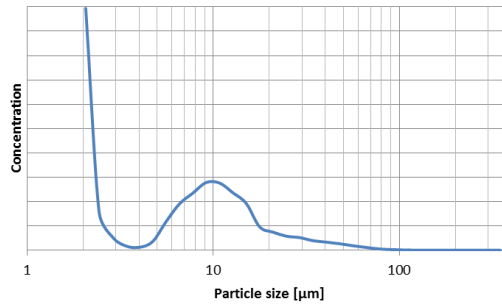
Figure 8.2: Typical LISST measurement

The concentrations in the finest fractions are of no value, as the measurements are erroneous. The finest sediments are kept completely suspended throughout the reservoir, so its interest is anyway limited. The coarsest fractions, i.e. $d > 50$ μm, show little or no concentrations in most measurements, as coarse sediments settle early in the reservoir, or are transported as bed load. Previous versions of SSIIM had a support for maximum 9 sediment sizes, but this has been expanded to 50 as of April this year. This allows for simulation of all of the 32 size fractions from the LISST, but this seems superfluous. As the coarsest bins are empty and the finest contain sediment kept in suspension, and

66

without reliable measurements for verification, these fractions can be excluded from the simulations.

The particle size has a large influence on the sediment transport processes, which is seen in the sedimentation of coarser sediments in the upper range of the reservoir, but also in the vertical distribution of sediments and the spatial sediment patterns in the secondary currents. However, both measurements and simulations show that these trends are not susceptible to the small changes in the particle size, so little information is lost by collocating some sediment size groups. Such a grouping, in contrast to selecting, say, every second size bin, allows for comparing the total sediment concentration as well as the individual size groups.

Also from a perspective of the ease of reading the results and the scope of the analysis, a reduction in the total number of sediment classes is advantageous. It is found suitable to reduce the number of size classes to eight, which is enough to cover the variation without losing much information, while still being easy to interpret. To capture most of the processes and avoid convolution, the LISST fractions are grouped two and two so as to cover the main Gauss-shape seen in the measurements. The settling velocities of the sediments are calculated according to Stokes' law (equation 2.5). The chosen partitioning is shown for the typical LISST measurement in figure 8.3 and along with the settling velocities in table 8.2.
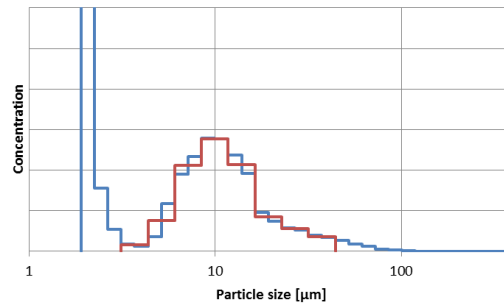

Figure 8.3: Size bins

Table 8.2: Size bins

Bin	Lower μm	Median μm	Upper μm	w mm/s
1	34.1	37.5	40.6	1.26
2	24.7	26.9	34.1	0.65
3	17.7	19.3	24.7	0.34
4	12.7	13.9	17.7	0.17
5	9.2	10.0	12.7	0.089
6	6.6	7.2	9.2	0.046
7	4.7	5.1	6.6	0.024
8	3.4	3.7	4.7	0.012

8.2.3 Simulated Concentrations

The aim on the concentration simulation was to replicate the measured concentration data. x and y coordinates from the 15 measurements were added in the *interpol* file in SSIIM, and the F 48 16 data set was used to write a *.vtk* file containing the concentration values of all size fractions in up to 16 cells over the depth. This file was opened in Microsoft Excel, where a custom-made macro was written to extract and manipulate the relevant information. The information was handled differently for the longitudinal and vertical distribution plots. The longitudinal plot employed depth-averaged concentrations, so the concentration values in each cross section were averaged. The vertical plots were made with the macro described in section 8.2.1. In the *.vtk* file, the information is arranged according to the size fractions. In order to make the Rouse plots, the macro needed to separate the information for each vertical profile and calculate the relative concentrations and depths. A total of 99 simulations were run to get the best results.

8.2.4 Grid Generation

In order to save time, the grid used for the simulations in this thesis was developed by Stefan Haun in advance. I have later adjusted it to improve the results. The basis for the geometry is bathymetry data obtained by echo sounding performed by a hydrological team from ICE on September 7 and 8. The data was read by SSIIM, and geodata points were inserted along the border and around the islands, adding the geometry that was not possible to measure by boat. The measured and added points are displayed in figure 8.4, where the colors represent different elevations of the points.
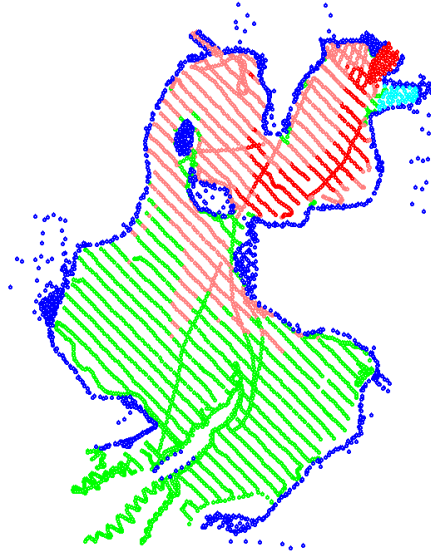
Figure 8.4: Geodata

The grid was generated according to the procedure explained in section 5.3. A single block was used, covering the whole reservoir, touching the inflow and outflow areas. The grid is unstructured and non-orthogonal, with hexagonal cells, and is using the wetting and drying algorithm. The grid block size is 109x109x15 cells, with a total of 43,189 active cells at water level 577 m.a.s.l.

The grid has three inflow areas and one outflow area. Experience from previous simulations of the reservoir shows that the Tuis river has little influence on the flow field, concentration and sedimentation patterns in the reservoir. Grid problems have also been experienced in the Tuis inflow area, so to avoid problems, the inflow from the Tuis river is neglected.

During the work with the simulations, it became apparent that the grid needed improvements. The bed level in the narrow passage between the peninsula and the largest island was not sufficiently covered by the bathymetry measurements, which when interpolated in SSIIM led to a too low level in the modeled passage. To improve this, new geodata points were added in this area. The basis for the new elevations were depth measurements with ADCP. In accordance with known water level at the weir at the time of the measurements, a simulation in SSIIM was performed to find the water level in the passage, and then the bed levels were calculated from the ADCP depths. The final grid used for the simulations is shown in figure 8.5 at water level 577 m.a.s.l., i.e. the highest regulated water level.
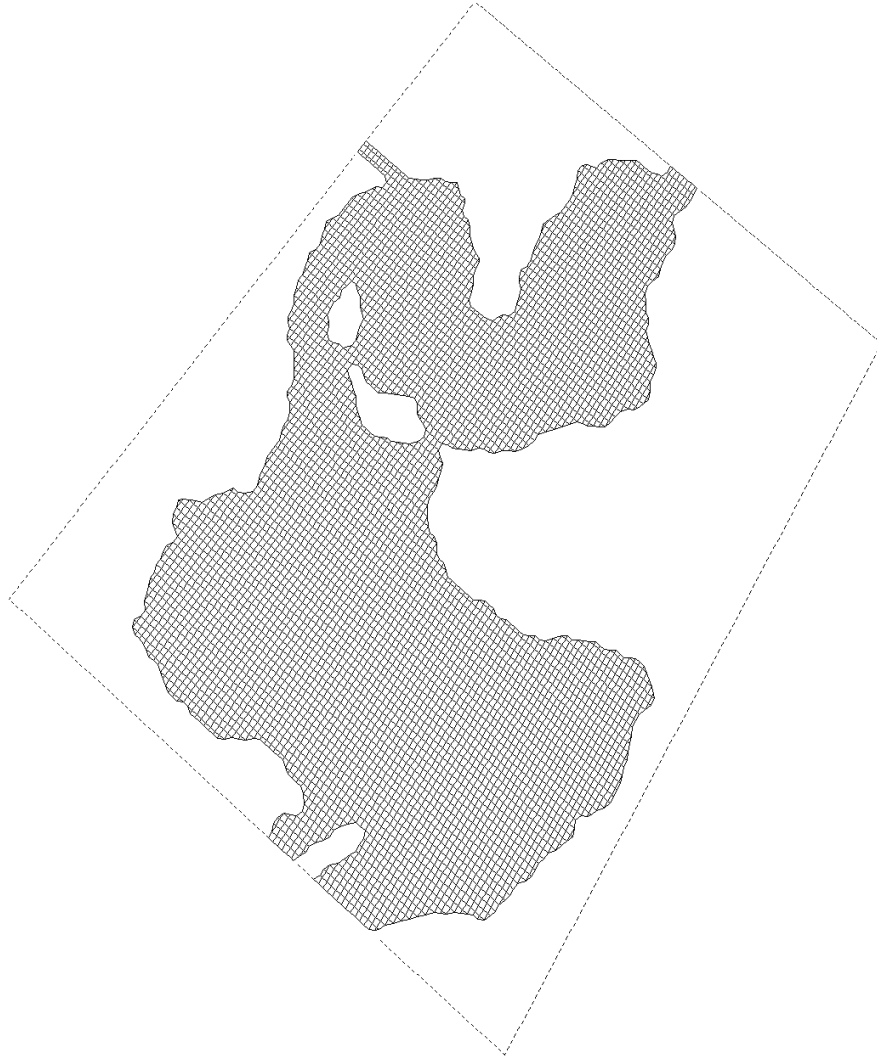
Figure 8.5: Grid used for the simulations

8.2.5   Water Input

The Reventazón catchment is the Costa Rican catchment with most available hydrological information, because of its long history of hydroelectric importance (Alvarado et al., 1993). In the catchment as a whole, there are installed more than 25 hydrological stations, about half of which are in operation today. The station with the longest observations is the Angostura station, which was installed in 1953 in what is today downstream the Angostura reservoir. Upstream the reservoir is Cola del Embalse Angostura, which measures the discharge into

70

Angostura from the Reventazón river. The discharge is also measured and logged every 30 minutes in the small tributaries Tuis and Turrialba. The discharge in Atirro, however, is not in the log files, so this value has to be estimated in order to know all the inflows. In addition to discharges, the water level in the reservoir is also logged. The variation in water levels and discharges is significant over the course of a day, especially from Río Reventazón, which is heavily influenced by the operation of the upstream powerplants. There is usually a peak around 8 in the morning, after which the discharge normally remains constant for several hours. The pattern in the water level is more unpredictable, as it is influenced both by the volume of inflowing water and the consumption at the Angostura powerplant.

During the measurements on September 13, the discharges are stable for the whole period, while the water level decreases slightly from 576.1 to 575.9. The average values, which are used for the simulations, are summed up in table 8.3. The discharge in Atirro is assumed to be 9 m^3/s.

Table 8.3: Average water level and discharges during measurements

Water level	m.a.s.l.	576.0
Reventazón	m^3/s	78.5
Atirro	m^3/s	9.0
Turrialba	m^3/s	2.7

8.2.6 Sediment Inflow

ICE performs periodic measurements of sediment concentrations in their measurement stations. For these calculations, a set of 714 measurement pairs of water discharge and sediment concentration from the Cola del Embalse station are used. The earliest measurement is from 1974, and the latest from 2009, and 1994 is the year which is best covered, with 186 measurements.

The inflow of sediments to the reservoir at the time of the measurements is unknown. To reduce the uncertainty, a relationship should be established between the discharge and the concentration. The validity of a rating curve for prediction of a single concentration is very low because of the inevitable variability in the data, but it may help put a bound on the guessed values. Moreover, because of the large seasonal variation both in discharge and sediment concentration, a relationship based on data for the whole year might not be representative for single months. Hence, for a best estimate of the concentration at a given discharge in September, only data from the same season should be used, if sufficient data is available. There are 112 measurements from September in the series, and it is seen from figure 8.6 that September in general has a higher sediment concentration than the average for the year, especially at low discharges. This is because of the dry season's low sediment concentrations have a high influence on the annual average concentration for low discharges. Figure 8.6 shows the 25, 50, 75 and 90% percentiles of the concentration measurements for the different discharges.

(a) Full year   (b) September
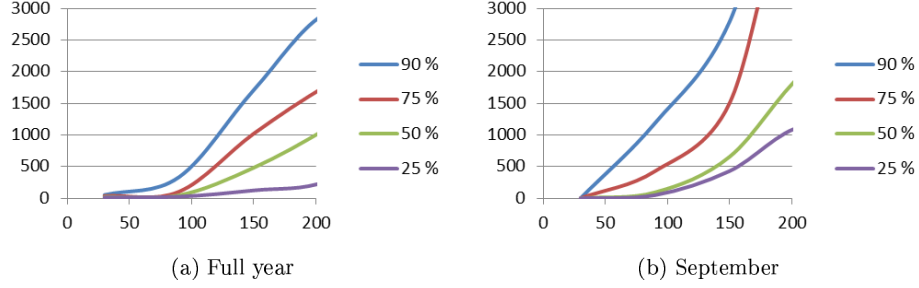
Figure 8.6: Rating curve

The rating curve is not used to estimate the sediment concentration during the specific day. This would not be very useful, as the variation from day to day is substantial. In stead, the measured suspended sediment grain-size distributions from the reservoir were used as input, and scaled to best fit the observed concentrations. Because of the large expansion in the flow area where the river enters the reservoir, a portion of the sediment will settle in the first meters of the reservoir. Hence, the inflowing sediment concentration is necessarily larger and has a slightly higher portion of coarse sediment than the values that were measured some 300 m downstream. Each size fraction was therefore scaled individually to best match the measured values, while still maintaining a plausible grain-size distribution in the inflow. The total concentration was then controlled against the rating curve to see if it was within a credible range.

For the sediment inflow from the other rivers, little is known. From conversations with the employees at ICE, we know that there was a sand slide upstream in Atirro prior to the measurements on September 13. From this, in addition to the effect of the Reventazón regulation, it is probable that the concentration in Atirro was higher than in Reventazón. An estimate of twice as high concentrations was used for the simulation. The Turrialba river was thought to have about the same concentration as Reventazón from observation of the water color.

(a) Reventazón   (b) Atirro   (c) Turrialba

Figure 8.7: Inflow concentrations September 13

Figure 8.7 shows the sediment grain-size distributions used in the longi-

72

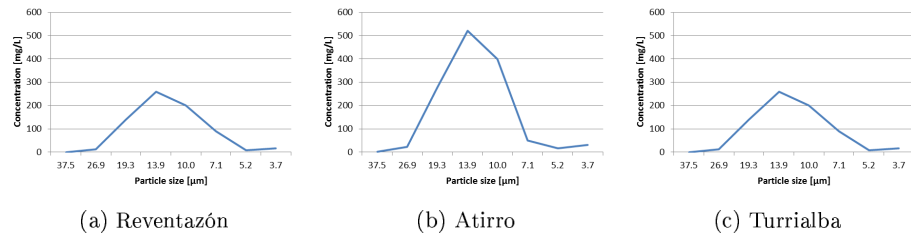tudinal steady state simulation for the incoming sediment in the three rivers. Multiplied with the corresponding discharges, the absolute sediment inflow from Reventazón, Atirro and Turrialba is 56.9, 11.9 and 2.0 kg/s in this simulation.

8.2.7 Bed Sediment

25 bed sediment samples were collected from different parts of the reservoir in September 2011. The samples were analyzed by sieve analysis with mesh sizes from 0.073 to 4.0 mm. Used as bed material input in SSIIM for the steady state simulation, the analyzed particle sizes are mostly out of the simulated range. An average of 30% of the material was finer than the finest mesh. A sample taken in 2007 was analyzed further, covering also the clay fraction. This measurement was sampled in the shallow upstream area of the reservoir and contained 23% clay, 71% silt and 6% sand (Hoven, 2010).

The samples from 2011 shows the coarsest sediment in the downstream end of the reservoir. This is counterintuitive, and the most likely explanation is that more fine material leaked out of the sediment grabber in the downstream end, where it is deeper. Discarding these samples, the measurements are more according to theory, with coarser sediment in the inflow area and finer on the flat planes and further downstream. A median measurement was used for the estimation of the bed grain-size distribution.

8.2.8 Roughness

Simulations showed that the bed roughness has little influence on the sediment concentration distribution compared to the other parameters, such as geometry and inflow of water and sediment. For the concentration simulation, the roughness height was set to 1 cm.

8.2.9 Time

The time-step of a simulation is of great importance. A too long step will give instabilities in the solution, while a too short step gives extensive computation times. It is therefore important to find a trade-off between these interests. In this case, a time-step of 50 seconds was found to be stable, while still not demanding too much computational resources.

The duration of the simulation is also important. The simulation starts with clear water in the whole reservoir, and a constant inflow of sediments will gradually establish a steady-state situation. It was found that 500,000 seconds, which is almost 6 days, was sufficient for the concentration distribution in the reservoir to stabilize. Using all 8 processor cores in the computer, these simulations took about 8 hours.

8.3 Flushing

Limited time was allocated for the flushing simulations, and the work was additionally postponed because of much work with the figures for the article. As

a result, only three weeks was available from the first attempt at a flushing simulation. Furthermore, we waited long before asking for the measured inflow concentrations from ICE, and the files were kept in bureaucracy longer than expected. The files arrived only a week before the thesis deadline, so there was not enough time to get an optimal result.

8.3.1 Time

The drawdown started from 576.0 m.a.s.l. on September 13 around midnight, and this level was reached again around midnight of September 18. The total duration of the flushing is 120 hours. Most of the erosion in the reservoir happens when the water level is at the lowest, but for the simulation to run, it has to start at a higher water level, and then be drawn down. The full 120 hours is therefore simulated.

A time step of 50 seconds gave a stable simulation, but a higher number of inner iterations was needed than for the steady state simulation, and a value of 50 was used.

8.3.2 Water Input

For the discharges and water levels during the flushing, the same log file from ICE was used as for the concentration simulation. The inflow from both Tuis and Turrialba was ignored in the simulations, because of the small discharges compared to that of Reventazón. The discharge from Atirro was estimated at $9 \text{ m}^3/\text{s}$.

The hydrograph during the flushing contains two large peaks: one as the water level has reached the minimum level, and one just before the water level starts to rise. Although the average discharge during the flushing is about 80 m^3/s, the magnitude of the largest peak is 380 m^3/s. The rapid changes in discharge represents a stability problem for the simulation. When the water level is low and the discharge changes quickly, there is a great chance of a grid split. This is caused by multiple cells drying up, separating the inflow area from the outflow area. SSIIM does not allow a variable time step or number of inner iterations, and to prevent the time of the simulation to exceed any acceptable level, these values have to be kept at a reasonable level. To mitigate this problem, the hydrograph was smoothened, making the temporal gradients smaller, and reducing the total magnitude of the peaks.

The water level has a more stable time line than the discharge. The level is reduced slowly to 574 m.a.s.l., then rapidly to the lowest level of 565 m.a.s.l., where it is kept for about 50 hours, and finally increased again. The discharge and water level series are displayed in figure 8.8.
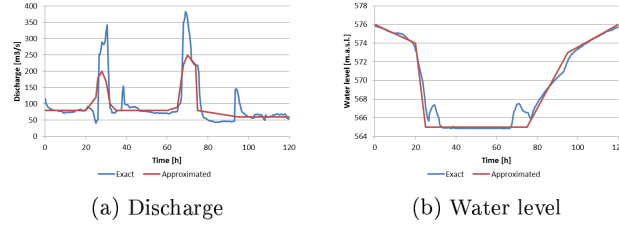
(a) Discharge   (b) Water level

Figure 8.8: Input series for flushing

8.3.3 Sediment Inflow

The sediment inflow was unknown for a long time. We waited too long before requesting the files from ICE, and the were caught in bureaucracy for some time. It was only on June 2 that the file was received, making the time available for the final simulations very limited. The concentration measurements were performed by ICE using a USGS depth-averaging suspended sediment sampler, at an average of about three measurements per hour. Unfortunately, the logged series ends at a peak, before the flushing is finished, so the rest of the time series had to be estimated. The grain-size distribution of the inflowing sediment is unknown.

8.3.4 Bed Sediment

As the objective of the flushing simulation is to simulate the amount and distribution of flushed sediment, fewer sediment sizes had to be simulated. Still, coarse and fine materials behave very differently during a flushing, both with respect to erosion, transport and sedimentation. Four sizes were chosen, which covers the main range from the samples. The sizes were chosen so that each fraction contained 25% of the bed sediment from the samples. The resulting sizes were 300, 100, 30 and 2 μm.

8.3.5 Roughness

Different roughness values were used during the optimization, and a value of 0.1 m was used in the final simulation.

8.3.6 Progress

Sediment flushing is difficult, and there are many different algorithms to test. It takes quite a lot of time to find a set of algorithms that gives a stable simulation, and even longer to get good results.

    Getting the simulation to run properly was the first problem encountered. The wetting and drying algorithm is sensitive when the water level is low and the discharge is high, so there is a great chance for the inflow area to get separated from the outflow. One possible method is to manually set the water level

75

upstream as well as downstream. This gives better control of the water surface, but without a measurement of the upstream level during the drawdown, the method is not very accurate. However, after changing the parameters for a while, the simulation run well without the upstream reference value. In the first simulations, there was a problem with a laterally skewed water surface, which is caused by some assumptions in the algorithms for calculating the upstream water level from the downstream reference cell. Variations of the algorithm gave a better result. Another problem was the peaks in the discharge time series. As explained earlier, this series was smoothened to get better stability in the simulation.

When the simulation run well, the problem was to improve the results. As with any model, calibration is needed, and a lot of different parameters may be varied that will influence the results. The largest problem seemed to be getting sedimentation in the downstream range of the reservoir. This was first solved in the penultimate simulations. The default implementation of the van Rijn bed load formula assumes that bed load is below a given level. When the distance from the center of the bed cell to the bed is different from the value van Rijn subscribed, this results in a wrong estimate. The F 60 1 data set solves this by using an extrapolation algorithm based on the Hunter Rouse distribution. Using this algorithm, there was erosion in the upstream end and sedimentation in the downstream end.

9 Results

9.1 RESCON

The initial run with static water level and discharge for the 2010 flushing yielded 3.81 million m^3. Compared to the value of 229,400 m^3 from the bathymetry data assessed with SSIIM, this is 16.6 times higher than expected.

With the full time series as input, the flushed volume was 4.28 million m^3. Calibrating the flushing parameter to 16.08, the model yielded 229,400 m^3.

When the calibrated model was run with the 2009 time series, the result was 296,681 m^3. The values from the bathymetry data was 349,000 m^3.

The results are displayed in figure 9.1. In 9.1a all results are shown, and in 9.1b only the bathymetry data and the results from the calibrated model.
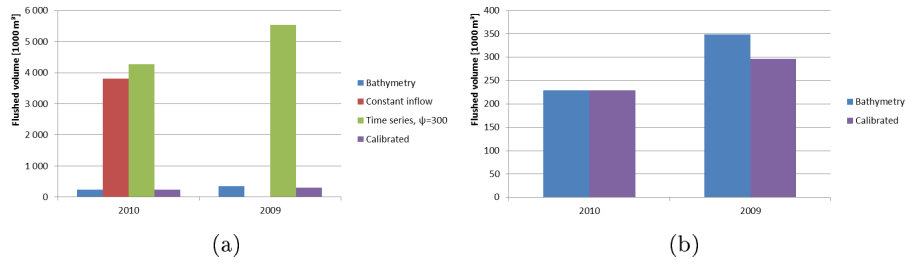
Figure 9.1: RESCON results

9.2 Duplicate Measurements

Figure 9.2 shows the measured vertical concentration distributions for five measurements in the same location.

(a) Duplicate 1   (b) Duplicate 2   (c) Duplicate 3

(d) Duplicate 4   (e) Duplicate 5
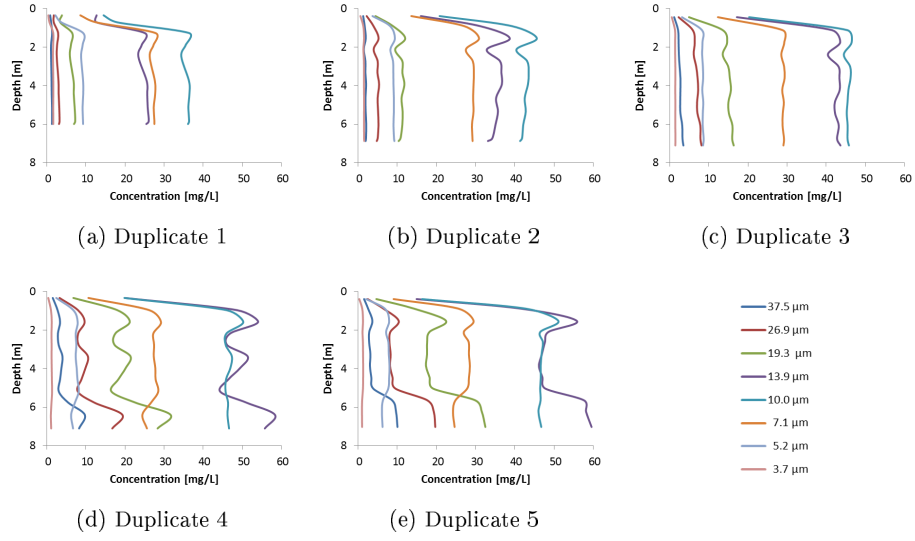
Figure 9.2: Duplicate measurements

Figure 9.3 shows the simulated velocity fields from the first-order power-law simulation and the second-order upwind simulation.

(a) POW   (b) SOU
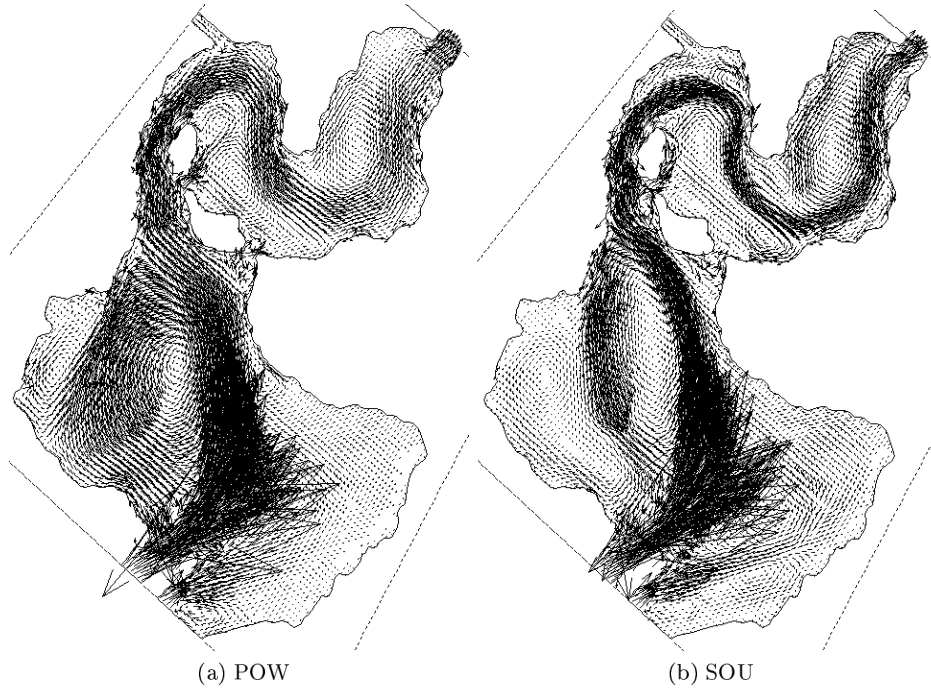
Figure 9.3: Velocity fields from the POW and SOU schemes

Figure 9.4 shows contour lines of the simulated concentration distribution of particle size 13.9 µm, for the two discretization schemes.

<div align="center">(a) POW   (b) SOU</div>
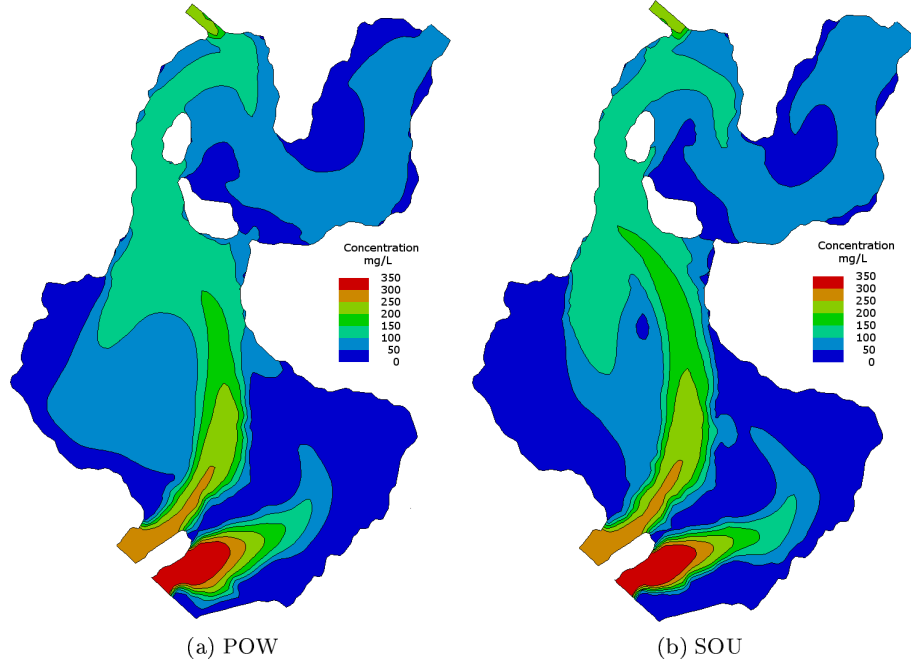
Figure 9.4: Simulated concentration distributions, 13.9 µm

9.3 Longitudinal Concentration Distribution

Figure 9.5 shows the depth-averaged concentrations following the original river channel, for the different size fractions. Figure *a* shows the concentration measurements, figure *b* the results from the first-order power-law scheme simulation, and figure *c* the results from the second-order upwind scheme simulation.

(a) LISST

(b) POW

(c) SOU

| 37.5 μm | 26.9 μm | 19.3 μm | 13.9 μm |
| 10.0 μm | 7.2 μm | 5.1 μm | 3.7 μm |
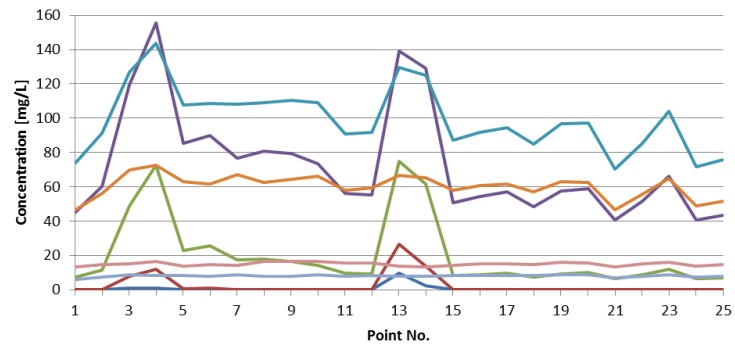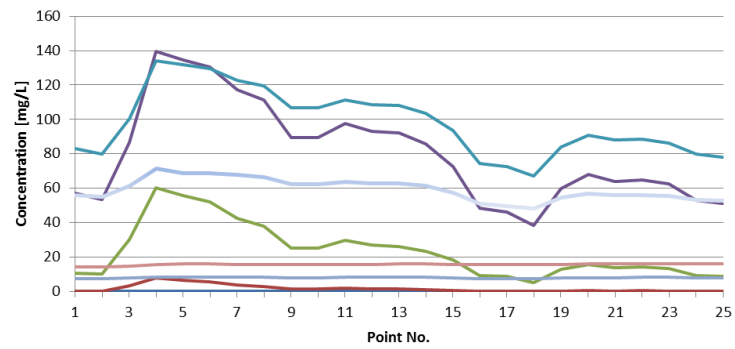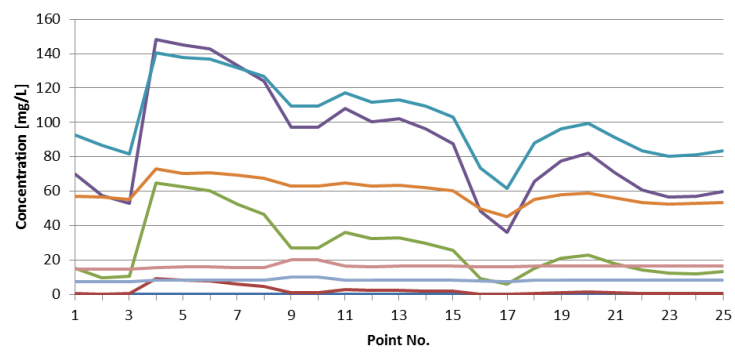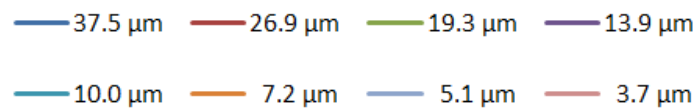
Figure 9.5: Longitudinal depth-averaged comparison

9.4 Vertical Concentration Distribution

Figure 9.6 shows Rouse profiles of the vertical concentration measurements.
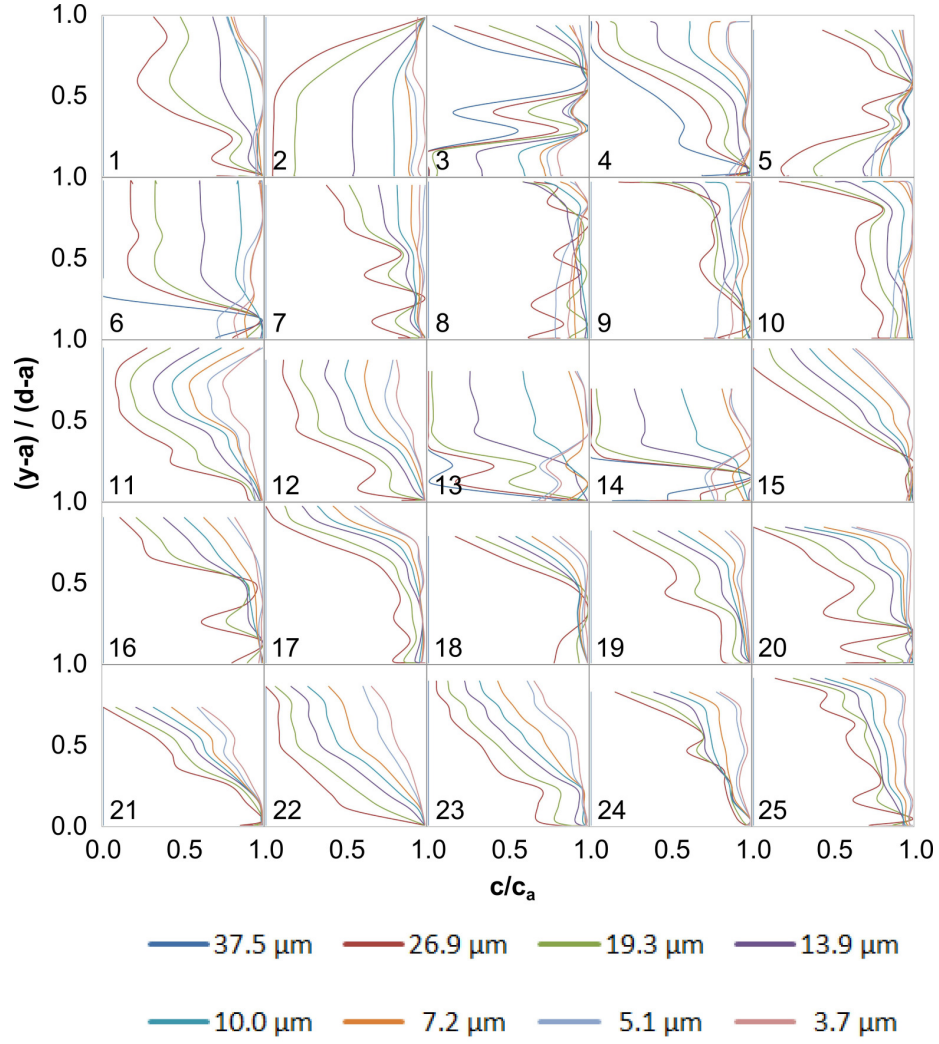
Figure 9.6: Rouse profiles from LISST measurements

Figure 9.7 shows Rouse profiles of the results from the simulation with the first-order power-law scheme.
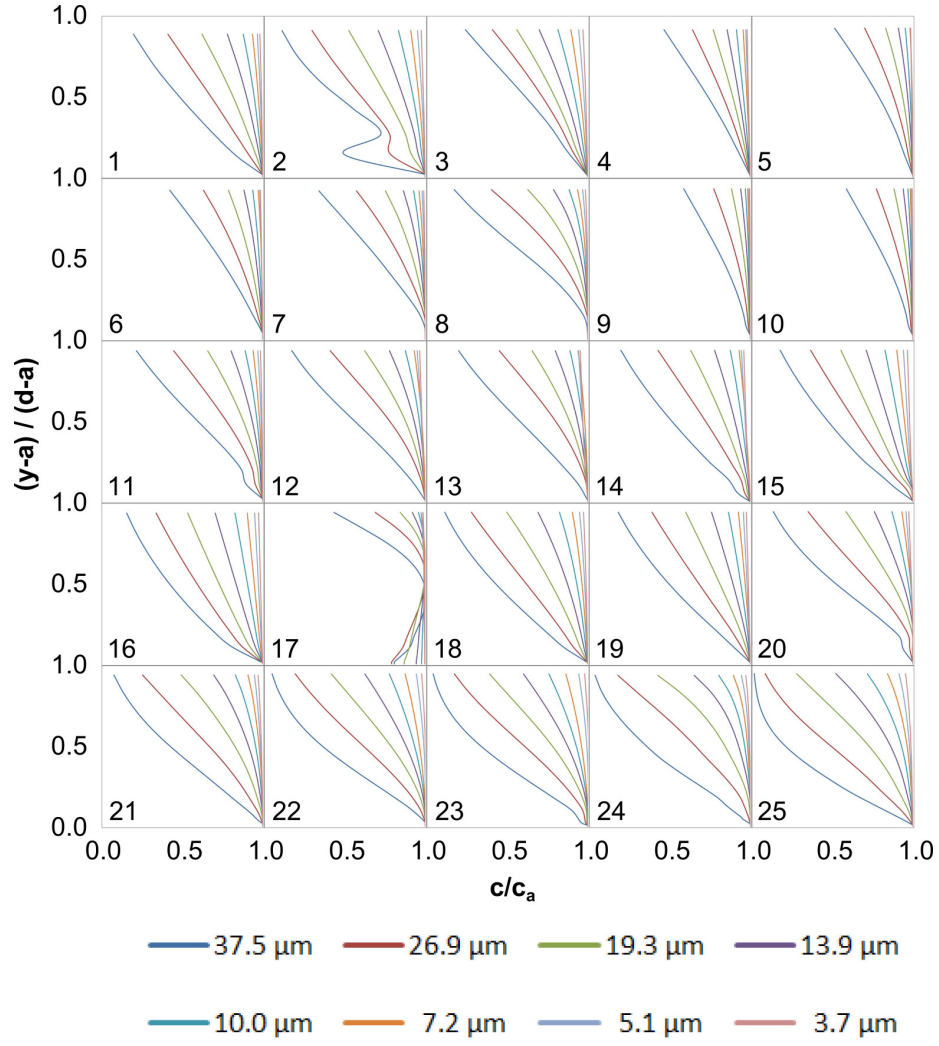
Figure 9.7: Rouse profiles from POW simulation

Figure 9.8 shows Rouse profiles of the results from the simulation with the second-order upwind scheme.
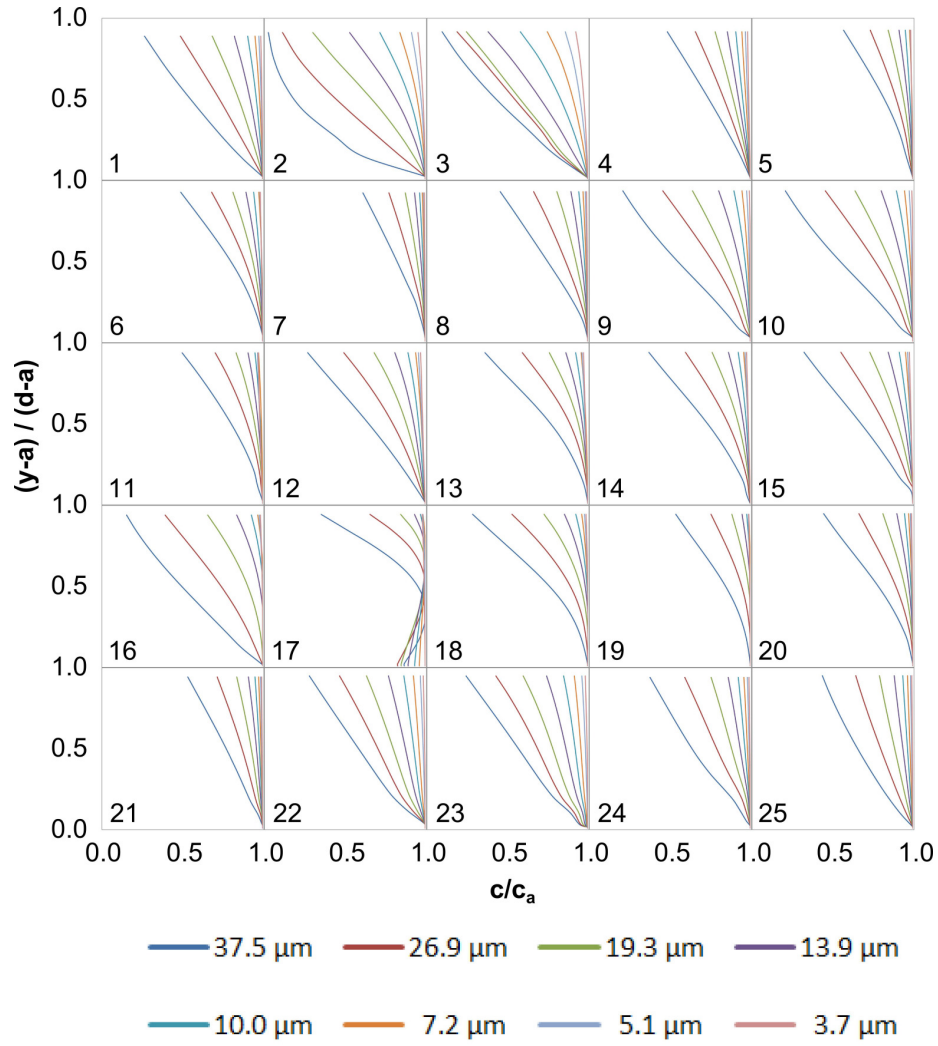
Figure 9.8: Rouse profiles from SOU simulation

9.5 Flushing

Figure 9.9 shows the measured and simulated bed changes in the reservoir during the flushing. The measured results are created by subtracting measured bathymetry data before the flushing from similar measurements after.

(a) Measured bed changes   (b) Simulated bed changes
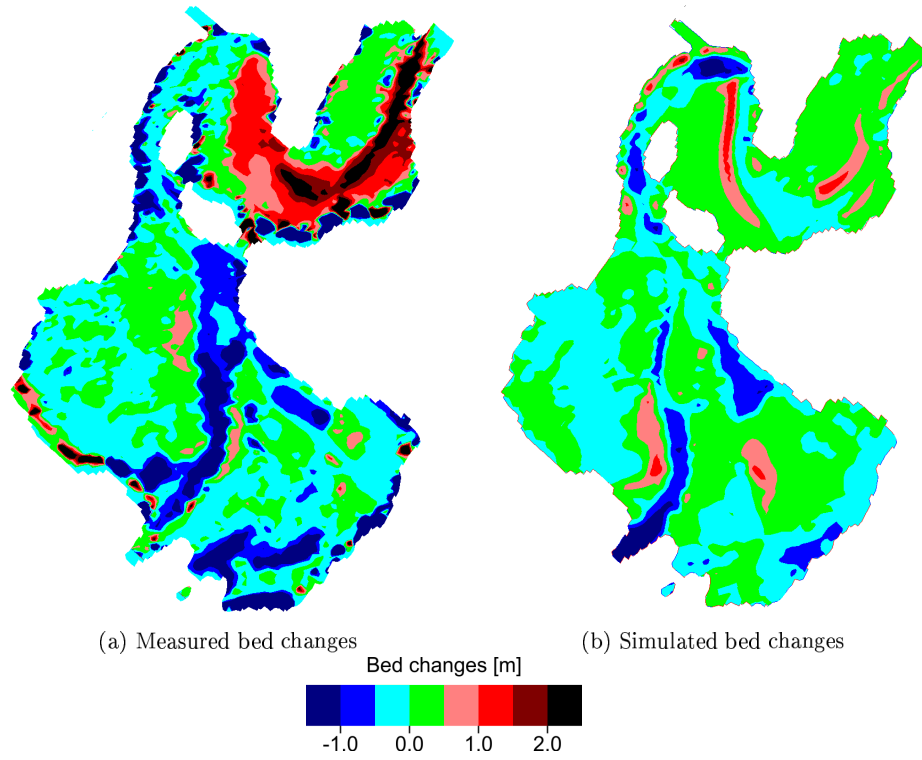
Figure 9.9: Measured and simulated bed changes

The total volume of removed sediments from the reservoir based on the bathymetry data is 221,331 m^3. The final simulation removed 141,173 m^3, but this number does not make much sense without the correct erosion distribution in the reservoir.

Part III
Discussion and Conclusion

10 Discussion

10.1 RESCON

10.1.1 Parameter Sensitivity

In Angostura, flushing channel will always be narrower than the reservoir width, so the width and side slope of the reservoir does not affect the carrying capacity. As a result, the only parameters affecting the result are:

ψ, Q_f, El_{max}, El_f, L, T_f, ρ_{dep}

The formulas are summarized in table 10.1, along with the differential propagation of uncertainty.

Table 10.1: Parameter sensitivity

Formula	Error propagation
$V_f = Q_s \cdot T_f \cdot \rho_s^{-1}$	$\frac{dV_f}{Vf} = \frac{dQ_s}{Q_s} + \frac{dT_f}{T_f} + \frac{d\rho_{dep}}{\rho_{dep}}$
$Q_s = \psi \cdot Q_f^{1.6} \cdot S^{1.2} \cdot W^{-0.6}$	$\frac{dQ_s}{Q_s} = \frac{d\psi}{\psi} + 1.6\frac{dQ_f}{Qf} + 1.2\frac{dS}{S} + 0.6\frac{dW}{W}$
$S = \frac{El_{max} - El_f}{L}$	$\frac{dS}{S} = \frac{dEl_{max} + dEl_f}{El_{max} - El_f} + \frac{dL}{L}$
$W_f = 12.8 \cdot Q_f^{0.5}$	$\frac{dW_f}{W_f} = 0.5\frac{dQ_f}{Q_f}$

As W and Q_f are not independent, the uncertainty in V_f will not be the sum of the two uncertainties. The total uncertainty in V_f is given in equation 10.1.

$$\frac{dV_f}{Vf} = \frac{d\psi}{\psi} + 1.1\frac{dQ_f}{Qf} + 1.2\frac{dEl_{max} + dEl_f}{El_{max} - El_f} + 1.2\frac{dL}{L} + \frac{dT_f}{T_f} + \frac{d\rho_{dep}}{\rho_{dep}} \quad (10.1)$$

From this, we can see how much the parameters much be varied to get a specified change in the flushed volume.

Table 10.2: Variation in parameters to get 10% change in flushed volume

Var	Rel.chng.	Abs.chng.	Unit
ψ	10.0%		-
Q_f	9.1%	9.1	m^3/s
El_{max}	8.3%	1.2	m
El_f	8.3%	1.2	m
L	8.3%	290	m
T_f	10.0%	0.15	days
ρ_{dep}	10.0%	0.13	t/m^3

10.1.2 Discussion

The results from the flushing model is only the volume of flushed sediment. It gives no information about the distribution within the reservoir. In the full RESCON model, the effects of dead and live storage on the long-term capacity is estimated by letting the trap efficiency change according to (Brune, 1953).

The model is not made for sediment pass-through, as there is no method for dealing with the incoming sediment during the flushing. For this reason, the model is inadequate for the modeling of the September flushing in Angostura.

Giving results 10-20 times the observed values, the model was unable to match the actual flushed volume without transcending the recommended range of the parameters. Since the model is linear in the flushing parameter, changing this to a value far out of the recommended range forces the model to give the right volume of flushed sediment. However, this undermines the purpose of the model, which is to get a quick estimate of the flushed volume with only easily accessible data. The calculated flushing channel width in the model is not as large as the actual flushing channel width. Nevertheless, manually setting the width is not sufficient to give a more reasonable result. Moreover, even after calibrating the model by changing the discharge coefficient to match the flushed volume in one case, the model fails to predict the results in a second case.

These are all indicators of the model being too simplistic to model these situations. The Angostura hydropower reservoir has a complex geometry, and a simplistic model based on best-fit results from other, probably more standard-shaped, reservoirs is insufficient to estimate both the total quantities and relative changes in the flushed volume for different cases. The model is probably more suited for reservoirs with straight center lines, where complex flow fields and geometric obstructions are not affecting the flushing processes.

10.2 Duplicate Measurements

To evaluate the variability in the LISST measurements, the vertical concentration distribution was measured five times in a single location. The duration of each measurement was about 20 seconds, and the time between the start of each measurement was approximately one minute. The measurements were performed in the downstream range of the reservoir, in the outer part of the last curve, as seen in figure 10.1.

Figure 10.1: Location of duplicate measurements

The results were displayed in figure 9.2 For a single location and a short time span of about five minutes, the variation is large. The coarse material shows a concentration peak close to the bed for the two last measurements, while the three first are more uniform. Apart from this peak, the trend is more or less homogeneous over the depth, with the latter measurements having higher concentrations. For the finer material, the variation is slightly less, and without the peak.

When averaging over the depth, we get the results shown in figure 10.2. Apart from the finest sediment fractions, where the variations are smaller, the order of the five measurements according to concentrations are the same for all the particle sizes. The relative variability is largest for the coarsest material. There is also a distinct correlation between the concentration and the mean particle size, i.e. the measurements with the highest sediment concentrations have coarser material.

(a) Absolute   (b) Deviation from average
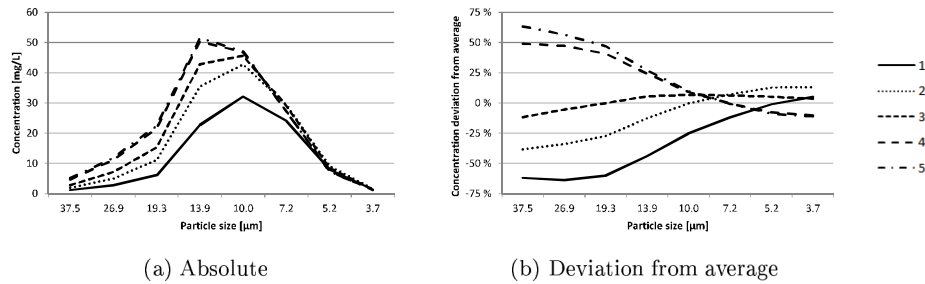
Figure 10.2: Depth-averaged variability in duplicate measurements

The instrument entering the bed load is a probable cause for the bottom peak in the two last measurements. This would explain the amount of coarse material. The depth of duplicate 2 and 3 is however in the same range as the two last, without showing signs of bedload. As the variation above the lowest meter is also significant, bed load can not be the only explanation.

The variance is most likely not caused by the instrument. The variability is systematic, and in accordance with a change in the flow field during the measurements. The location for the measurements was in the outer range of a curve, and the flow field is susceptible to slight changes in the water inflow, or other disturbances. Drifting of the boat is another likely explanation for the variability, as it is difficult to make the measurements in the exact same location several times, and the spatial concentration gradients may be steep.

These concentration fluctuations are probably not representative for the whole reservoir. Where the flow field is more stable, we would still expect trust-worthy and representative measurements. However, some areas will inevitably me more difficult to assess, and a single measurement will not be sufficient to represent the concentrations.

10.3   Velocity Field

The simulated velocity field from the first-order power-law scheme and the second-order upwind scheme were seen in figures 9.3. The second-order scheme shows a more concentrated flow in the upstream part of the reservoir, and the large vortex covering most of this area is more stretched longitudinally. Downstream of the islands, the second-order scheme shows a more complex flow field with more and stronger eddies, and a concentrated main flow. In the bends downstream of the small island, the main flow cuts through the curves. The second-order scheme gives steeper gradients, which corresponds to the observed flow, but the location of the main currents deviates in some locations from what was seen in the field. Slight changes in geometry or inflow parameters is known to influence the shape of the eddies.

There is no real verification data for the velocity field in the reservoir. Although ADCP measurements were performed during concentration measurements, the quality of the measurements make them counterproductive in the object of verification of model results. As a result, the best indicators of the real velocity field are observations in the field, and the measured concentration distribution.

10.4   Longitudinal Concentration Distribution

10.4.1   Measured

The depth-averaged longitudinal distribution of the different sediment sizes in the reservoir is shown in figure 9.5 a. There are two notable peaks at measurement points 4 and 13-14, with a more stable decrease across the reservoir length in the other areas. The relative size of the peaks is larger for the coarse material than for the fine. Another important observation is the low concentration in the first two measurements.

The largest concentrations will always follow the main water flow in the reservoir, and in Angostura, The water from the Reventazón river predominates the flow field. If some measurements are made in this zone and others outside, the measured concentrations will vary accordingly.

The final simulation with the second-order upwind scheme, which matches the measurements reasonably well, is used to illustrate this. Figure 10.3 shows contour lines for the concentration of sediment size 13.9 µm along with the measurement locations.
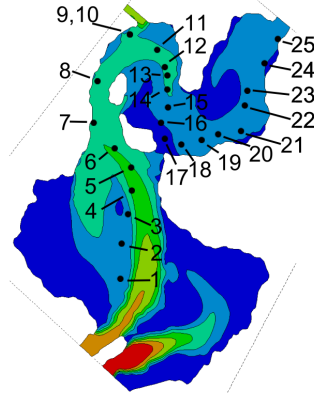
Figure 10.3: Simulated concentration distribution, 13.9 µm

The first two measurements are clearly out of the main flow, which explains the measured low concentrations, both compared to the first peak and the forthcoming measurements.

The concentration peak at point 4 is measured in the flow center, and the surrounding measurements along the zone's borderline. The magnitude of this peak is also amplified by the confluence of Reventazón and Atirro.

While measurements 5 through 12 show low concentrations, the main flow zone in the simulation also covers point 5-8. The real main flow is probably more concentrated and crossing between measurement 5 and 6.

The second large peak in the measurements, in points 13-14, was first believed to be caused by the inflow from the Turrialba river. However, the simulations indicated that the low discharge from this river was not sufficient to cause high concentrations in this location. The real cause is again probably the location in the middle of the main flow. As seen in the next section, the two measurements also contain bedload, which makes the magnitude of the peak even larger.

In the downstream area, below point 15, the concentration is more stable, with some small and larger oscillations, which may be natural variations in the measurements or slight deviations from the main flow zone.

When disregarding the peaks and troughs, there is a steady decrease in the concentration from the upstream to the downstream end.

10.4.2   Simulated

The low concentration in the first two measurements is matched by both simulations. These are measurements outside the main flow zone, and the simulated stream lines follow the same path.

Both simulations capture the first peak at 3-4. The magnitude of the concentration peak is also matched well, especially by the simulation with the second-order upwind scheme.. The length of the peak is however not reproduced. The reason for this is probably that the real flow field was slightly different around profiles 5-8, so that the measurements were not made in the most concentrated area.

The measured concentrations drop further in profiles 11-12. This is seen slightly in the both simulations, but not in the same location. The reason for the drop in the measurements is the influence of the Turrialba river, whose water is quite clear compared to the overall water in the reservoir.

The second peak in profiles 13-14 is seen only as a small concentration increase in the simulation results. A previous simulation using a second-order upwind scheme gave results also reproducing this peak. However, a bug was found in the implementation of the scheme in the numerical model, so the results could not be used. Unfortunately, after the bug was fixed, the results were never as good. The main factor influencing the results is the flow field, and the area around the Turrialba inlet (profiles 11-15) and downstream the passage (profiles 16-19) are most vulnerable to changes. The complex geometry in these areas, with curved channels and secondary inflows through the two passages, creates multiple large, interacting turbulent eddies, which are responsible for the distribution of the sediment concentrations in the area. Small changes in the geometry, water level or discharges from the different rivers might change this flow field drastically. It is believed that the flow field simulated with the second-order scheme containing the bug was closer to the actual flow field during the measurements, but for the wrong reasons.

Prior to the bug fix, the first and second-order schemes gave more contrasting results. The simulated velocity fields contained large differences in the downstream range of the reservoir, more than would be expected with the current grid quality. After the bug was fixed, the results from the two different discretization schemes are much more alike, with most differences stemming from false diffusion. The bug stemmed from an error in the discretization close to walls, where only first-order discretization may be used for the flux from the border cells, but second-order discretization is used for the flux at the next surface. The result of this bug is that the program miscalculated the concentration gradients close to walls, and this may affect the vortexes in the whole flow field.

The bug fix shows the importance of testing of simulation software, and hence one of the objectives of this thesis, as some programming errors may be very well concealed and only be detected after years of research. The current version of the discretization scheme is also verified to be correct by comparison to a different implementation according to (Waterson and Deconinck, 2007).

10.5 Vertical Concentration Distribution

10.5.1 Measured

Most of the measurements have vertical profiles similar to the theoretical according to the Rouse formula, equation 2.7, especially in the downstream range of the reservoir. However, there are some discrepancies. The reference level for the Rouse profiles in figure 9.6 is chosen as the level of the lowest measurement point. The ratio between this and the actual water depth will vary from profile to profile, and may not be strictly comparable. This will cause random variations in the results. The highest concentration in each vertical is chosen as the reference concentration. This is done to set an upper bound of 1.0 on the x-axis, but it may also distort the figure, especially in profiles with only a few measurements with high concentrations.

Profile 8 originally showed a deviating curve for size 26.9 µm. This was caused by a high-concentration measurement close to the surface for the corresponding two LISST size fractions, which caused the lower part of this size's curve to be shifted to the left. The measurement was probably caused by floating organic matter entering the LISST tube. Apart from this erroneous measurement, the profile was without anomalies.

Some of the profiles, notably No. 4, 6, 13 and 14, show high concentrations close to the bed. The most likely reason is that the measurements also captured some of the bedload, as observed in the duplicate measurements in figure 9.2. This is further supported by observing the particle size distribution at different depths. It can be seen that the measurements close to the bed have a more prominent concentration of coarse sediment, which is characteristic for bedload. This is displayed in figure 10.4, where the grain size distributions for profile 14 are shown at depths 1.4 and 11 m.

Figure 10.4: Concentration profiles in profile 14
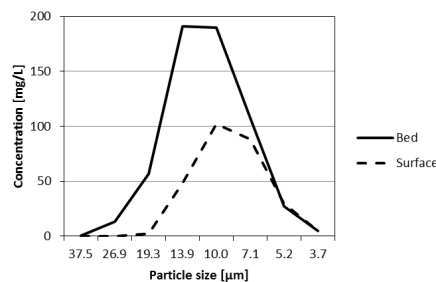
Profiles 3 and 5 show concentration peaks midway between the bed and the surface. This can be caused by local upwelling or turbulent eddies. The same tendency can also be seen in profiles 7, 16 and 20, but not as strong.

Profile 2 is the most inscrutable. From the middle of the profile and upwards, the concentration increases, and the effect is most prominent in the coarser

92

fractions. From a sediment point of view, this is hard to explain. The most likely cause of increasing concentration close to the surface is particles with a density lower than that of water, for example algae. Floating organic matter was observed in the field, but not necessarily in this location.

10.5.2 Simulated

The bed load seen in some of the measurements is not modeled as suspended load in the model, and is hence not reproduced in the figures. Some measured profiles have concentration variations, that are not modeled. The measurements represent instantaneous captures of the turbulent flow, while the numerical model solves the time-averaged Navier-Stokes equations, where the time-dependent variations have been removed. It is likely that an averaging of multiple measurements in the same locations would yield profiles more similar to the theoretical.

In almost all cases, the Rouse profiles from both simulations have the shape predicted by equation 2.7, with some exceptions. When disregarding the irregularity in the measurements, the simulated profiles agree quite well with the measured ones. The ratio of surface to bed concentration matches well for most of the profiles, especially in the simulation with the first-order scheme.

Profile 2 in the simulation with the first-order scheme shows a concentration drop close to the bed. The point is located in a shear layer of a recirculation zone with strong secondary currents. The concentrations inside the recirculation zone are lower than at the outside, and the velocity vectors in the bed cell are different from the vector at higher elevations. In the simulation with the second-order scheme, the point is located almost in the center of the recirculation zone, and therefore we do not see the same trend in the profile. However, this profile has the lowest ratio of surface to bed concentrations in the simulations. This can be because the the profile location inside the recirculation zone, where the velocity and turbulent diffusion is low. The capacity to keep sediment is suspension is thereby reduced.

Profile 17 in both simulations deviates strongly from the theoretical profile. The highest concentration is midway between the surface and the bed. This is likely caused by an upwelling close to the bed, where a water flux transports sediment from the bed and upwards in the water column. In figure 10.5, the simulated vertical velocities in the profile are plotted versus the depth. Close to the bed, the velocity is positive (upwards), while it is negative closer to the surface. In this location, water is flowing through the passage between the island and the peninsula, generating turbulent eddies with a complex velocity field. Although the magnitude of the vertical velocities is below 1 mm/s, this is the same range as the settling velocities of the particles, so it is still sufficient to keep the sediment in suspension. It is hard to see the same tendency in the measurements, but it is probably a very local phenomenon. Even if the same process was happening in the measured location, the uncertainties in the measurements are in the same range as the magnitude of the theoretical variation, so it may appear as random noise.
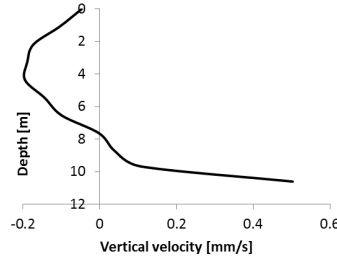
Figure 10.5: Vertical velocity in profile 17

In general, the simulation with the first-order scheme gives profiles with a lower ratio between surface and bed concentrations than the simulation with the second-order scheme. Using a second-order upwind scheme, the simulated diffusion will typically be higher than with first-order schemes, and the high diffusion keeps more sediment in suspension, making the vertical profiles more uniform. The difference is largest in profile 11, 21 and 25. In profiles 9 and 10, which are duplicate measurements and hence identical in the simulations, the first-order scheme gives the smallest ratio of surface to bed concentrations. However, this is caused by a local flow field that differs in the two simulations, so that the diffusion is higher in the simulation with the first-order scheme.

10.6   Flushing

Sediment flushing is a very difficult process to model. The amount and distribution of erosion and sedimentation depend critically on input data, algorithms used and assumptions made. The limited time assigned for this part of the thesis was not enough to optimize the results.

10.6.1   Measured

Along the border of the reservoir, the measured bed changes show small alternating areas of large erosion and sedimentation. These are not real bed changes, but stem from differences in where the measurements were made before and after the flushing, which after bed interpolation and subtraction is treated as bed changes. The zones closest to the borders should therefore not be included in the analysis.

The measured bed changes show that there is little change in the flat upstream plains in the reservoir. The further away from the main channel, the less erosion. Along the main channel, a layer of up to two meters is eroded, and this channel continues all the way down to the first island. In the area around the Atirro inflow, there is also a bed change of two meters. Where the reservoir curves around the islands, there is a bed change of about 0.5 m.

Because the September flushing only has a partial drawdown, the downstream end of the reservoir does not have river flow at any time during the

flushing. This leads to extensive deposition in the whole area, the largest bed changing being in the main channel, where the reservoir was originally deepest. A bed change of maximum three meters was measured.

Although the inflow concentration time series was cut off too early, it is stipulated that the inflowing sediment volume during the flushing is about 390,000 m^3. With a net erosion of 220,000 m^3, this means that about 65% of the sediment outflow from Angostura during the flushing is from the sediment inflow. However, it is not known if the sediments that are eroded in the upstream end of the reservoir are deposited in the downstream end or flushed out.

10.6.2 Simulated

In the upstream end of the reservoir, the same trends can be seen in the simulation as in the measurements. There is a flushing channel from the Reventazón river with up to two meters of bed change. However, the channel does not reach as far in the simulation as in the measurements. There are two areas of sedimentation on the sides of the channel. This can also be seen in the measurements, but not to the same degree, and not in the same locations. There is no erosion around the Atirro inflow in the simulation. This is caused by a grid split at low water levels, excluding the water inflow from this river when the erosive power is at its largest.The bed changes in the reservoir curve seem to agree well with the measurements, with values around 0.5 m.

The downstream area is however not well modeled. While the measured bed changes had depths of up to three meters, the larges deposition in the simulation is around one meter. Most of the area has no deposition at all.

The volume change in the final simulation was around 141,000 m^3. This value can easily be adjusted to give the same amount as the value from the bathymetry by varying some of the parameters described in the next section. However, this does not make any sense as long as the distribution of sedimentation and erosion in the reservoir is not yet modeled correctly.

10.6.3 Parameter Sensitivity

Many parameters and algorithms were tested to improve the results. A total of 29 stable simulations were run, and show a great variability both in total volume change, and in the distribution of erosion and sedimentation. Some of the findings are presented here.

Grain-size Distribution in Inflow

As the grain-size distribution in the inflow is unknown, it is a great source of uncertainty. Coarse sediment will settle in the upper end, while finer sediment will either settle in the downstream end or follow the water out of the flushing gates. Two different distributions with mean size of 72 μm and 20 μm were tested, showing the large influence on the total volume. The simulation with the coarse material gave almost no erosion in the upstream end, and extensive sedimentation on both sides of the flushing channel.

Table 10.3: Volume change influence from grain-size distribution

Mean size μm	Volume change 1000 m^3
72	-496
20	-165

Roughness

Three simulations were performed with different roughness, while all other parameters stayed the same. Values of 0.01, 0.1 and 0.2 m were used. These simulations were performed while the overall results were still very poor, with sedimentation in almost the whole reservoir. Table 10.4 shows the volume changes in the different simulations. A higher roughness gives less overall sedimentation, but more sedimentation in the downstream end of the reservoir. The difference in the volume change from 0.1 to 0.2 m is 25%.

Table 10.4: Volume change influence from roughness

Roughness m	Volume change 1000 m^3
0.01	-515
0.1	-597
0.2	-446

Rouse Extrapolation

Another algorithm that had a large influence was the Rouse extrapolation, explained in section 8.3.6. Similarly to the increase in roughness, including this algorithm gives more erosion in the downstream end, and more sedimentation in the downstream end. The difference in volume change is large, but dependent on the sediment size. For a mixture of coarse and fine material in the inflow, the sedimentation in the upstream end was dominating, giving a positive reservoir volume change from including the algorithm. However, with mostly fine material in the inflow, the increased sedimentation in the downstream end leads to a negative reservoir volume change from including the algorithm, as seen in table 10.5

Table 10.5: Volume change influence from Rouse extrapolation

Rouse extrapolation	Sediment	Volume change 1000 m^3
No	Mixed	-466
Yes	Mixed	-320
No	Fine	204
Yes	Fine	83

Sediment Transport Formula

The default bed sediment concentration formula in SSIIM is the van Rijn formula, equation 4.56. The default coefficients of 0.015, 1.5 and 0.3 may be changed by invoking the F 6 data set in SSIIM. The first coefficient was changed to see the influence. However, this was only tested before the concentration measurements were available. In addition, the Wu formula was tested in a separate simulation, with the measured inflow concentrations.

Table 10.6: Volume change influence by van Rijn coefficients

	van Rijn coefficient	Volume change 1000 m^3
	0.015	67
	0.035	88
van Rijn	0.015	-465
Wu		-439

11   Conclusion

Although the RESCON model has given promising results in other cases, it is not able to model the flushing of Angostura. The complex reservoir geometry sets heavy restrictions on the flushing processes in the reservoir, which an algebraic model of this type cannot reproduce.

No high-quality verification data for the reservoir velocities exists, so the validity of the simulated velocity field can only be estimated from observations in the field and the concentration distribution measurements.

Previously unexplained variations in the lateral concentration variation have been explained by distance from a main high-concentration flow zone. This is simulated quite well in the numerical model, but some variations are not captured due to deviations in the velocity field. Measured vertical concentration variations are in general simulated well in the model, giving similar Rouse profiles in measurements and model. However, some measured profiles contain large random variations and inclusion of bedload, which are not reproduced by the model.

Early differences between first and second-order scheme results led to the discovery of a bug in the second-order upwind scheme in the numerical program. In the context that the main purpose of this thesis is verification and improvement of the program, this discovery was very welcome. The corrected discretization scheme implemented by professor Olsen gives more similar results to the first-order scheme, and has been verified by other methods.

The time allocated for the flushing simulation was not enough to get satisfactory results. The erosion in the upstream end is modeled well, but the measured sedimentation in the downstream area is much larger than in the simulations. With more time for this simulation, it would have been possible to increase the quality of the results.

12 Further Work

The results from the RESCON model shows that it is not valid for reservoirs with complex geometry. It could still be tested more extensively for simpler reservoirs. The lack of sediment routing support in the model may be a limitation for other reservoirs in series, where flushing of upstream reservoirs gives high sediment inflow to the downstream reservoir during the flushing. This could be tested with reservoir arrangements where this is the case, and if possible, the model could be expanded to also handling this sediment management strategy.

The low quality of the velocity measurements from the reservoir in September 2011 was caused by trouble with the ADCP. Without proper velocity measurements, it is difficult to get a good verification of the simulated velocity field, which is essential also for the concentration distribution. Given more experience with the LISST instrument, it could also be advantageous with better lateral concentration measurements, although this is believed to be understood quite well.

The flushing simulation was only partially successful because of limited allocated time for this simulation. This leaves further work to be done to improve these results. There are more variables and algorithms to vary, and knowledge about the grain-size of the inflowing sediment would be of a great advantage.

References

Alvarado, P., Jiménez, O., Ramírez, C., Valverde, J., 1993. Proyecto hidroeléctrica Angostura. ICE.

Anderson, J., 1995. Computational Fluid Dynamics. The Basics with Applications. McGraw-Hill Science/Engineering/Math.

Apsley, D., Hu, W., 2003. Cfd simulation of two- and three-dimensional free-surface flow. International Journal for Numerical Methods in Fluids 42, 465–491.

Atkinson, E., November 1996. The feasibility of flushing sediment from reservoirs. Tech. rep., HR Wallingford.

bcr, 2012. Temperature map costa rica.
URL http://www.bestcountryreports.com/Temperature_Map_Costa%20Rica.php

Blazek, J., 2001. Computational Fluid Dynamics: Principles and Applications. Elsevier Science.

Brune, G. M., November 1953. Trap efficiency of reservoirs. Transactions, American Geophysical Union 34, 3.

Calderón, C. F., 2002. Manejo integrado de águas subterráneas: Estudio del aquífero de Angostura Turrialba, provincia de Cartago, Costa Rica. Editorial Universidad Estatal a Distancia, pp. 119–128.

Catano, N., Marchand, M., Staley, S., Wang, Y., 2009. Development and validation of the watershed sustainability index (wsi) for the watershed of the reventazón river. Tech. rep., Comcure.

CRMP, 2007. Costa rica map project - precipitation map.
URL http://www.costaricamapproject.com/maps/Weather/Precipitation-sm.jpg

Date, A. W., 2005. Introduction to Computational Fluid Dynamics. Cambridge University Press.

Ferziger, J. H., Peric, M., 2001. Computational Methods for Fluid Dynamics. Springer.

Fletcher, C. A. J., 1996. Computational Techniques for Fluid Dynamics, Vol. 1: Fundamental and General Techniques. Springer.

Harlow, F. H., Welch, J. E., 1965. Numerical calculation of time-dependent viscous incompressible flow of fluid with free surface. Physics of Fluids 8, 2182–2189.

Hoven, L. E., 2010. Three-dimensional numerical modelling of sediments in water reservoirs. Master's thesis, NTNU.

ICE, 2011. Generación hidroeléctrica sostenible en américa latina en el contexte del cambio climático.
URL http://www.grupoice.com/wps/wcm/connect/7f941880488e7a158f059f051eb7cca6/brochure_

ICE, 2012a. Descubra el tesoro de costa rica.
URL http://www.grupoice.com/wps/wcm/connect/41a9e10047cdeeab937ffbf079241ace/tesoro_cr

ICE, March 2012b. Plan de expansión de la generación electrica periodo 2012-2024.
URL http://www.grupoice.com/wps/wcm/connect/3bd3a78047cdebee904df9f079241ace/PEG2011re

Jimenez, O., Rodríguez, C., Olsen, N. R. B., 2004. Sedimentation in the angostura reservoir: Studies and experiences. 9th International Symposium on River Sedimentation, Yichang, China.

Løvfall, S., 2011. Three-dimensional numerical modelling of sediment deposition in the angostura hydropower res. Tech. rep., NTNU.

Mahmood, K., 1987. Reservoir sedimentation: Impact, extent and mitigation. Tech. rep., World Bank.

MARNET, 2000. Best practice guidelines for marine applications of computation fluid dynamics. Tech. rep., MARNET CFD.

Muzaferija, S., Peric, M., 1997. Computation of free-surface flows using the finite-volume method and moving grids. In: Numerical Heat Transfer - Part B - Fundamentals: An International Journal of Computation and Methodology.

Olsen, N. R. B., 2011a. Numerical Modelling and Hydraulics. NTNU.

Olsen, N. R. B., November 2011b. A Three-Dimensional Numerical Model for Simulation of Sediment Movements in Water Intakes with Multiblock Option. NTNU.

Palmiere, A., Shah, F., Annandale, G. W., Dinar, A., June 2003. Reservoir Conservation Volume 1: The RESCON Approach. World Bank.

Ramirez, O. J., Meza, C. R. R., Olsen, N. R. B., 2003. Sedimentación del embalse del p.h. angostura, estudios y experiencias.

Rodi, W., 1984. Turbulence Models and Their Application in Hydraulics. Insitut für Hydromechanik, University of Karlsruhe.

Sequoia, 7 2008. Random shaped particles & lissts.
URL http://www.sequoiasci.com/Articles/ArticlePage.aspx?pageId=133

Sequoia, February 2011a. The influence of particles outside the size range of the lisst.
URL http://sequoiasci.com/Articles/ArticlePage.aspx?pageId=221

Sequoia, 4 2011b. Laser diffraction 101.
URL http://www.sequoiasci.com/Articles/ArticlePage.aspx?pageId=229

Sequoia, 4 2011c. Laser diffraction 201.
URL http://www.sequoiasci.com/Articles/ArticlePage.aspx?pageId=230

Sequoia, 2011d. Lisst-sl.
URL http://www.sequoiasci.com/graphics/upload/LSL/SL-TB-Breel-800pxW.jpg

Sequoia, 2011e. LISST-SL Version 2.1.

Tecun, 2010. Río macho y cachí - costa rica.
URL http://tecun.com/emdt/100216/Riomacho.pdf

UDGN, 2008. Plan de cuenca del río reventazón-parismina. Tech. rep., Unidad de gestión nacional - Costa Rica.

USBR, 2006. Erosion and Sedimentation Manual. Books Express Publishing.

Van Rijn, L., 1984. Sediment transport, part iii: Bed forms and alluvial roughness. Journal of Hydraulic Engineering, ASCE 110, 1733–1755.

Vanoni, V. A., 2008. Sedimentation Engineering: Processes, Management, Modeling, and Practice. American Society of Civil Engineers.

Vega, E. R. (Ed.), 2004. Costa Rica en el siglo XX. EUNED.

Versteeg, H., Malalasekera, W., 2007. An Introduction to Computational Fluid Dynamics: The Finite Volume Method. Prentice Hall.

Waterson, N. P., Deconinck, H., 2007. Design principles for bounded higher-order convection schemes - a unified approach. Journal of Computational Physic 224, 182–207.

Wesseling, P., 2000. Principles of Computational Fluid Dynamics. Springer.

White, R., 2001. Evacuation of Sediments from Reservoirs. Thomas Telford Press.

Wilcox, D. C., 1995. Turbulence Modeling for CFD. DCW Industries.

A Input Files

```
T steady state pow

F 1 D                                         detailed boogie file
F 2 US                                        opening sequence
F 16 0.01                                     roughness
F 33 50 10                                    timestep, inner iterations
F 36 2                                        free water surface algorithm
F 37 2                                        sediment computation
F 48 16                                       output files
F 64 13                                       grid generation algorithm
F 65 180000 3300000 180000 50000 6000         number of cells, points and surfaces
F 94 0.01 0.1                                 cells below 0.01 m not generated, cells below 0.1 m as 2d
F 102 1                                       wetting and drying algorithm
F 105 2                                       surface update interval
F 106 0.3                                      active sediment layer thickness
F 112 1                                       lower water surface, read unstruc, then read koordina
F 113 7                                       stabilize triangular cells
F 159 1 2 0 1 0                               avoid grid problems
F 168 9                                       multigrid solver
F 200 1 0.1 0.01                              scaling values k and epsilon
F 206 4                                       max number of threads
F 235 10                                      stabilize cells
F 291 1 3 0.01                                stabilize edge cells
F 292 1 2.0                                   timestep inner iteration ns equation
F 293 1                                       write residual file
G 1 300 300 15 8                              grid size xyz, number of sediment sizes
G 6 72013 0 0 0.5 0.5                         downstream reference cell
P 10 100                                      output file write interval
W 1 50 150 576                                manning, discharge, water level
K 1 10000 100                                 max number of interations
K 3 0.4 0.4 0.4 0.2 0.2 0.2                    relaxation factor velocity, continuity, k, e
K 5 0 0 0 1000 0 0                            multigrid algorithm


S 1 0.00003747 0.0012628
S 2 0.00002691 0.0006510
S 3 0.00001932 0.0003356                      sediment size and fall velocity
S 4 0.00001387 0.0001730
S 5 0.00000996 0.0000892
S 6 0.00000715 0.0000460
S 7 0.00000513 0.0000237
S 8 0.00000369 0.0000122

N 0 1 0
N 0 2 0.15
N 0 3 0.15
N 0 4 0.175                                   bed sediment distribution
N 0 5 0.175
N 0 6 0.15
N 0 7 0.1
N 0 8 0.1
```

Figure A.1: Control file steady state simulation

```
I       0      -1 -1 -1 576.2 1.94E-07 4.26E-06 5.26E-05 9.81E-05 7.55E-05
3.40E-05 3.02E-06 6.04E-06 3.89E-07 8.52E-06 1.05E-04 1.96E-04 1.51E-04 1.89E-05
6.04E-06 1.21E-05 1.94E-07 4.26E-06 5.26E-05 9.81E-05 7.55E-05 3.40E-05 3.02E-06
6.04E-06 0.00E+00 0.00E+00 0.00E+00 0.00E+00 0.00E+00 0.00E+00 0.00E+00 0.00E+00
0.00E+00 0.00E+00 0.00E+00 0.00E+00 0.00E+00 0.00E+00 0.00E+00 0.00E+00
I     250000  -1 -1 -1 576.0 1.94E-07 4.26E-06 5.26E-05 9.81E-05 7.55E-05
3.40E-05 3.02E-06 6.04E-06 3.89E-07 8.52E-06 1.05E-04 1.96E-04 1.51E-04 1.89E-05
6.04E-06 1.21E-05 1.94E-07 4.26E-06 5.26E-05 9.81E-05 7.55E-05 3.40E-05 3.02E-06
6.04E-06 0.00E+00 0.00E+00 0.00E+00 0.00E+00 0.00E+00 0.00E+00 0.00E+00 0.00E+00
0.00E+00 0.00E+00 0.00E+00 0.00E+00 0.00E+00 0.00E+00 0.00E+00 0.00E+00
I     500000  -1 -1 -1 576.0 1.94E-07 4.26E-06 5.26E-05 9.81E-05 7.55E-05
3.40E-05 3.02E-06 6.04E-06 3.89E-07 8.52E-06 1.05E-04 1.96E-04 1.51E-04 1.89E-05
6.04E-06 1.21E-05 1.94E-07 4.26E-06 5.26E-05 9.81E-05 7.55E-05 3.40E-05 3.02E-06
6.04E-06 0.00E+00 0.00E+00 0.00E+00 0.00E+00 0.00E+00 0.00E+00 0.00E+00 0.00E+00
0.00E+00 0.00E+00 0.00E+00 0.00E+00 0.00E+00 0.00E+00 0.00E+00 0.00E+00

D       0      78.5 9.0 0.0 2.7 90.2 0 0 0 0 576.2
D     250000  78.5 9.0 0.0 2.7 90.2 0 0 0 0 576.0
D     500000  78.5 9.0 0.0 2.7 90.2 0 0 0 0 576.0
```

Figure A.2: Timei file steady state simulation

```
T flushing
F 1 D                                    detailed boogie file
F 2 U                                    opening sequence
F 16 0.1                                 roughness
F 33 50 50                               time step, inner iterations
F 36 7                                   free water surface algorithm
F 37 2                                   sediment computation
F 60 1 0                                 rouse extrapolation
F 64 13                                  grid generation algorithm
F 65 180000 3300000 180000 50000 6000    number of cells, points and surfaces
F 94 0.25 1.0                            cells below 0.01 m not generated, cells below 0.1 m as 2d
F 102 1                                  wetting and drying algorithm
F 105 1                                  surface update interval
F 106 0.5                                active sediment layer thickness
F 112 1                                  lower water surface, read unstruc, read koordina
F 113 7                                  stabilize triangular cells
F 139 8.5 0.1                            minimum value of u+
F 147 80 0 1 0.2 1.0 1.0                 extrapolation to wetted cells
F 154 0.5                                smoothing water surface
F 159 1 11 0 1 5                         avoid grid problems
F 164 31                                 openmp solver version
F 168 9                                  multigrid solver
F 178 4                                  smoothing water suface
F 179 1 1                                upwind function
F 187 -1                                 reduce water level gradients
F 200 1 0.1 0.01                         scaling values k and epsilon
F 206 8                                  max number of threads
F 219 4                                  flushing restart
f 224 1000                               surface residual
F 233 7                                  surface from depth-averaged pressure
F 235 10                                 stabilizing cells
F 287 2                                  outflow from water level
F 291 1 3 0.01                           stabilization of edge cells
F 292 1 2.0                              time step inner iteration ns equation
F 293 1                                  write residual file
G 1 300 300 15 4                         grid size xyz, number of sediment sizes
G 6 72013 0 3 0.10 0.01                  downstream cell reference
W 1 50 150 576                           manning, discharge, water level
K 1 8640 20000                           number of iterations
K 3 0.2 0.2 0.2 0.1 0.1 0.1              relaxation factor for velocities, continuity, k, e
K 5 0 0 0 10 0 0                         multigrid algorithm
K 6 1 1 1 0 0 0                          discretization scheme

S 1 0.000300 6.00E-02
S 2 0.000100 8.00E-03                    sediment size and fall velocity
S 3 0.000030 1.50E-03
S 4 0.000002 3.60E-06
N O 1 0.25
N O 2 0.25                               bed sediment distribution
N O 3 0.25
N O 4 0.25
B 0 0 0 0 0 0 0 0
```

Figure A.3: Control file flushing simulation

```
I      0       -1 -1 577 576 0.00E+00 0.00E+00 3.02E-04 4.53E-04 0.00E+00 2.26E-05 6.79E-05 1.36E-04
I      72000   -1 -1 577 574 0.00E+00 0.00E+00 3.02E-04 4.53E-04 0.00E+00 2.26E-05 6.79E-05 1.36E-04
I      90000   -1 -1 577 565 0.00E+00 0.00E+00 6.04E-04 9.06E-04 0.00E+00 2.26E-05 6.79E-05 1.36E-04
I      93600   -1 -1 577 565 0.00E+00 0.00E+00 1.51E-03 2.26E-03 0.00E+00 2.26E-05 6.79E-05 1.36E-04
I      100800  -1 -1 577 565 0.00E+00 0.00E+00 1.21E-02 1.81E-02 0.00E+00 2.26E-05 6.79E-05 1.36E-04
I      108000  -1 -1 577 565 0.00E+00 0.00E+00 1.21E-02 1.81E-02 0.00E+00 2.26E-05 6.79E-05 1.36E-04
I      115200  -1 -1 577 565 0.00E+00 0.00E+00 1.21E-02 1.81E-02 0.00E+00 2.26E-05 6.79E-05 1.36E-04
I      126000  -1 -1 577 565 0.00E+00 0.00E+00 7.55E-03 1.13E-02 0.00E+00 2.26E-05 6.79E-05 1.36E-04
I      216000  -1 -1 577 565 0.00E+00 0.00E+00 1.51E-03 2.26E-03 0.00E+00 2.26E-05 6.79E-05 1.36E-04
I      234000  -1 -1 577 565 0.00E+00 0.00E+00 6.04E-03 9.06E-03 0.00E+00 2.26E-05 6.79E-05 1.36E-04
I      244800  -1 -1 577 565 0.00E+00 0.00E+00 1.21E-02 1.81E-02 0.00E+00 2.26E-05 6.79E-05 1.36E-04
I      252000  -1 -1 577 565 0.00E+00 0.00E+00 1.21E-02 1.81E-02 0.00E+00 2.26E-05 6.79E-05 1.36E-04
I      266400  -1 -1 577 565 0.00E+00 0.00E+00 4.53E-03 6.79E-03 0.00E+00 2.26E-05 6.79E-05 1.36E-04
I      270000  -1 -1 577 565 0.00E+00 0.00E+00 2.26E-03 3.40E-03 0.00E+00 2.26E-05 6.79E-05 1.36E-04
I      342000  -1 -1 577 573 0.00E+00 0.00E+00 1.51E-03 2.26E-03 0.00E+00 2.26E-05 6.79E-05 1.36E-04
I      432000  -1 -1 577 576 0.00E+00 0.00E+00 1.51E-03 2.26E-03 0.00E+00 2.26E-05 6.79E-05 1.36E-04
I      468000  -1 -1 577 577 0.00E+00 0.00E+00 1.51E-03 2.26E-03 0.00E+00 2.26E-05 6.79E-05 1.36E-04

D      0        80 9 89 0 0 0 0 0 0 576
D      72000    80 9 89 0 0 0 0 0 0 574
D      90000    120 9 129 0 0 0 0 0 0 565
D      93600    180 9 189 0 0 0 0 0 0 565
D      100800   200 9 209 0 0 0 0 0 0 565
D      108000   170 9 179 0 0 0 0 0 0 565
D      115200   100 9 109 0 0 0 0 0 0 565
D      126000   80 9 89 0 0 0 0 0 0 565
D      216000   80 9 89 0 0 0 0 0 0 565
D      234000   90 9 99 0 0 0 0 0 0 565
D      244800   220 9 229 0 0 0 0 0 0 565
D      252000   250 9 259 0 0 0 0 0 0 565
D      266400   220 9 229 0 0 0 0 0 0 565
D      270000   80 9 89 0 0 0 0 0 0 565
D      342000   60 9 69 0 0 0 0 0 0 573
D      432000   60 9 69 0 0 0 0 0 0 576
D      468000   60 9 69 0 0 0 0 0 0 577
```

Figure A.4: Timei file flushing simulation

B Assignment Text

Sedimenter i Angostura vannkraftreservoar

Bakgrunn

Sedimenter som fyller opp vannreservoarer er et stort problem på verdensbasis. Det fører til at tilgjengelig reguleringsvolum for et vannkraftverk vil minske over tid, med tilhørende økonomiske konsekvenser. Viktige spørsmål er da hvor fort prosessen skjer, og hvor effektiv mulige mottiltak vil være, for eksempel spyling av reservoarene. Sedimentdeponering og spyling kan modelleres med en tredimensjonal numerisk modell, hvis denne gir pålitelige resultater.

For å undersøke dette nærmere har det vært foretatt en innsamling av feltdata for Angostura-kraftverket i Costa Rica. Disse dataene kan brukes til å teste hvor godt den numeriske modellen kan beregne sedimenttransport under deponering og spyling. Feltmålingene er gjort i samarbeid med det lokale kraftselskapet ICE (Instituto Costarricense de Electricidad) og med støtte fra et prosjekt finansiert fra Norges Forskningsråd.

En av problemstillingene i prosjektet er hvor godt den numeriske modellen kan beregne sedimentkonsentrasjonene i reservoaret. Dette kan sammenlignes med målingene tatt med LISST-SL instrumentet. Det er ønskelig å se på profiler i lengderetningen, tverrstrøms retning og i vertikal retning, og forsøke å forklare variasjonene i profilene med fysiske prosesser i reservoaret, for eksempel sekundærstrømninger, resirkulasjonssoner og sedimentenes fallhastighet i forhold til turbulensnivået. Det er interessant å se hvorvidt den numeriske modellen kan replisere disse prosessene.

En annen viktig prosess er utspylingen av sedimentene. Her kan en sammenligne resultatene fra den numeriske modellen med topografiske bunndata før og etter utspylingen. Et viktig spørsmål er hvor nøyaktig den tredimensjonale numeriske modellen kan beregne utspylingen, inkludert utspylt volum og hvor de eroderte sedimentene kommer fra i reservoaret. Det er interessant å sammenligne usikkerheten og nøyaktigheten i beregningene med enklere ingeniørmessige overslagsformler for erosjonsmengden. Disse kan for eksempel tas fra RESCON-modellen med tilhørende litteratur.

Datasett som kan brukes til disse beregningene er fra september 2011 og november 2011. For å spare tid kan kandidaten samarbeide med PhD-student Stefan Haun og bruke hans og tidligere masterstudent Sigurd Løvfalls inngangsdata til SSIIM-modellen fra september 2011.

Viktigste spørsmål i oppgaven

Oppgaven kan besvare følgende spørsmål:

1. Sedimentdeponering

   - Hvordan ser sedimentkonsentrasjonsprofilene ut i Angostura-reservoaret?

Dette gjelder profiler i alle tre retninger, for forskjellige sedimentfraksjoner.

- Hvordan beskriver man de fysiske prosessene som skaper variasjon i profilene?

- Hvordan repliserer den numeriske modellen disse prosessene, og med hvilken kvalitet?

2. Reservoarspyling

- Hvor korrekt modellerer den numeriske modellen utspylt sedimentvolum?

- Hvor korrekt modellerer den numeriske modellen det geometriske området som blir erodert/deponert under utspylingen?

- Hvor god er nøyaktigheten på den tredimensjonale numeriske modellen i forhold til enklere metoder?

- Hva er fordeler/ulemper med den tredimensjonale numeriske modellen i forhold til enklere metoder?

Veiledning og rapportering

Prof. Nils Reidar Olsen vil være hovedveileder for oppgaven. I tillegg kan kandidaten få støtte av PhD-student Stefan Haun, som arbeider med samme problemstilling. Kandidaten kan også søke hjelp hos Dr. Nils Rüther som også arbeider med numerisk modellering ved vårt institutt. Kandidaten kan få informasjon fra Carlos Roberto Rodriguez ved ICE i Costa Rica.

En profesjonell strukturering av oppgaven er viktig. Oppgaven skal bl.a. inneholde innholdsliste, figurliste og referanseliste. Det er ønskelig at oppgaven inneholder sort/hvitt strekfigurer av bl.a. grid, hastighetsvektorer og sammenligninger mellom målinger og beregninger, i tillegg til fargefigurer av vesentlige parametere.

I tillegg til papirkopier av oppgaven, skal det leveres en CD med en PDF-fil og en Word/Framemaker/tekstbehandlingsfil av oppgaven, samt separate filer av oppgavens figurer og de viktigste input-filene for de numeriske beregningene.

Anta at målgruppen for oppgaven er vassdragsingeniører med noe kjennskap til numerisk modellering, men uten detaljert kjennskap til SSIIM eller Costa Rica.

Denne teksten skal inkluderes i oppgaven, og vil bli brukt under sensureringen.